8-2021

Design, Analysis and Experimental Evaluation of 3D Printed Variable Stiffness Structures

Rossana R. Fernandes

DESIGN, ANALYSIS AND EXPERIMENTAL EVALUATION OF 3D PRINTED VARIABLE STIFFNESS STRUCTURES

By

Rossana R. Fernandes

A Dissertation Submitted to the Faculty of Embry-Riddle Aeronautical University

In Partial Fulfillment of the Requirements for the Degree of

Doctor of Philosophy in Aerospace Engineering

August 2021

Embry-Riddle Aeronautical University

Daytona Beach, Florida

DESIGN, ANALYSIS AND EXPERIMENTAL EVALUATION OF 3D PRINTED VARIABLE STIFFNESS STRUCTURES

By

Rossana R. Fernandes

This Dissertation was prepared under the direction of the candidate's Dissertation Committee Chair, Dr. Ali Tamijani, Department of Aerospace Engineering, and has been approved by the members of the Dissertation Committee. It was submitted to the Office of the Senior Vice President for Academic Affairs and Provost, and was accepted in the partial fulfillment of the requirements for the Degree of Philosophy in Aerospace Engineering.

DISSERTATION COMMITTEE

Ali Tamijani Digitally signed by Ali Tamijani Date: 2021.08.03 17:40:53 +04'30'

Chairman, Dr. Ali Tamijani

Marwan Al-Haik Digitally signed by Marwan Al-Haik DN: cn=Marwan Al-Haik, o=Embry-Riddle Aeronautical University, ou=Aerospace Engineering, email=alhaikm@erau.edu, c=US Date: 2021.08.03 20:14:34 -04'00'

Member, Dr. Marwan Al-Haik

Sirish Namilae Digitally signed by Sirish Namilae Date: 2021.08.04 16:22:49 -04'00'

Member, Dr. Sirish Namilae

Frank J. Radosta Digitally signed by Frank J. Radosta Date: 2021.08.03 11:39:44 -04'00'

Member, Dr. Frank Radosta

Rafael Rodriguez Digitally signed by Rafael Rodriguez Date: 2021.08.03 12:28:33 -04'00'

Member, Dr. Rafael Rodriguez

Sirish Namilae Digitally signed by Sirish Namilae Date: 2021.08.04 16:22:27 -04'00'

Graduate Program Coordinator,
Dr. Sirish Namilae

Date

Maj Mirmirani Digitally signed by Maj Mirmirani Date: 2021.08.04 17:18:38 -04'00'

Dean of the College of Engineering,
Dr. Maj Mirmirani

Date

Lon Moeller Digitally signed by Lon Moeller Date: 2021.08.05 09:23:38 -04'00'

Senior Vice President for Academic
Affairs and Provost,
Lon Moeller, J.D.

Date

ACKNOWLEDGEMENTS

I am eternally grateful to God for the life opportunities and the people I met, and for always giving me the strength that allowed me to persevere and complete this degree. I am deeply grateful to my parents for their love and sacrifice to raise me and provide my education. Without their and my sister's support, the completion of this degree would not have been possible. I wish to thank my cousin, Jorge Gamboa, for his career mentorship.

I would like to express my gratitude to my advisor, Dr. Tamijani, for his patience, support and guidance, and for believing in me even through the hardships. I extend my gratitude to Dr. Al-Haik for his support and advice and to my committee members, Dr. Radosta, Dr. Namilae and Dr. Rodriguez, for their time and prompt technical advice when needed. I would also like to thank Dr. Gordon Leishman, Dr. Zheng Zhang and the wind tunnel staff for their patience, expertise and time.

I also wish to thank Dr. Boutros Azizi, Dr. Kaveh Gharibi, Patricia Velasco and Sandeep Chava. Special thanks to Dr. Audrey Gbaguidi and Suma Ayyagari for their friendship and support. I cannot thank enough Dr. Barbara Abendschein, Dr. Bereket Berhane, Dr. Ilteris Demirkiran, and Mr. Matthew Kindy for the career advices and support. Thank you to everyone that directly or indirectly had an impact in my life.

This research was supported by the Office of Naval Research (ONR) under award number N000142012683 with program manager Dr. Anisur Rahman; the National Science Foundation (NSF) under award number 1847133 with program manager Dr. Kathryn Jablokow; and U.S. Air Force Office of Scientific Research (AFOSR) under award number FA9550-17-1- 0171 with Jaimie Tiley as the Program Manager. I wish to thank ONR, NSF and AFOSR for their support.

ABSTRACT

The rapid progress of additive manufacturing (AM) introduces new opportunities but also new challenges for design and optimization to ensure manufacturability, testability and accurate representation/prediction of the models. The present dissertation builds a bridge between design, optimization, AM, testing and simulation of advanced optimized variable-stiffness structures. The first part offers an insight on the mechanical, viscoelastic and failure characteristics of AM continuous fiber composites. This understanding was used in the second part to investigate the feasibility of different topology and fiber-orientation optimization methods and the manufacturability of the resulting models. The study also assesses the effects of the manufacturing constraints on the stiffness. In the third part, a framework was used to optimize the topology and orientation of lattice structures subjected to stress constraints. This framework uses homogenized stiffness and strength to expedite the optimization, and Hill's criterion to express the stress constraint. Those properties are implemented in the macrostructure topology optimization to improve the lattice structure stiffness. The optimized design is projected and post-treated to ensure manufacturability. The framework tested for two case studies producing designs with enhanced yield strength. The last part of this research challenges the capabilities of AM to fabricate, for the first time, an optimized flexible wing model with internal structures. The wing was tested in a low-speed wind tunnel to validate a robust computational model which enables the future study of the aeroelastic performance of different optimized wing models. This dissertation demonstrates that the conjoint use of topology and orientation optimization and AM results in advanced lighter structures with enhanced stiffness and/or strength.

TABLE OF CONTENTS

LIST OF FIGURES

Figure Page

Figure Page

Figure Page

LIST OF TABLES

NOMENCLATURE

A	Cross-sectional area
A_{ij}	Aerodynamic influence coefficient
$\mathbf{C}$	Stiffness tensor of the cell material
$\overline{\boldsymbol{C}}$	homogenized stiffness tensor
C_D, C_L, C_M	Coefficient of drag, lift, pitching moment
E	Elastic modulus
$\boldsymbol{F}$	Force vector
f	Frequency or constraint functions
F_e	Failure index
G_{12}	Shear modulus
g_m	Stress constraint
ΔH	Activation energy of glass transition
h_1, h_2	Horizontal and vertical dimensions of the cell hole
$\tilde{h}_n$	Intermediate filtered variable
h_{min}	Minimum printable feature size
$\boldsymbol{K}$	Stiffness matrix
K_{eff}	Effective stiffness
L	Cell size or lift
M_{ijkl}	Local structure tensor that relates the effective strain and micro-strain
P	Maximum load
p	Tuning parameter

p_i	Pressure
q	Dynamic pressure
q_1, q_2	Parameters that penalize the intermediate density
R	Universal gas constant
$\boldsymbol{R}$	Transformation matrix
R_e	Reynold's number
r_f	Filter radius
$\overline{\boldsymbol{S}}$	Inverse of the homogenized stiffness
SE	Compliance
SR	Strength ratio
T_g	Glass transition
t_n	Member thickness
$\boldsymbol{U}$	Displacement vector
$\boldsymbol{v}$	Wind speed
V_0	Volume of the design domain
V_f	Fiber volume fraction
V_g	Volume fraction constraint
V_m	Matrix volume fraction
Y	Cell domain
β	Projection parameter for controlling the intensity of the projection
γ	Dilation factor
δ	Deflection

δ_{ij}	Kronecker delta
$\bar{\boldsymbol{\varepsilon}}$	Effective strain
$\varepsilon_{pq}^{(0)kl}$	Microscopic unit strains
Λ	Periodicity
Ω_{m}	Volume of the element
$\partial\Gamma$	Boundary of the design domain
ϕ	Material indicator variable
η	Inflection point
$\bar{\boldsymbol{\sigma}}$	Effective macro-stress
σ	Normal stress
θ	Fiber or cell orientation
ρ	Density
ρ_{th}	Density threshold
τ_{12}	Shear stress
ν_{12}, ν_{21}	Major and minor Poisson's ratio
v_i	Virtual displacement field
χ^{kl}	Displacement field
AM	Additive manufacturing
3D	Three dimensional
CFRP	Carbon fiber reinforced polymer
DIC	Digital image correlation
DMA	Dynamic mechanical analysis

DSC	Differential scanning calorimetry
EQS	Equally spaced
FDM	Fused deposition modeling
FEA	Finite element analysis
FEM	Finite element method
ILSS	Interlaminar shear strength
MBB	Messerschmitt-Bolkow-Blohm
NACA	National advisory committee for aeronautics
SEM	Scanning electron microscope
SIMP	Solid isotopic material with penalization
SENB	Single-edge notched beam
SLA	Stereolithography
SLS	Selective laser sintering
SOMP	Solid orthotropic material with penalization
TE	Trailing edge
UAV	Unmanned aerial vehicles

1. Introduction

The high demand for faster, lighter and lower cost systems have been the main motivation of aerospace industry. The advances in additive manufacturing (AM) seems to correspond to those needs. The purpose of this research is to explore the advantage of AM to build advanced structures with variable stiffness and enhanced structural performance. This dissertation is divided in four main sections. The first section provides an insight on the mechanical properties and failure mechanisms of AM composite structures. The following two sections explores the feasibility and freedom of AM in the fabrication of topology- and orientation- (morphology) optimized structures made of continuous fibers or lattice structures. This knowledge is applied in the last section on a real life application: the analysis of an AM flexible wing. This section discusses the motivations for the present dissertation.

1.1. AM Composite Materials

The high demand for strong and lightweight materials makes composites an appealing choice in aerospace, such as in the design of wing structures (Rajpal, Gillebaart & De Breuker, 2019), optimization of unmanned aerial vehicles (UAV) (Boutemedjet et al., 2019) and launch vehicles (Morovat et al., 2019) and in the prevention of flutter (Asadi & Farsadi, 2020; Fernandes & Tamijani, 2017).

Composite materials have recently transitioned into the domain of AM, offering unique advantages over conventional composite manufacturing methods (van de Werken et al., 2021). Specifically, the AM of composites does not require tooling, enables manufacturing of complex geometries and short production lead times, and allows unprecedented control over fibers' placement and orientation. Therefore, the AM of composites can open new possibilities that will potentially transform the composites

industry (van de Werken, Hurley, et al., 2019; van de Werken, Tekinalp, et al., 2019).

Engineers can utilize the design freedom of AM and the highly anisotropic properties of carbon fiber reinforced polymers (CFRPs) to fabricate parts with adaptive fiber paths optimized for specific loading conditions. Traditional composite design focuses on engineering the stacking sequence or orientation of each, usually unidirectional, lamina within a laminate to improve the part performance and reduce mass. AM, however, allows for intricate steering of individual carbon fiber tows or filaments, laying them down in the most efficient orientations. Thus, both part geometry (topology) and fiber towpath can be optimized in composite AM. To this end, including the AM constraints in the design framework is crucial.

1.2. Design Optimization of Lattice Structures

A lattice structure comprises a network of cells with nodes and struts that offer exceptional properties such as high stiffness, energy absorption, and acoustic insulation. Lattice structure topology and morphology optimization have received considerable attention in recent years due to the emergence of new AM techniques with the ability to fabricate microstructures. Among the various multiscale optimization methods used to design lattice structures, the homogenization-based approach has been investigated the most. This is because the effective properties of local microstructures can be obtained using homogenization theory. A surrogate model is then obtained for various microstructure densities, and this surrogate model is used within the optimization process, significantly reducing the computational complexity of microstructure analysis during the optimization procedure. The stiffness-based de-homogenization approaches has proven to reduce weight of periodic lattice structures but its stiffness is still limited if the stress constraints are not considered during the optimization process. In addition,

utilizing stress constraints may change the optimized lattice structure topology and morphology. The goal of the current study is to investigate the optimization of the topologies and morphologies of lattice structures that are subject to stress constraints.

1.3. AM Flexible Wing Model

Fluid-structure interaction can lead to disasters if not considered during the design of flexible structures in a flow. When a flexible object or vehicle, such as an aircraft, is surrounded by a flow, the aerodynamic loads acting on the body will cause a deformation or change in its shape. This deformation will cause a change in the aerodynamic loads, creating a cycle. Vehicles are designed such that this interaction is stable.

Divergence and flutter are perhaps two of the most studied aeroelastic phenomena. Divergence is the static aeroelastic phenomenon in which the aerodynamic loads increase the deformation causing failure. Flutter happens when the structure can no longer damp the energy due to the fluid-structure interaction and starts oscillating at increasing amplitude until it fails. Flutter and divergence prevention involves changing the geometry in the design stage, using sensors and actuators (Livne, 2018), using stiffeners and using composite materials (Fernandes & Tamijani, 2017).

Effective prevention of these phenomena requires reliable ways to predict them. The aeroelastic response of a model can be studied through computational fluid-structure coupled models or through wind tunnel and flight tests (Livne, 2018). Computational models are often used in lieu of experimental data since they are usually faster and economical. However, for more advanced vehicles those models may not be accurate enough. Wind tunnel tests and reliable models are needed for validation since they have lower costs and are safer than flight tests (Zhu, 2019).

The objective of the last part of the research is: 1) to create a robust computational

framework to support an optimization framework in assessing the aeroelastic performance (including flutter and divergence characteristics) and efficiency of the optimized wing models. 2) To develop a guideline for the wind tunnel test used in the validation of the computational model. 3) To demonstrate the practicality of additive manufacturing in the fabrication of wind tunnel models for advanced concepts.

2. Review of the Relevant Literature

This section provides an overview of relevant existing work on AM composite materials, optimized AM composite structures, homogenization-based optimization of lattice structures and AM wind-tunnel models. The author reviews some advantages and disadvantages of AM composite materials and different studies on the optimization of continuous fiber composite structures and cellular structures. The advantages and challenges of AM wind tunnel models are also discussed.

2.1. AM Composite Materials

Carbon fiber reinforced polymeric composites are well known for their high strength-to-weight ratio, elevated stiffness, and corrosion and fatigue resistance. Their usage in complex designs has been limited by the manufacturing capabilities and high costs of traditional methods such as autoclave, pultrusion and resin transfer molding (RTM) (Caminero et al., 2018). Recent advancements in AM have overcome these challenges and allowed the fabrication of composite parts and complex geometries at affordable cost, time and less material waste using techniques such as fused deposition modeling (FDM) (Caminero et al., 2018; Parandoush & Lin, 2017).

Despite the advantages cited, the AM of composite FDM parts in particular still presents major challenges. Thermoplastics utilized in FDM possess lower elastic modulus than their injection-molding counterparts making the composite more susceptible to delamination (Caminero et al., 2018). Researchers have attempted to improve the mechanical, electrical or thermal properties of 3D printed polymers (Parandoush & Lin, 2017) through the insertion of short (Blok et al., 2018; Zhong et al., 2001) or continuous (Blok et al., 2018; Ning et al., 2017; Tian et al., 2016; van de Werken, Hurley, et al., 2019) fibers or nanofillers (Meng et al., 2017; Weng et al., 2016).

The effects of the different printing parameters, such as layer thickness, raster angle, fiber volume fraction, fiber orientation and printing direction on the performance of the composites have also been investigated (Tian et al., 2016; Wu et al., 2015). Tian et al. (2016) used a conventional 3D printer to infuse continuous fibers into Polylactic Acid (PLA) and optimized the liquefier temperature, layer thickness, hatch spacing, filament feed rate and printing speed to maximize the flexural strength and modulus.

A few other studies (Caminero et al., 2018; Zhang et al., 2018) have investigated the interlaminar bonding of 3D printed fiber-reinforced composites. Caminero et al. (2018) observed that the interlaminar shear strength (ILSS) of FDM polymers increases with the decrease of the layer thickness as the porosity in the composite decreases. Furthermore, the increase of the fiber content leads to an increase in the ILSS, yet far less than ILSS of composites based on pre-pregs due to the difference in matrix and fibers used in both methods and due to the fact that FDM is a vacuum-free technique that employs atmospheric pressure; far lower pressure than that in autoclaves, hence, resulting in low compaction and high interlaminar porosity.

The mechanical properties of 3D printed composites were previously explored (Blok et al., 2018; Ghebretinsae, 2019; van de Werken, Hurley, et al., 2019; Van Der Klift et al., 2016). Van Der Klift et al. (2016) experimentally determined the tensile properties of 3D printed continuous carbon fiber and nylon samples. The authors observed premature failure caused by discontinuities in the fiber path. They also reported that the porosity increases with the number of layers, which could substantiate the inaccuracy of the rule of mixtures for laminates with large number of fiber laminae. van de Werken, Hurley, et al. (2019) investigated the 3D printed composite via both experiments and finite element

analysis (FEA) and studied the influence of the fiber infill and geometry on the failure of these composites. Ghebretinsae (2019) performed tensile and flexural tests of carbon fiber-reinforced Onyx (matrix) samples to determine the material properties and assess the failure mode of the 3D printed composite. The author validated the experimental material properties using FEA and the rule of mixtures. It was observed that the FEA and the rule of mixtures were more conservative than the experiments and the delamination was the root cause of failure.

The strength of AM continuous fiber composites is also highly dependent on the fiber placement pattern and fiber volume fraction (van de Werken, Hurley, et al., 2019). The present work studies the effects of fiber placement on the mechanical (ultimate and interlaminar shear strength) and viscoelastic (stiffness and damping) properties of the AM composites by comparing two fiber patterns of the commercial composite 3D printer, Mark Two®. This FDM printer can produce fiber paths in any unidirectional orientation denoted as "isotropic fiber infill" although its name has no association with the traditional meaning of isotropic in material science. Alternatively, Mark Two® can place the fibers parallel to the boundaries of the part – "concentric fiber infill."

Previous studies used Mark Two® to demonstrate the advantages of continuous fibers including: a) customized-shaped fibers, in lieu of unidirectional lamina and multi-axial laminates, are promising in composite design and optimization as they can conform to any path on a 2D plane, including the optimized load path (Papapetrou, Patel & Tamijani, 2020; Tamijani et al., 2018). b) AM parts can be one to two orders of magnitude stronger and stiffer than unreinforced counterparts and can be lighter and almost as strong as aluminum alloys (van de Werken, Hurley, et al., 2019). c) They can attenuate distortion

and warping often observed in 3D printed polymeric composites (Crease, 2016a).

Furthermore, the thermomechanical behavior of different conventional fiber-reinforced composites (Capela et al., 2017; Feng et al., 2003; Goertzen & Kessler, 2007; Miyano & Nakada, 2006) and hybrid composites (Ayyagari, Al-Haik & Rollin, 2018; Gbaguidi et al., 2017), among other materials have been assessed using dynamic mechanical analysis (DMA). Goertzen and Kessler (2007) highlighted the usefulness of DMA in predicting the survivability of CFRPs under harsh environments while studying the effects of the heating rate and frequency on the glass transition temperature of the carbon fiber-reinforced resin. Feng et al. (2003) employed DMA to compare grafted and unsized short glass fiber-reinforced nylon composites emphasizing the effects of grafted fibers on the crystallization temperature, stiffness and strength of the material.

Capela et al. (2017) studied the effects of the short carbon fiber length on the strength and toughness of the material using tensile tests and DMA, verifying that the stiffness increased as the fiber length increased. Besides improving the mechanical properties of the non-reinforced polymer, short fibers are relatively more affordable and allow easy fabrication of composites. The only attempt to date was in determining the glass transition temperature of 3D printed continuous carbon fiber-reinforced composites using DMA (van de Werken, Hurley, et al., 2019).

A variety of thermoplastics, such as nylon, acrylonitrile butadiene styrene (ABS) and Polylactic Acid (PLA) are used as the matrix of AM composites. The present research utilized Onyx as a matrix; a thermoplastic made of nylon and chopped carbon fibers. Although some studies have used Onyx to investigate the mechanical properties (Ghebretinsae, 2019; Isobe et al., 2018; Sanei et al., 2019) and impact behavior (Scrocco

et al., 2018) of 3D printed composites, the material properties of Onyx obtained by experimental evaluations were presented for the first time in the current study.

2.2. Optimization of AM Composite Structures

The use of carbon fiber as a reinforcement in AM polymers has been extensively investigated and reviewed in the literature. However, the full potential of continuous fiber-reinforced composite AM has yet to be realized (Brenken et al., 2018; Hofstätter et al., 2017; van de Werken, Tekinalp, et al., 2019). Both short and continuous fiber reinforcements have been used in different AM technologies with varying degrees of success. While short fibers provide moderate improvements over the base polymer (van de Werken, Hurley, et al., 2019; van de Werken, Tekinalp, et al., 2019), continuous fiber reinforcements improve the polymer properties by 1-2 orders of magnitude, surpassing AM metals' specific mechanical properties (van de Werken, Tekinalp, et al., 2019).

Only a few studies to date have tried to utilize the advantage of fiber reinforcements and AM to enhance part performance (Brooks & Molony, 2016; Jiang, Hoglund & Smith, 2019; Li et al., 2020; Papapetrou, Patel & Tamijani, 2020; Saito et al., 2019; Sugiyama et al., 2020). Papapetrou, Patel and Tamijani (2020) introduced two topology-optimization schemes for AM part design, namely the solid orthotropic material with penalization (SOMP) and the level-set. An integrated fiber path optimization has been demonstrated using four methods of equally spaced (EQS), offset, streamline, and level-set fiber placement approaches (Papapetrou, Patel & Tamijani, 2020).

Improvements in stiffness of benchmark designs are demonstrated in the literature, although the feasibility of their manufacturing and experimental validations are not reported. In another study, Safonov (2019) presented a design optimization approach for the AM of orthotropic and transversely isotropic materials. They conducted the topology

optimization of 2D and 3D geometries based on the density distribution, resulting in structures 66% to 90% lighter than the initial design; no experimental validation was carried out. Brooks and Molony (2016) used a “force line approach” to place fiber-reinforced filaments along the load paths to design parts for AM. A pulley, a hook, and a universal joint were manufactured and successfully tested according to their proposed design methodology.

Jiang, Hoglund and Smith (2019) used the SOMP and continuous fiber angle optimization to perform the topology and fiber path optimization of AM composites subjected to volume constraints. The fibers, in this study, were printed parallel to the part's perimeter and along the principal stress directions. The authors observed that the stiffness of topology- and fiber path-optimized parts are enhanced compared to components optimized at a fixed unidirectional angle, demonstrating the fiber orientation's influence on the mechanical performance of the studied parts. They also verified that the minimum compliance is obtained when the printing plane is parallel to the applied load, yielding a 63% lower compliance than other printing orientations.

Most studies on design optimization of AM composites are focused on the numerical challenges of the problem and rarely on manufacturing and experimental investigation of optimized parts.

2.3. Design Optimization of Lattice Structures

Projection of homogenized designs is inspired by the work of Pantz and Trabelsi (2008), in which the homogenized properties of rank-two laminates were used to optimize microstructure topologies and the principal direction was utilized to optimize cell morphologies. A mapping function based on the optimized orientation was needed to project the homogenized design. However, since the optimized orientation was

symmetric with respect to π, a regularization approach was utilized to alleviate the discontinuities in the optimized orientation.

Optimization was performed using a coarse mesh. The optimized design was projected onto a fine mesh using a mapping function and optimized density to generate the lattice structure. Later, each of the three steps i.e., homogenization, regularization, and projection was enhanced in other research studies.

Groen and Sigmund (2018) interpolated the homogenized properties of a square cell with rectangular hole instead of using the explicit homogenized properties of rank-two laminates. They also introduced a connected-component labeling approach to simplify regularization. Allaire, Geoffroy-Donders and Pantz (2019) addressed the conformality of square lattices. They also used an abstract manifold for the computational domain to reconstruct lattice structures from optimized homogenized designs. The compliance-based lattice structure topology and morphology optimizations were also studied (Gharibi & Tamijani, 2021) using load paths and load flows as intermediate variables (Tamijani et al., 2018). Later, the optimization of material distribution and orientation and the subsequent projection for various types of cells and lattices using Fourier series representation was also investigated (Tamijani, Velasco & Alacoque, 2020).

Despite the success of stiffness-based de-homogenization approaches in generating lightweight periodic lattice structures, higher stiffnesses cannot be achieved if the stress constraints are not implemented within the optimization process and the optimized lattice structure fails. In addition, utilizing stress constraints may change the optimized lattice structure topology and morphology.

There are three sources of complexity associated with stress-constrained optimization

using homogenized properties: (1) stress singularities at zero density; (2) the large number of local stress constraints; and (3) the local nature of micro-stresses, which depends heavily on the cell micro-architecture.

In the context of macrostructure topology optimization, stress singularities at zero density are addressed by using a polynomial, Kreisselmeier-Steinhauser, or reciprocal function to smooth the feasible design space (Duysinx & Bendsøe, 1998; Rozvany & Sobieszczanski-Sobieski, 1992). The issue of large numbers of stress constraints has been addressed by aggregating the local constraints into a global constraint using the Kresselmeier-Steinhauser, p-norm, or p-mean functions (Duysinx & Sigmund, 1998; Yang & Chen, 1996). However, aggregations of stresses may not represent local stresses in structures. In order to preserve some of the local nature of the stresses while avoiding excessive computational cost, regional stress approaches have been proposed in which the design domain is split into several clusters and the stress constraints of the elements within each cluster are aggregated into a single constraint (Holmberg, Torstenfelt & Klarbring, 2013; Le et al., 2010).

Unlike the above two issues, i.e., stress singularities and large numbers of local stress constraints, which exist in both macro and microstructural optimization, macrostructure optimization with microstructural stress considerations is less investigated. Microstructural stress constraints can be implemented within the macrostructure optimization process using two approaches: (a) finding the effective allowable stresses and (b) amplifying the homogenized stress. Cheng, Bai and To (2019) investigated topology optimization of lattice structures with stress constraints. A cubic lattice structure with a single-density design variable was considered. The Hill's yield criterion was used

as the strength constraint. The effective yield strength in Hill's model was obtained by performing FEAs of lattice structures for various densities. Yu et al. (2020) studied topology optimization of shell-lattice structures with stress constraints. This study also used the Hill yield criterion. The effective yield strength was found for various densities. In both of these studies, a single design variable was employed to control the lattice structure topology.

However, to use the full potential of the lattice structures in perpendicular directions, two variables must be used to describe the cell. To this end, Donders (2018) studied minimization of the L2 norms of lattice structure stresses in square cells with rectangular holes using two variables. The effective stress was obtained using homogenized stress-strain relations. Then an amplification factor, which considered micro-stress fluctuations, was multiplied by the effective stress to mimic the microstructural stress.

While both stress amplification factor and effective allowable stress approaches were tested for microstructure topology optimization, cell orientations were kept unchanged in previous studies. However, various cells, such as square cells with rectangular holes that exhibit superior orthotropic properties, are weak with regard to withstanding shear stress. The orientation must be incorporated in the optimization process in order to take advantage of the orthotropic properties of the cell.

2.4. AM Wind Tunnel Models

Typical wind tunnel models are fabricated out of metals, wood, foam and fiberglass. Their manufacturing can be expensive, time-consuming and complex. Adding to the difficulty to build complex geometries is the fact that the models must conform to certain standards of surface finishing and tolerances. In addition, the real model and the prototype should have the same geometry, mass, stiffness, strength and dynamics (Zhu,

2019).

Researchers have found in AM a potential replacement for traditional fabrication methods for wind tunnel models. AM can reduce the cost and build time and fabricate complex shapes. Most common AM methods, stereolithography (SLA), selective laser sintering (SLS) and FDM, take about one day to fabricate a plastic wind-tunnel model while traditional ceramic or metal machined models take weeks to months to build (Aghanajafi & Daneshmand, 2010; Barlow, Rae & Pope, 1999). This facilitates possible corrections to the models by cutting their fabrication time and effort. In addition, internal structures and elaborated geometries can more easily be fabricated from a CAD model through AM contributing to the fulfilment of the mass and stiffness similarities (Zhu, 2019). The advantages of AM address some of the hindrances of traditional methods, creating possibilities for new design concepts.

AM models have also hitches due to the nature of the fabrication method and the material used. Plastic models cannot usually endure several test cycles (Aghanajafi & Daneshmand, 2010) and are not reliable at high speeds due to their low stiffness and strength (Zhu, Zhang & Li, 2019). To increase their stiffness, metal coating (Zhu, Zhang & Li, 2019) and inserts (Kroll, Artzi & Ralbag, 2010) and hybrid models (made of resin with metallic machined supports) (Zhu, Miao & Li, 2019) have been used. Recent advances in the AM of high performance plastics such as polyether ether ketone (PEEK) may lead to stiffer wind-tunnel models (Zhu, Zhang & Li, 2019).

On the other hand, the low stiffness or large flexibility might in fact be desirable and more representative of real models (Zhu, Zhang & Li, 2019). Also, the layer-by-layer nature of commonly used AM methods not only affects the material properties but results

in a stair step-effect in some geometries and low quality surface finish, requiring some post-processing such as sanding and painting (Zhu, 2019). Aghanajafi and Daneshmand (2010) have compared two missile models built of steel through binder jetting and machined. The models were tested in the wind tunnel and the aerodynamic coefficients were analyzed. The difference between the two models becomes more tenuous with the increase of the Mach number. Due to the limited accuracy in the aerodynamic response obtained from the AM models, several authors (Aghanajafi & Daneshmand, 2010; Kroll, Artzi & Ralbag, 2010) have advised the use of these models only at the early design stage.

Despite the aforementioned limitations, researchers have successfully taken advantage of AM to facilitate their studies for the different regimes up to hypersonic speed (Zhu, Zhang & Li, 2019). Different types of wind tunnel models, such as aircraft (Raza et al., 2021; Zhu, Zhang & Li, 2019), UAVs (2017; Junk, Schröder & Schrock, 2017), missiles (Aghanajafi & Daneshmand, 2010) models have been built through AM techniques demonstrating their viability. Zhu, Zhang and Li (2019) proposed a model with pre-deformation to compensate for the flexibility of the plastic models and reduce the resulting error. After comparing the aerodynamic performance of plastic AM models with metallic computational ones, the authors concluded that AM models could be reliably used in the transonic regime. Rêgo et al. (2018) built a hybrid model of an entrance ramp of a scramjet motor, with stainless steel and AM plastic. The model was tested for Mach 7 and 8.

The first attempt to manufacture a flexible wing model with internal structures was done by Pankonien et al. (2017). They additively manufactured a flexible wing model

and tested in the wind tunnel at subsonic speeds (less than 45 m/s). The different partitions of the wing were attached together through “interpenetrating fastening,” which extended throughout large regions, instead of glue or fasteners. This mechanism reduces stress concentration and grants accessibility to interior since it is not permanent. This interconnecting mechanism would be unfeasible for complex and more realistic models such as the one in the present study.

The aerodynamic loads and displacements are the important responses in the current study. The aerodynamic loads (normal, side and axial) and moments (yaw, pitch and roll) are measured by transducers in the force balance. Traditionally, displacements in wind tunnel models are measured using several strain gages or accelerometers (Kuester, Intaratep & Borgoltz, 2018). Alternatively, digital image correlation (DIC), laser interferometry and laser displacement sensors have also been used (Kuester, Intaratep & Borgoltz, 2018).

In the present study, DIC was utilized to measure the deformation. Contrarily to traditional deformation measurement methods, DIC has the ability of measuring the deformation field over a region without contact with the sample (Banks et al., 2015) and without disturbing the flow. Banks et al. (2015) demonstrated the accuracy and repeatability of DIC in measuring deformation of a sailing catamaran foil in a wind tunnel. For a range of wind speed and angles of attack, DIC revealed to be accurate for steady flow but its accuracy was limited by the DIC sampling rate for the unsteady flow. DIC was also utilized to demonstrate the interaction between the deformation and the angle of attack. After stall, the deformation tended to reduce the tip angle of attack.

Wind tunnel models are usually rigid and deformation corrections are often applied to

obtain a closer representation to the real models (Zhu, Zhang & Li, 2019). Despite the work of Pankonien et al. (2017), the present research aims to use the flexibility of AM and build the first flexible wing model with optimized internal structures. The model has been optimized by Locatelli, Mulani and Kapania (2011) for minimization of weight subjected to buckling and stress constraints. The design variables were the internal layout of the structure and the size of the skin panels, spars and ribs. The resulting optimized model has curvilinear spars and ribs which have been proven to enhance the aeroelastic performance (Fernandes & Tamijani, 2017; Locatelli, Mulani & Kapania, 2011).

3. Mechanical Characterization of 3D Printed Continuous Fiber-Reinforced Onyx Composites

This chapter identifies the fiber content of the commercial carbon filament and determines the effect of the continuous fibers and their layout on the interfacial strength and adhesion of AM continuous fiber composites. The failure mechanism of AM continuous fiber composites via experiments and FEA (using First Ply Failure and Progressive Failure) is characterized. Furthermore, we anticipate that the viscoelastic behavior of AM composites is different from traditional composites due to the nature of their manufacturing which entails high porosity. Therefore, DMA was utilized to obtain the thermomechanical properties (stiffness and damping) of AM under temperature and frequency sweep. Finally, the effects of continuous fibers on the glass transition temperature of the polymer and prevention of failure due to creep were investigated. The work of this chapter has been published in (Fernandes, Tamijani & Al-Haik, 2021).

3.1. Experimental Procedure

This subsection discusses the material and printing settings used in this chapter. Three types of experiments were performed: interlaminar shear test, tensile test and dynamic mechanical analysis. The theory and formulation about the three tests are also discussed.

3.1.1. AM Process and Materials

The continuous fiber composite samples in this research were manufactured using a Mark Two® composite 3D printer (refer to Figure 3.1). This printer has one print head with a double nozzle system that prints the polymer and fiber-matrix filament separately onto an unheated print bed at nozzle temperatures of 252 °C and 275 °C, respectively. The plastic nozzle is made out of brass with a steel tip while the fiber nozzle is entirely made out of brass. The printing parameters are summarized in Table 3.1. Since the print

speed is not disclosed by Markforged, the author estimated it to be around 14 mm/s.

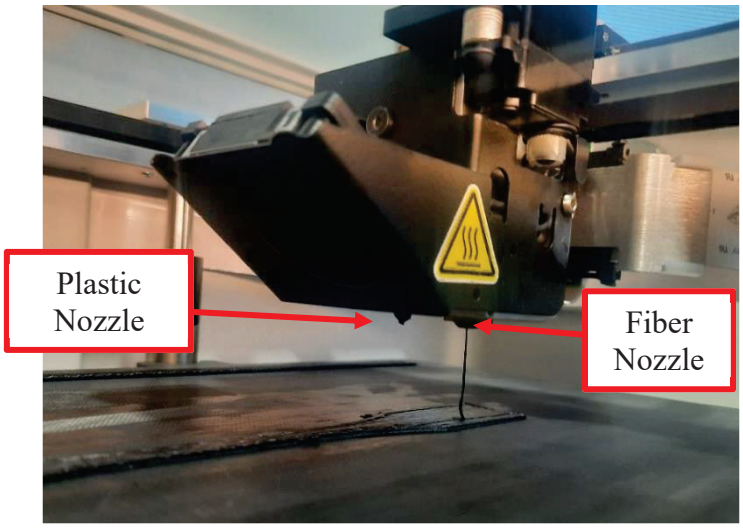

Figure 3.1 Printhead illustrating printing process.

Table 3.1

Print Settings

Parameter	**Value**
Print Speed	14 mm/s
Plastic Nozzle Temperature	252 °C
Fiber Nozzle Temperature	275 °C
Bed Temperature	Unheated
Layer Height	0.125 mm
Infill Density	100%
Filament Spacing	0 mm

The materials utilized are Markforged® carbon filament and a Markforged® Onyx.

Onyx is a Markforged® proprietary thermoplastic made of nylon and chopped carbon fibers. The microscale carbon fibers make Onyx 3.5 times stiffer than neat nylon and reduce shrinkage and warping (Crease, 2016b). Due to the inclusion of chopped carbon fibers, Onyx exhibits a higher toughness and heat resistance than other AM polymers, such as nylon and ABS (Crease, 2016b).

Markforged® carbon fiber-matrix filament is also a composite on its own, as it comprises microscale continuous carbon fibers embedded in an unknown polymer that melts when the filament is extruded from the nozzle providing adhesion to the tooling surface and polymer. The carbon fiber-matrix filament is molten into approximately 1 mm-wide and 0.125 mm-thick paths (van de Werken, Hurley, et al., 2019) with no polymer in between the adjacent printed fibers. To examine the fiber volume fraction of the continuous carbon fiber-matrix, filaments of unprinted Markforged® carbon fiber-matrix were mounted in an epoxy mold and allowed to cure. The sample in the mold was ground with 800, 1000 and 1200-grit silicon carbide papers and polished, according to (ASTM) before being observed under an Olympus metallurgical light microscope.

The micrograph in Figure 3.2 shows that the actual microscale carbon fibers are randomly distributed in the composite filament. The microscopic image was processed using ImageJ® software, which determines the percentage of white (fibers), or grey (matrix) area within the area of interest (inside the red line in Figure 3.2). The fiber volume content was determined to be around 30% by volume. This reveals that Markforged® parts have rather a substantially lower carbon fiber content compared to traditional unidirectional carbon fiber-reinforced laminate. This fact, adding to the inherently high porosity of FDM parts discussed in later sections, compromises the

strength and stiffness of these AM composites. Throughout this manuscript, we will refer to the fiber filament volume fraction of different samples without considering the 30% factor.

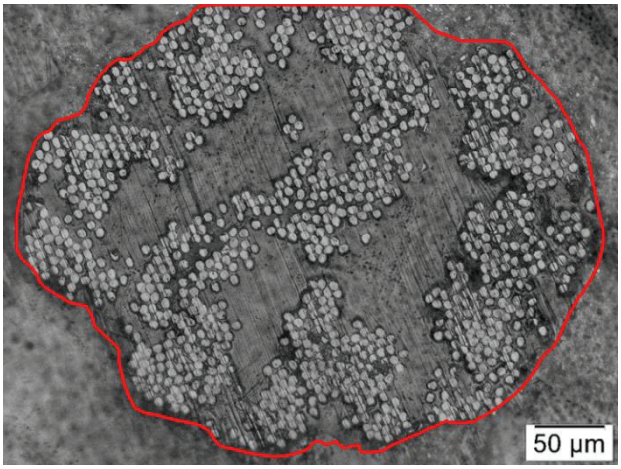

Figure 3.2 Light microscopy micrograph of strands of carbon fiber filament mounted in an epoxy mold.

In this study, three samples were studied: Markforged® "isotropic" and concentric fiber infill and neat Onyx. "Isotropic" fibers are continuous strands of unidirectional fibers and have no resemblance to the traditional meaning of isotropic in material science. Isotropic fibers provide resistance in the XY plane (Crease, 2016c). Alternatively, the fibers can be laid down parallel to the perimeter of the model; called "concentric" fibers, providing flexural strength and preventing deformation at the edges (Crease, 2016c). The two described layouts are illustrated in Figure 3.3 in which the polymer and the fibers are represented by white and yellow lines, respectively. For the geometry and dimensions in Figure 3.3, the concentric fibers are printed from the outer edge towards the center of the geometry leaving a gap in the middle, which is filled with polymer since there is not

enough space for an additional fiber. Such a gap is not observed in isotropic fiber infills since the plastic (white zigzag lines) is deposited near the edge if necessary to ensure no discontinuity in the middle. Gaps between the adjacent filaments or due to change in the filament path are known to cause stress concentration and premature failure (Ahn et al., 2002; Gibson, Rosen & Stucker, 2014).

Regardless of the fiber layout, Mark Two® prints the first and last layer and at least a wall around the contours of the printed model made of Onyx. Onyx layers are alternately printed at ±45°. The present research studies the effects of these two-fiber layouts on mechanical properties (stiffness and tensile and interlaminar shear strength), failure mode and thermomechanical properties (glass transition temperature, creep rate and activation energy of glass transition) of AM polymers.

(a)

(b)

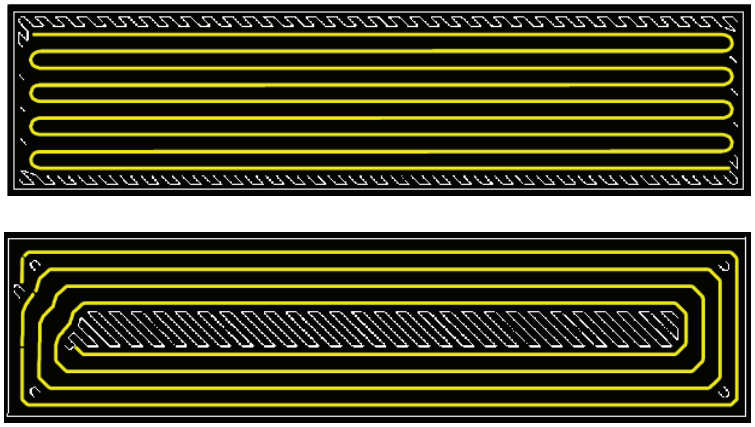

Figure 3.3 AM fiber layout for DMA coupons: a) isotropic fiber sample; and b) concentric fiber sample.

3.1.2. Interlaminar Shear Test

Since delamination is one of the most common failure mechanisms in laminated

composites, the interlaminar shear test was conducted to study the resistance to delamination of AM composites. Five isotropic, concentric and Onyx samples were subjected to interlaminar shear tests according to International (2016). The specimens had a 26 mm span, 13 mm width and 52 0.125 mm-layers. The isotropic and concentric samples, with fiber layouts similar to the ones in Figure 3.3 had 66.02% and 66.67% fiber volume fraction, respectively.

The maximum interlaminar shear strength (ILSS) of a short beam of a cross-sectional area A can be determined through a three-point bending test with a maximum load of P, and it is translated by the following expression:

$$\mathrm{ILSS} = \frac{3}{4}\frac{\mathrm{P}}{\mathrm{A}} \tag{3.1}$$

The test was performed using a CA43.504 MTS Electromechanical test machine at a constant crosshead displacement rate of 1 mm/min and was terminated when the load declined about 30% as per International (2016). The diameter of the support and applied load cylinders, shown in Figure 3.4, are 5 and 10 mm, respectively. Force were registered by a 50 kN load cell.

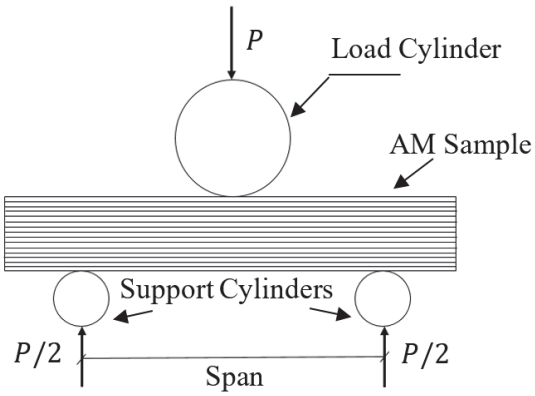

Figure 3.4 Schematic of the interlaminar shear test.

3.1.3. Tensile Test

To understand the effects of the fiber path on the mechanical properties (stiffness and strength) and failure mechanism of AM polymers, tensile tests were performed using a CA43.504 MTS Electromechanical test machine. First, the material properties of the composite and of Onyx were determined. For that effect, carbon fiber composite specimens with 0°, 90° and 45° fiber orientation were tested and their stress-strain curves plotted to obtain E_1 and σ_{1T} (from 0°), E_2 and σ_{2T}, (from 90°) and E_x (from 45°). E and σ are the elastic modulus and the ultimate strength, respectively. The subscripts 1 and 2 indicate the fiber and matrix directions in the material coordinate system, and *x* is in the global coordinate system.

The major Poisson's ratio (ν_{12}) was obtained by dividing the lateral strain by the longitudinal strain when the load is applied longitudinally, and the minor Poisson's ratio was obtained via the Betti's reciprocal formulation: $\nu_{21} = \frac{\nu_{12}E_2}{E_1}$. The shear modulus G_{12} was computed from the transformation equation of the engineering constant:

$$\frac{1}{\mathrm{E_x}} = \frac{1}{\mathrm{E_1}}\cos^4\theta + \left(\frac{1}{G_{12}} - \frac{2\nu_{12}}{E_1}\right)\cos^2\theta\sin^2\theta + \frac{1}{E_2}\sin^4\theta \tag{3.2}$$

where $\mathrm{E_x}$ is the transformed axial modulus at a fiber orientation $\theta = 45°$ (Jones, 1998).

The Onyx and fiber-reinforced samples were prepared and the tests were carried out according to ASTM D638-14 (specimen Type II) and D3039/D3039M-17, respectively. Onyx was subjected to compressive loads to obtain its compression strength (ASTM, 2010). The dimensions of the tensile test specimens are reported in Table 3.2. With fiber layouts shown in Figure 3.5, they had 72.13% fiber volume fraction, distributed within six layers out of a total of eight layers. The top and bottom layers are made of Onyx only.

In Figure 3.5, the fibers are represented by yellow lines and Onyx by white lines or grey in the case of neat polymer sample. The 0° and concentric fiber-reinforced samples were printed with polymeric tabs with a bevel angle of 7°.

Table 3.2

Dimensions of tensile specimens in mm

Specimen	**Total Length**	**Gauge Length (L_0)**	**Width**	**Thickness**
0° Isotropic Fibers	250	138	15	1.3
90° Isotropic Fibers	175	125	25	2.0
45° Isotropic Fibers	167	92	10	1.9
Concentric Fibers	250	138	15	1.3
Onyx	183	117	6.5	3.0

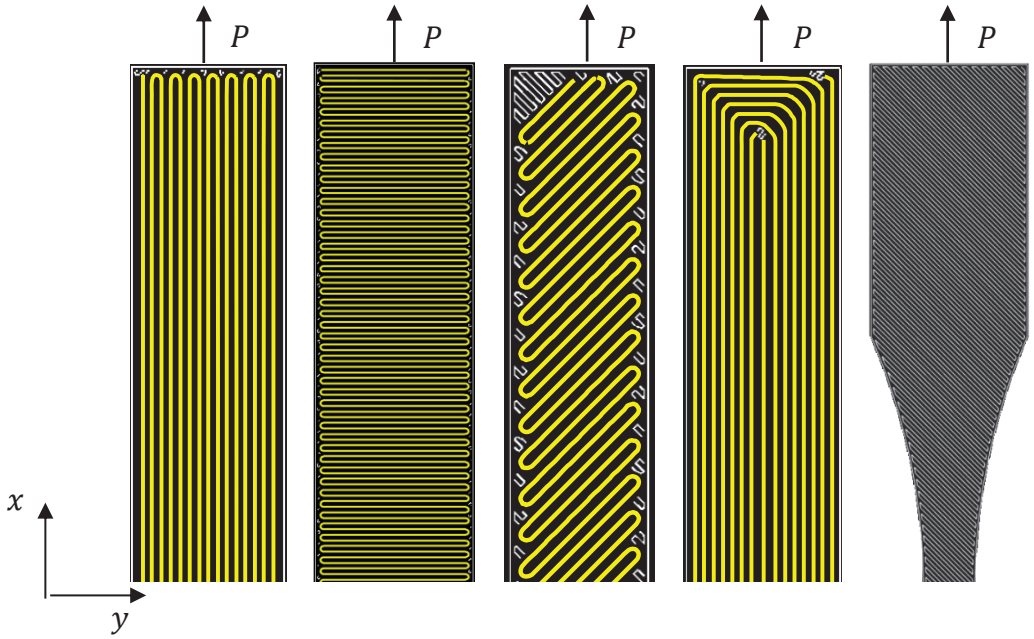

Figure 3.5 Section of the tensile test specimens: 0°, 90° and 45° isotropic fiber patterns; concentric fiber pattern and Onyx specimen (from left to right).

The force was recorded by a 50 kN load cell and the strain was computed using DIC with two cameras from Correlated Solutions, Inc. The fractured surface of the reinforced samples was observed under a FEI Quanta 650 scanning electron microscope (SEM) to identify the mode of failure.

3.1.4. Dynamic Mechanical Analysis

Elevated temperatures accelerate the viscoelastic behavior as the molecules in the matrix material are perturbed and the space for molecular motion is increased (Menard & Menard, 2002). The polymeric matrix becomes softer and eventually transitions to a rubbery state, compromising its mechanical stiffness and creep resistance. The temperature at which polymers transition from glassy to rubbery state is called glass transition temperature, T_g, and it can be determined using the DMA temperature sweep.

For most applications, such as load-bearing applications, the polymer should operate at temperatures below its T_g. Other applications, in which the polymer is used as flexible rubber or sealant, for example, it is desirable to keep the temperatures above T_g (Hale, 2002). Several experimental techniques including DMA and differential scanning calorimetry (DSC) can be utilized to measure T_g, with a variation of about 25 °C among these different methods (Goertzen & Kessler, 2007; Menard, 2008).

When measured at different frequencies (f), the glass transition temperature can be employed to estimate the activation energy of glass transition (ΔH). This can be mathematically expressed by (Goertzen & Kessler, 2007):

$$\Delta H = -R \frac{d(\ln(f))}{d\left(\frac{1}{T_g}\right)} \tag{3.3}$$

where R is the universal gas constant. The activation energy is the energy required for

a molecule of a polymeric chain segment to ‘‘jump’’ to a nearby empty molecular space or chain-segment size. It can be used to predict the creep rupture, the stiffness of the material at the end of its service life (Rudin & Choi, 1999) and changes under harsh environments or aging (Karbhari & Wang, 2004).

The 40.0 mm × 10.0 mm × 0.7 mm (2015) continuous carbon fiber composite coupons, with isotropic fiber reinforcement, concentric fiber reinforcement and no reinforcement (i.e., 100% Onyx), were printed using the Mark Two® printer. The reinforced samples comprise six layers, four of which are made of carbon fiber composite. The top and bottom layers are made of Onyx only. The isotropic and concentric fiber-reinforced samples (Figure 3.3) have 40.5% and 39.0% fiber filament volume fractions, respectively.

The viscoelastic behavior of AM continuous fiber composites was evaluated using a Perkin Elmer DMA 8000 according to ASTM D4056-12 [50]. The samples were mounted using a 3-point bending fixture and the tests were run at a heating rate of 2 °C/min (except for Onyx which was run at 0.5 °C/min) (ASTM, 2015) and maximum strain of 0.005; within the elastic region. Through several trials, it was found that at 0.5 °C/min was the heating rate that allowed Onyx to achieve thermal stability and better capture its viscoelastic behavior.

The first study was conducted at a constant frequency of 1 Hz while heating the sample from 30 °C to 160 °C. Next, to simulate isothermal environments, the frequency was swept from 1 Hz to 100 Hz while maintaining the temperature at 30 °C. On a third study, the temperature was again varied as before but for different constant frequencies (10 Hz, 30 Hz and 50 Hz) to determine the activation energy.

3.2. Results and Discussion

This subsection discusses the results of the interlaminar shear test, tensile test and the dynamic mechanical analysis. The results of the computational and experimental failure analysis are also presented.

3.2.1. Interlaminar Shear Test

The fiber/matrix interlayer bonding dictates the strength of a composite (Caminero et al., 2018; Hou et al., 2020). Additively manufactured composites are fabricated at low pressures relative to traditional composites resulting in high porosity and low strength (Caminero et al., 2018) and premature failure. In addition, FDM parts require adequate residual heat energy to allow proper interlayer bonding (Gibson, Rosen & Stucker, 2014). Therefore, this section analyzes the interlaminar bonding of AM continuous fiber reinforced samples. Since the ILSS is a characteristic of laminates and FDM parts are built layer-by-layer, the ILSS of neat Onyx samples were also assessed.

The 3-point bending of the printed composite short beams was performed, and the post-test analysis, in Figure 3.6 (a) and (b), showed that the cracks propagate transverse to the bending direction and the predominant mode of failure of the composites samples was interlaminar shear (delamination) which emphasizes the poor adhesion between fiber/matrix layers. On the other hand, the Onyx samples displayed a crack propagating at the midspan of the sample from the bottom upwards (Figure 3.6 (c)). The plastic deformation is visible in the plot of ILSS vs. deformation in Figure 3.7.

The results of the interlaminar shear test for the three samples are compared in Figure 3.7. These results are based on the average of 5 samples per configuration. As expected, the Onyx samples exhibited high plasticity and had a bonding strength lower than the continuous fiber-reinforced samples. In fact, Table 3.3 shows that, regardless of the fiber

layout, the continuous fibers tripled the ILSS of Onyx. After reaching the average ILSS, the Onyx curve drops drastically indicating that their failure rapidly and catastrophically propagates through the layers after fracture initiates in contrast with the fiber-reinforced samples for which the strength gradually decreases after failure.

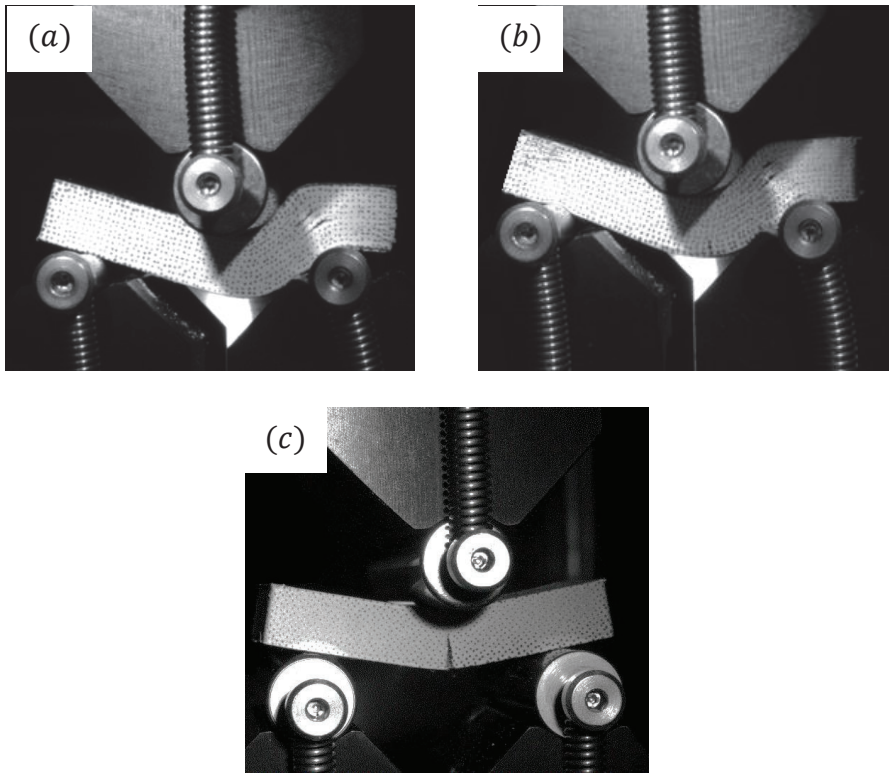

Figure 3.6 Failed interlaminar shear test samples: (a) isotropic infill; (b) concentric infill; and (c) Onyx sample.

In addition, Figure 3.7 shows that both fiber configurations displayed identical stiffness as their strength raises at the same rate. The difference in the ILSS of the two samples could arise from the 0° and 90° fibers in concentric layout. The interlaminar shear stresses are dependent on the fiber orientation through changes in the stiffness matrices and the elasticity solutions of anisotropic plates (Pipes, 1971; Pipes & Pagano,

1970). Similar to a cross-ply, although not a perfect cross-ply, concentric samples are more prone to delamination due to interlaminar shear than a unidirectional lamina. This leads to smaller ILSS as manifested in Figure 3.7.

After reaching the ILSS and delamination starts, the average curve for the isotropic samples seems to drop at a faster rate than the concentric samples indicating that the latter is more ductile due to the middle polymeric region and carries the load more efficiently. The steeper descent for the isotropic samples indicates that delamination is propagating at a faster rate.

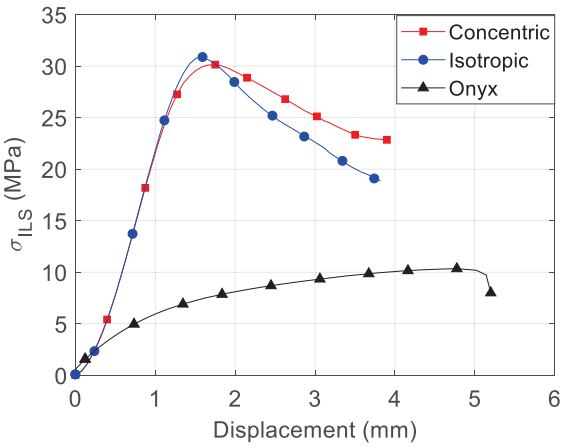

Figure 3.7 Average ILSS vs displacement for the three samples.

Overall, these ILSS for the continuous fiber-reinforced samples are consistent with the results obtained by Caminero et al. (2018). Those authors reported an ILSS of 31.94 MPa for an AM unidirectional carbon fiber-reinforced sample made of nylon with 73.2% (composite) fiber volume fraction. Furthermore, while the present results clearly demonstrate the enhancement in the interlaminar strength caused by introducing

continuous carbon fibers, the performance of AM composites is still not comparable to the traditional composites due to the high porosity discussed at the beginning of this section. In fact, Caminero et al. (2018) reported an ILSS of over 90 MPa for a pre-preg composite made of 59.8% high strength carbon fiber and epoxy. It is worth to highlight that the matrix and fiber in the pre-preg composite were different and the fiber volume fraction of the pre-preg composite is actually higher than the AM composites in the current study, as discussed in section 3.1.1.

Table 3.3

Average ILSS for the three printed configurations

Samples	**ILSS (MPa)**
Concentric Fibers	30.26 ±3.12
Isotropic Fibers	30.99 ±2.23
Onyx	10.75 ±1.30

3.2.2. Tensile Test

Five samples per configuration were tested and their representative stress-strain curves are shown in Figure 3.8. The material properties of the carbon fiber composite and the Onyx are reported in Table 3.4. E_1 and E_2 are the slopes of the linear portion of the stress-strain curve for the composite with isotropic fibers oriented at 0° and 90°, respectively. σ_1 and σ_2 are the axial and transverse strengths for the composite with isotropic fibers oriented at 0° and 90°, respectively. $E_x = 5.55\ GPa$ obtained from the tensile test of a 45° fiber-reinforced composite was applied to equation (3.2), giving $G_{12} = 2.53\ GPa$.

The compression strengths (σ_{1C} and σ_{2C}) for the composite were obtained by simulating a compression test in MSC Nastran for two laminate models with fibers oriented at 0° and 90° according to ASTM D6641 (2001). The shear strength (τ_{12}) was then determined using Tsai-Wu and Tsai-Hill failure criteria using the data for the tensile test of the 45° fiber infill specimen.

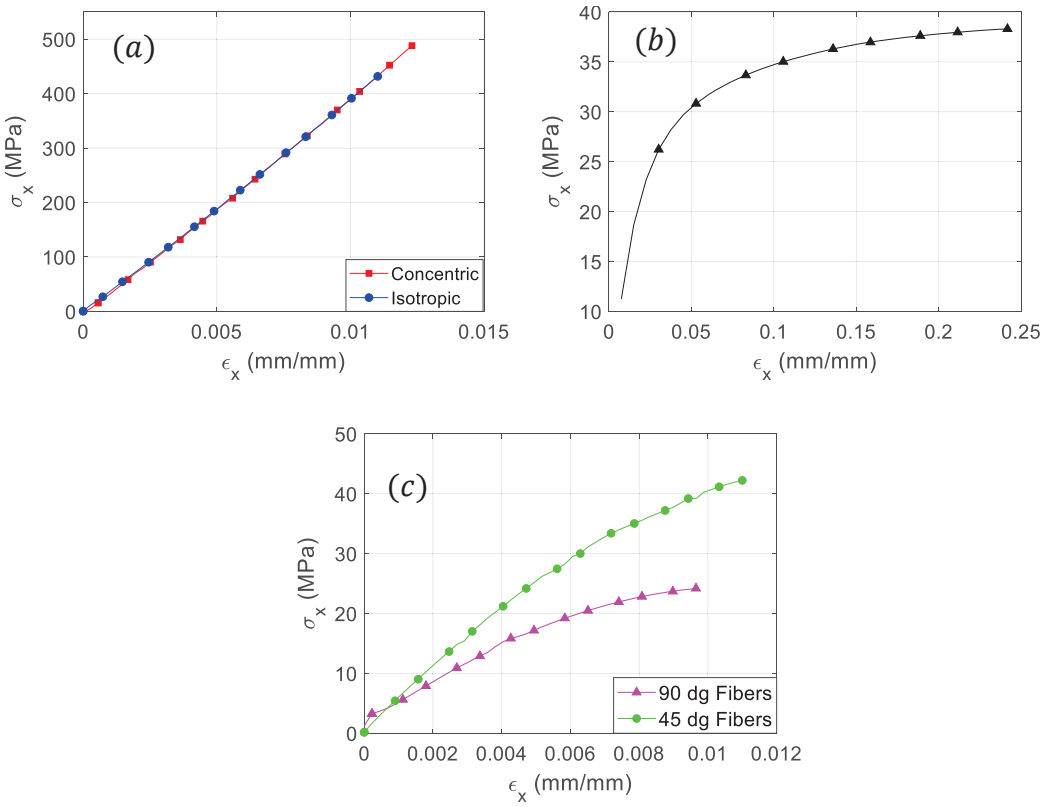

Figure 3.8 Average stress-strain curve for the three samples: a) 3D printed continuous fiber sample; b) onyx sample and c) 90° and 45° isotropic fiber-reinforced samples.

The rule of mixture is often used to determine the material properties of conventional composites. However, it assumes among other aspects a perfect adhesion between fiber and matrix with no voids which is not the case for AM composites. Using the material

properties for the fiber-filament and Onyx in Figure 3.4 and for a 72.13% fiber-matrix volume fraction, the following effective properties are obtained: $E_1 = E_{1f}V_f + E_{1m}V_m = 38.00\ GPa$ and $\sigma_1 = \sigma_{1f}V_f + \sigma_{1m}V_m = 515.48\ GPa$. Note that these results from the rule of mixture are within a 9% difference with the experimental values ($E_1 = 39.35\ GPa$ and $\sigma_1 = 471.95$ GPa) validating the test.

Table 3.4

Mechanical properties of the carbon fiber composite and Onyx

Property	**Isotropic Carbon Fiber Composite**	**Carbon-matrix filament**	**Onyx**
$\boldsymbol{E_1}$ **(GPa)**	39.35 ±0.18	52.00	1.75 ±0.02
$\boldsymbol{E_2}$ **(GPa)**	3.14 ±0.08	4.00	1.75 ±0.02
$\boldsymbol{\nu_{12}}$	0.34	0.33	0.36
$\boldsymbol{G_{12}}$ **(GPa)**	2.53	2.00	0.64
$\boldsymbol{\sigma_{1T}}$ **(MPa)**	471.95 ±32.53	700.00	37.96 ±3.52
$\boldsymbol{\sigma_{1C}}$ **(MPa)**	-216.00	-320.00	-78.27 ±4.05
$\boldsymbol{\sigma_{2T}}$ **(MPa)**	24.52 ±1.25	48.00	37.96 ±3.52
$\boldsymbol{\sigma_{2C}}$ **(MPa)**	-81.38	-100.00	-78.27 ±4.05
$\boldsymbol{\tau_{12}}$ **(MPa)**	43.82/44.30*	73.00	48.60

Note: the material properties for carbon-matrix filament were obtained from (Van Der Klift et al., 2016). *Allowable shear strength obtained using Tsai-Wu and Tsai Hill failure criteria.

In addition, it is well known that fiber-reinforced composites are designed to carry the load in the fiber direction. Transverse loads can cause early failure since the composite

transverse strength can be lower than the strength of the matrix itself as it is dependent on the matrix strength, imperfections and adhesion between matrix and fibers (Callister Jr & Rethwisch, 2020). This was observed in the present study in which σ_{2T} for the composite is lower than that of the Onyx. Also, the Onyx is stronger in compression than in tension since the cross-sectional area increases during compression as the specimen is crushed and the flaws are filled. In tension, however, the cross-section becomes thinner and the presence of flaws can initiate premature failure.

As shown Figure 3.8, the 3D printed 0° isotropic and concentric fiber composite samples exhibited a linear elastic behavior as their stress-strain curves steeply rise until the samples catastrophically failed. On the other hand, the remaining isotropic samples and the Onyx samples exhibited elastic-plastic transition while the Onyx sample deformed considerably more than the fiber-reinforced samples. Table 3.5 summarizes the results for the tensile test. The continuous fibers reinforced samples are ~23 times stiffer than the Onyx samples. They are also 14 (concentric fibers) and 12 (isotropic fibers) times stronger than the Onyx samples proving that continuous fibers can be used to improve the mechanical properties of the 3D printed polymers.

The post-test fiber-reinforced samples is shown in Figure 3.9. The fracture pattern suggests that they partially crack longitudinally along the fiber direction forming two samples with smaller areas that carry the same load and double the stress of the initial sample. The increase in stress causes one of this smaller samples to crack transversely. For the unreinforced samples, on the other hand, the cross-sectional area becomes smaller at the gauge region (Figure 3.9) forcing the stresses to be higher there and consequently, the specimens failed in that region.

Table 3.5

Tensile properties of AM composite samples

Samples	E_x **(GPa)**	σ_x **(MPa)**
Concentric Fibers	39.88 ±0.45	546.35 ±35.80
Isotropic Fibers	39.35 ±0.15	471.95 ±32.53
Onyx	1.75 ±0.02	37.96 ±3.52

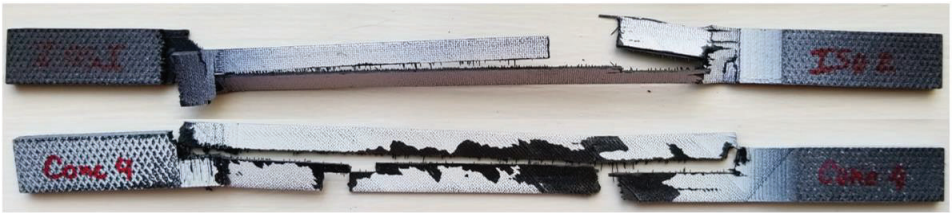

Figure 3.9 Fractured AM continuous fiber-reinforced composite from tensile test: isotropic fiber sample (top) and concentric fiber sample (bottom).

The two fiber-reinforced configurations differ on the tab section and in the middle region along the longitudinal direction of the sample as can be observed from Figure 3.5. The similarities in the gauge area made the two AM continuous fiber reinforced samples displace equally under the same load explaining their identical stiffness. Despite the similarities in stiffness and failure pattern, the isotropic and concentric fiber-reinforced samples reveal a very distinct strength. To better understand this disparity, the micrographs of the failed cross-section for the two samples were analyzed using a scanning electron microscopy (SEM, FEI Quanta 650 from Fisher Scientific) after being gold-sputtered to increase conductivity.

As revealed in Figure 3.10 (a), the isotropic samples experienced some fiber breakage, but matrix failure was more predominant. The micrographs of the isotropic fiber-reinforced samples show large cracks propagating around the fibers and through the

matrix and fibers pulled out from the matrix. This behavior is caused by poor adhesion between fiber filament and Onyx.

On the other hand, Figure 3.10 (b) shows that the concentric samples failed due to fiber breakage, i.e., the fibers gradually fractured allowing the other fibers to still carry load resulting in a strength higher than the isotropic samples. To validate the experimental observations, the two AM continuous fiber composite samples were modeled in MSC PATRAN/Nastran FEM software and their failure behavior was analyzed.

The samples were modeled as 8 layer-laminates with 35000 CQUAD4 elements. The fiber patterns were obtained from Markforged software, Eiger.io and since the fibers are not unidirectional, a different laminate property was generated for each element in PATRAN. Each property was created with the angle of the fiber passing through its centroid. The samples were clamped on one end and stretched on the other end as shown in Figure 3.11. The failure analysis was performed through static analysis using the Tsai-Wu Failure Criterion and through Progressive Failure using Hashin Failure Criterion.

The simulation demonstrates that the stresses are carried mostly by the fibers, i.e., the stress in the fiber direction is the most determinant in the failure analysis as shown in Figure 3.12. The gauge area is under high stresses that are uniformly distributed in that region. The failure indices for the isotropic pattern using the two failure criteria is depicted in Figure 3.13. The models predict failure near the tabs in the transition corner between the Onyx and fiber-matrix filaments indicated with a circle in Figure 3.13. However, the failure indices are approximately uniform in the gauge region indicating that failure may occur anywhere in that region. The presence of voids or defects, common

in AM composites, as shown in Figure 3.14 could initiate failure. The location of failure predicted by the FEA is consistent with the experimental observations (Figure 3.9).

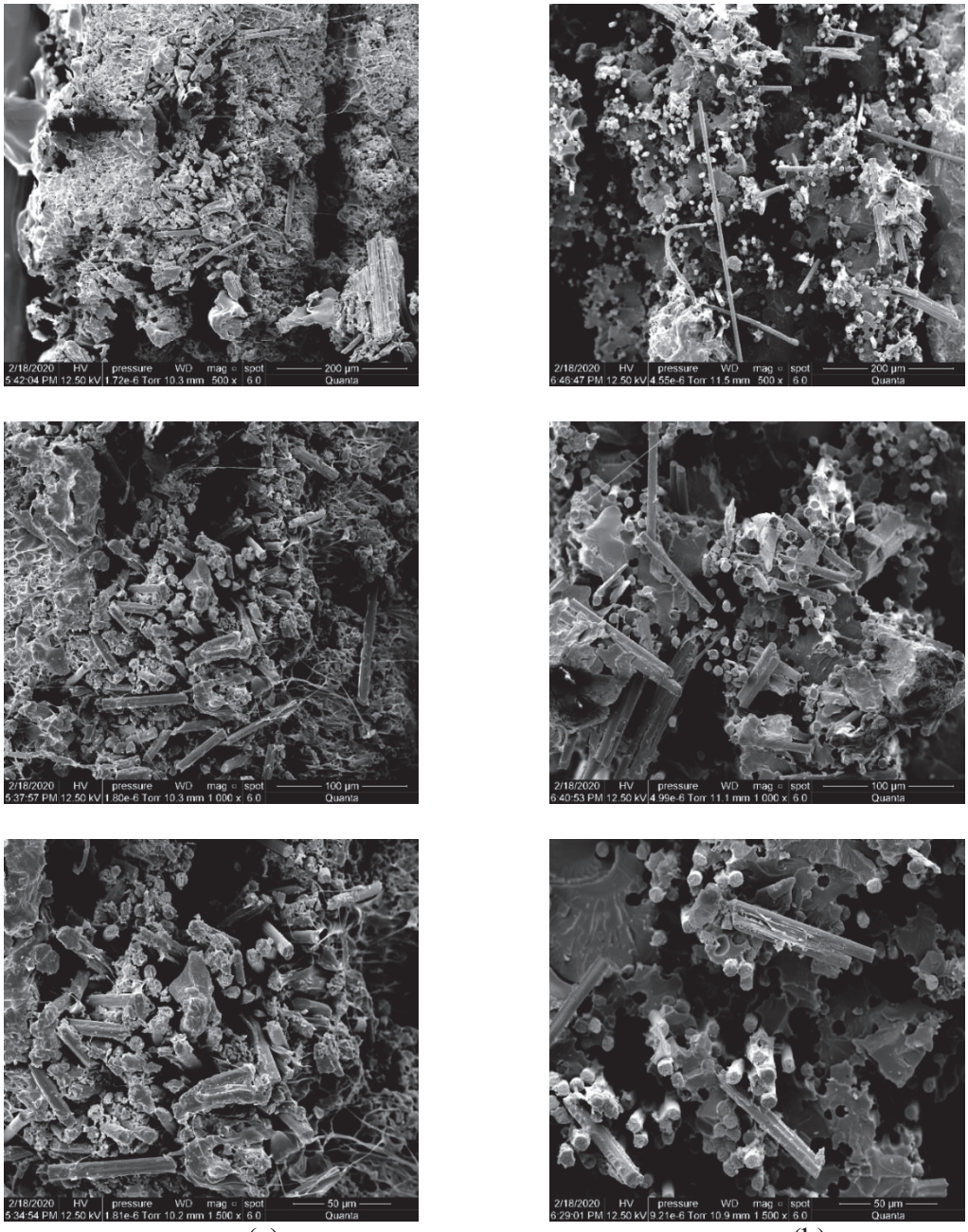

Figure 3.10 SEM micrographs of the fractured cross-section for (a) isotropic fiber and (b) concentric fiber layouts.

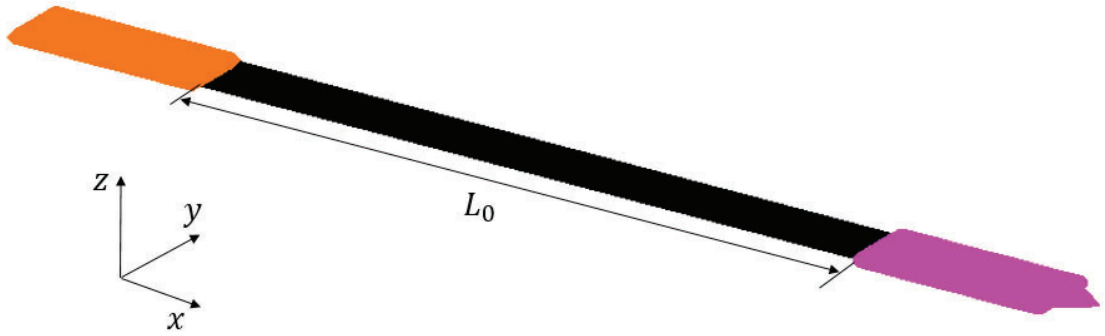

Figure 3.11 Tensile specimen with orange nodes clamped and pink nodes under tension.

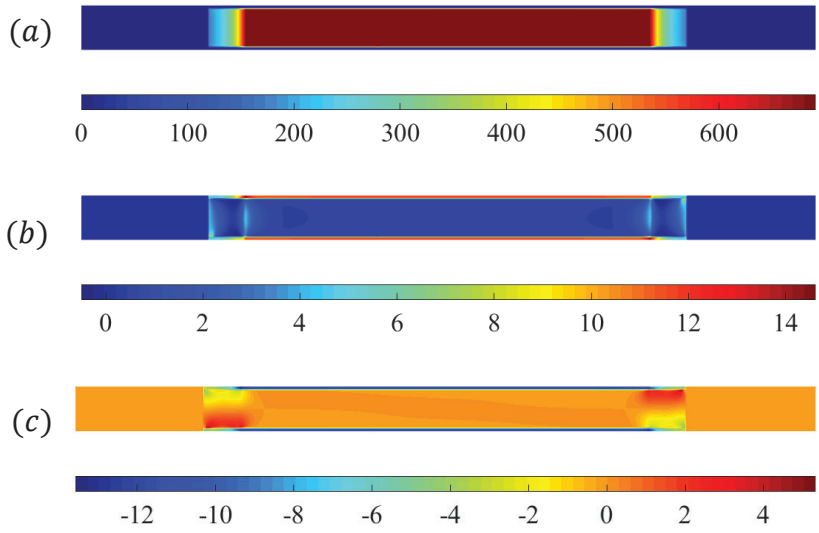

Figure 3.12 Stresses in the isotropic fiber pattern for the linear analysis at failure load: (a) normal stress in the fiber direction σ_1 [MPa] (b) normal stress perpendicular to the fiber direction σ_2 [MPa] and (c) shear stress τ_{12} [MPa].

Furthermore, since all the fiber-matrix layers have the same fiber orientation and stresses, the Hashin Criterion predicts that all fiber-matrix layers fail at once due to fiber tension. Table 3.6 compiles the failure loads for the isotropic fiber pattern. Tsai-Wu and Hashin Criteria estimate failure at 9535 N and 9015 N. The FEA results agree with the experimental observations with less than 3.58 % difference, except for the failure mode. According to the micrographs (Figure 3.10), the experimental model showed poor

bonding between layers and fiber pullout. However, the FEA does not consider the interaction between layers and only evaluates failure within the ply. Therefore, the finite element model (FEM) predicts failure due to fiber tension.

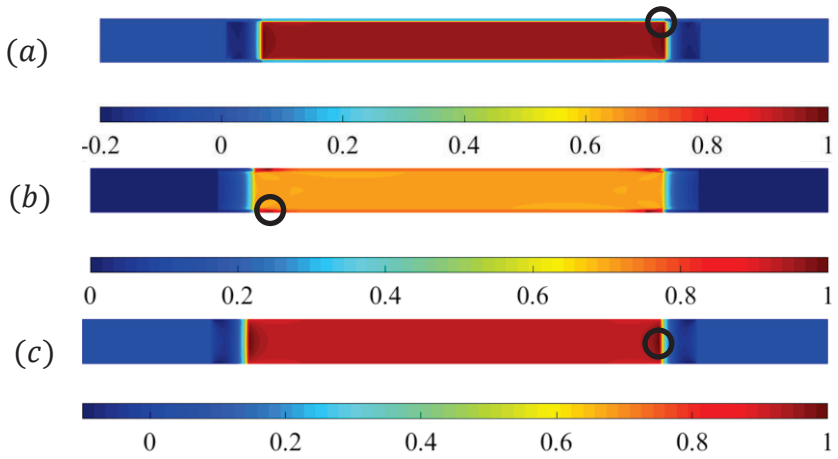

Figure 3.13 Failure index for isotropic fiber-reinforced samples: (a) 8-layer-laminate using Tsai-Wu criterion; (b) 8-layer-laminate Hashin/progressive failure criterion; and (c) equivalent model using Tsai-Wu criterion.

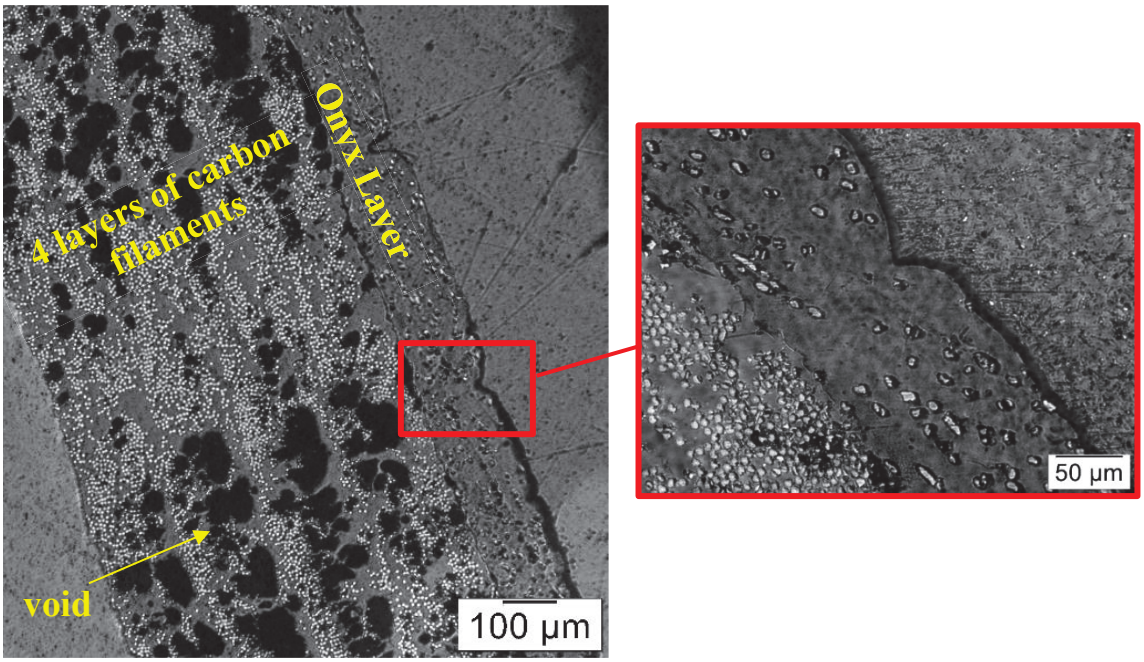

Figure 3.14 Micrograph of 3D printed composite with four fiber-matrix layers.

An equivalent model of AM specimen with continuous fibers and Onyx was created in FEA as a single lamina using the properties from the tensile test in Table 3.4. The results shown in Figure 3.13 c) indicate failure in the gauge region near the tap at an axial load of 8364 N. As shown in Table 3.6, the results are in agreement with the experiment and the other FEMs. In addition, this simplified model reduced the computational time of analysis by half of the other FEMs indicating that the equivalent model can replace the other models.

Table 3.6

Comparison of failure load in the isotropic fiber infill samples using different methods

Isotropic	**Failure Load (N)**	**% difference**
Experimental	9344 (±650.00)	---
8 layer-laminate, Tsai-Wu	9535	2.02
8 layer-laminate, Hashin/ Progressive Failure	9015	3.58
Equivalent model, Tsai-Wu	8364	11.07

A similar analysis can be performed for the concentric fiber infill. Once again, an 8-layer laminate was analyzed using the Tsai-Wu criterion and Hashin Progressive Failure. The failure indices are shown in Figure 3.15. The line near the middle of the sample indicates the existence of a small (<1mm) space between adjacent fibers due to a larger hatch distance. The gap causes failure near the grip due to fiber tension at 9224 N according to Tsai-Wu criterion and 9364 N according to Hashin criterion (Refer to Table

3.7). Although the two FEMs agree with each other, they have ~16% difference when compared to the experimental failure load. This difference can be attributed to small discrepancies in the printed fiber layout and that of the FEA.

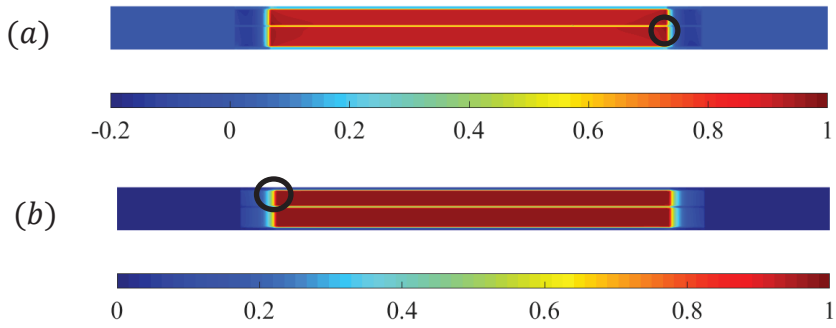

Figure 3.15 Failure Index for concentric fiber-reinforced samples: (a) 8-layer-laminate using Tsai-Wu Criterion; and (b) 8-layer-laminate Hashin/Progressive Failure Criterion.

Table 3.7

Comparison of failure load in the concentric fiber infill samples using different methods

Concentric	**Failure Load (N)**	**% difference**
Experimental	10654 (±697.84)	---
8 layer-laminate, Tsai-Wu	9224	14.39
8 layer-laminate, Hashin/ Progressive Failure	9364	15.88

3.2.3. Dynamic Mechanical Analysis for a Variable Temperature

The glass transition temperature is the limit temperature above which the mechanical properties, such as the stiffness of the polymer, start deteriorating and behaving like rubber. In this section, the effect of the continuous fiber layout on T_g was studied using

DMA.

The viscoelastic properties, namely storage modulus and $\tan\delta$ (damping), evolution with temperature are shown in Figure 3.16 and Figure 3.17 at temperatures from 30 °C to 160 °C under constant 1 Hz-frequency with the intent of characterizing isotropic and concentric fibers. Three samples per test were evaluated and the sample which best depicted the trend behavior is presented.

It is worth noting that the glass transition temperature, T_g, can be deduced from either the first inflection point in the graph of storage modulus vs. temperature or from the maximum peak in the tan δ vs. temperature curve (Goertzen & Kessler, 2007). In this study, T_g is estimated using the first method which is the most conservative (Goertzen & Kessler, 2007).

The glass transition temperatures estimated from Figure 3.16 for the Onyx, isotropic and concentric samples are 65 °C, 94 °C and 100 °C, respectively. Below T_g, the molecules do not have enough available energy to move. As the temperature increases, close to T_g, the elastic modulus decreases as the molecules of the polymer start moving due to increased mobility from the absorbed heat. However, the presence of short (in Onyx) and continuous fibers reduce the molecular motion (Anuar et al., 2008) requiring more energy (higher temperature) to move around those obstacles (fibers). Although the difference in the fiber volume fraction between the concentric and isotropic layout is less than 1%, the isotropic fiber layout displayed higher stiffness than the concentric layout. This is partially due to the fact that the interior of a concentric layout is filled with polymer (see Figure 3.3) making the composite more compliant in this interior region.

On the other hand, concentric fibers are expected to provide flexural strength.

Although the concentric fibers are less stiff than the isotropic fibers, they maintain their stiffness better due to polymeric middle section, i.e., their stiffness reduces in a rate slower than the isotropic counterpart does. Thus, the concentric fiber layout sample exhibits a higher T_g.

Shown in Figure 3.16, the isotropic fiber-reinforced sample at 30 °C is about 30% stiffer than the concentric fiber-reinforced material. As the temperature increases and the material passes through the glass transition to the rubbery plateau, the storage moduli drop significantly and beyond the glass transition. The curves for both isotropic and concentric fiber infill approach each other implying that as the temperature increases, the materials lost their structural integrity as they melt, and the differences in their fiber orientation did not affect their properties (storage modulus). However, the gap between storage moduli in the rubbery phase temperature range for the two composites are still higher than that for the Onyx.

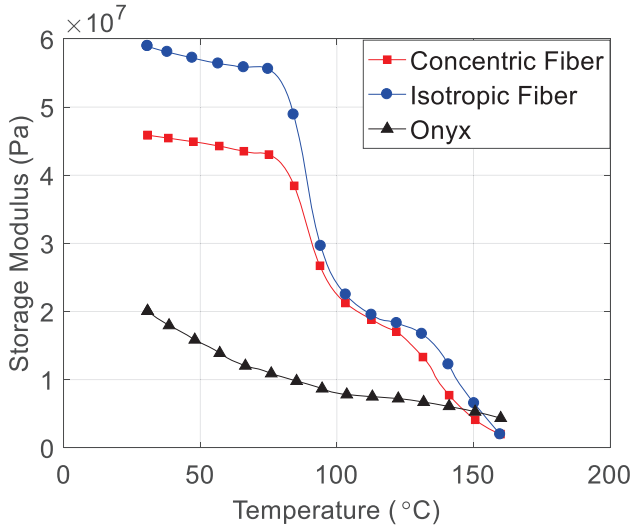

Figure 3.16 Storage modulus as a function of temperature for the three samples.

The tan δ graph in Figure 3.17 shows that Onyx possesses better damping parameter than the AM continuous fiber reinforced composites below 84 °C. The composites at lower temperatures retain high stiffness which does not promote the motion of the polymer segments around them. Once the matrix in the AM continuous fiber composites passes through the glass transition region, the composites exhibit considerably higher damping relative to the Onyx sample. The main contributors to this enhanced damping are the frictional and slippage mechanisms in the presence of the added surface area furnished by the continuous fibers. These results demonstrate that fiber-reinforced composites can achieve high damping by sacrificing their stiffness.

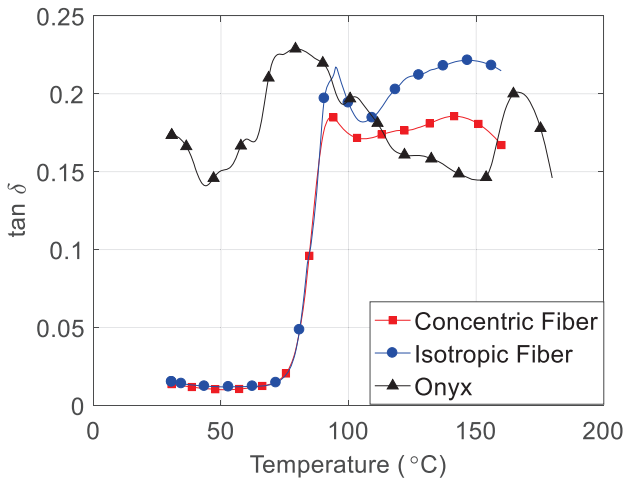

Figure 3.17 Damping parameter $(tan\,\delta)$ as a function of temperature for the three samples.

3.2.4. Dynamic Mechanical Analysis for a Variable Frequency

Next, isothermal conditions at 30 °C were considered while sweeping the frequency between 1 Hz and 100 Hz. Figure 3.18 shows the evolution of the storage modulus with frequency, while Figure 3.19 illustrates the variation of the damping parameter, tan δ,

with frequency. The storage modulus, which is indicative of the stored elastic energy, is much higher for the AM continuous fiber reinforced composites compared to the Onyx sample since the fibers provide high stiffness to the composite.

It is worth noting that unlike tan δ (and the loss modulus), the storage modulus shows little variation over the frequency range. In theory, both the loss and storage moduli exhibit frequency dependence on a higher scale in viscous fluids and viscoelastic materials than elastic ones. In the present research, as the material becomes less viscoelastic by adding continuous carbon fibers, the frequency dependence of the storage modulus vanishes. Such observation was reported for carbon fiber composites with different fibers orientation (Melo & Radford, 2005) within a range of frequencies.

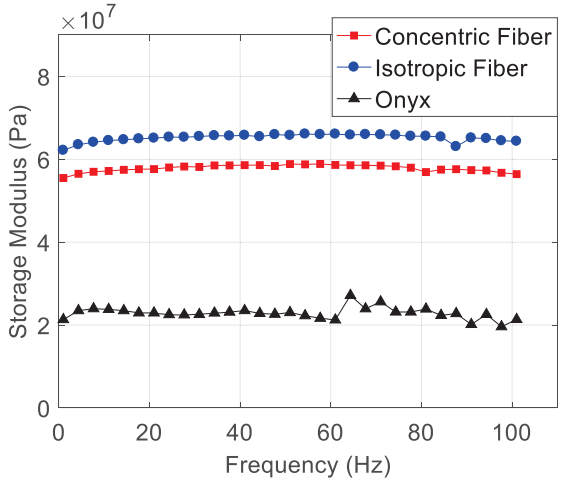

Figure 3.18 Storage modulus as a function of frequency for the three samples.

Examining Figure 3.19, the two continuous fiber layouts exhibited identical damping at 30 °C within the frequency range. Once again, Onyx has greater damping, but very low

stiffness compared to the continuous fiber-reinforced samples.

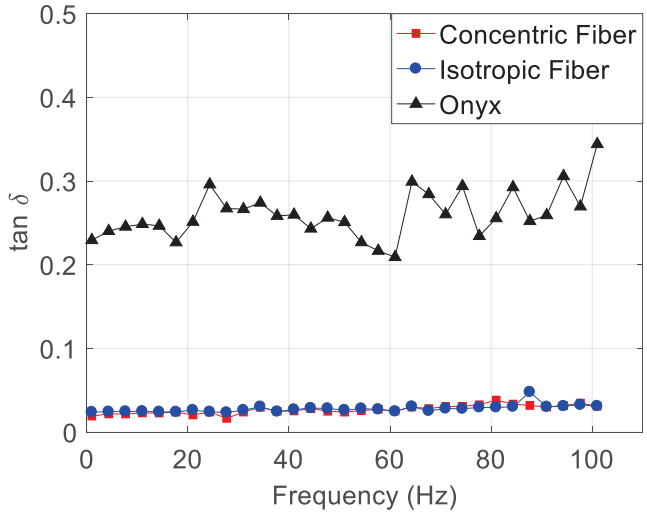

Figure 3.19 $tan\ \delta$ as a function of frequency for the three samples.

3.2.5. Dynamic Mechanical Analysis for Temperature Sweep at Different Frequencies

To obtain the activation energy of glass transition for the different composites, the temperature sweep was conducted at four different frequencies (1 Hz, 10 Hz, 30 Hz and 50 Hz). Figure 3.20 (a-c) show the storage modulus variation for Onyx, isotropic and concentric samples, respectively. The graphs for AM continuous fiber reinforced samples show that there is a slight shift of the curves as the frequency increases; which indicates that the glass transition depends on the frequency as previously reported (Chartoff, Menczel & Dillman, 2009; Goertzen & Kessler, 2007). For higher frequencies, the glassy to rubbery transition occurs at higher temperatures. The shift to higher temperatures is a direct result of time–temperature equivalence. As the frequency is increased, only shorter timescale molecular motions are permitted; thus, the polymer responds more as if it was

at a lower temperature than a sample that runs at a lower frequency but at the same temperature. Consequently, higher temperatures are needed for a sample to attain an identical mechanical state at higher frequencies, hence, the transitions shift toward higher temperatures.

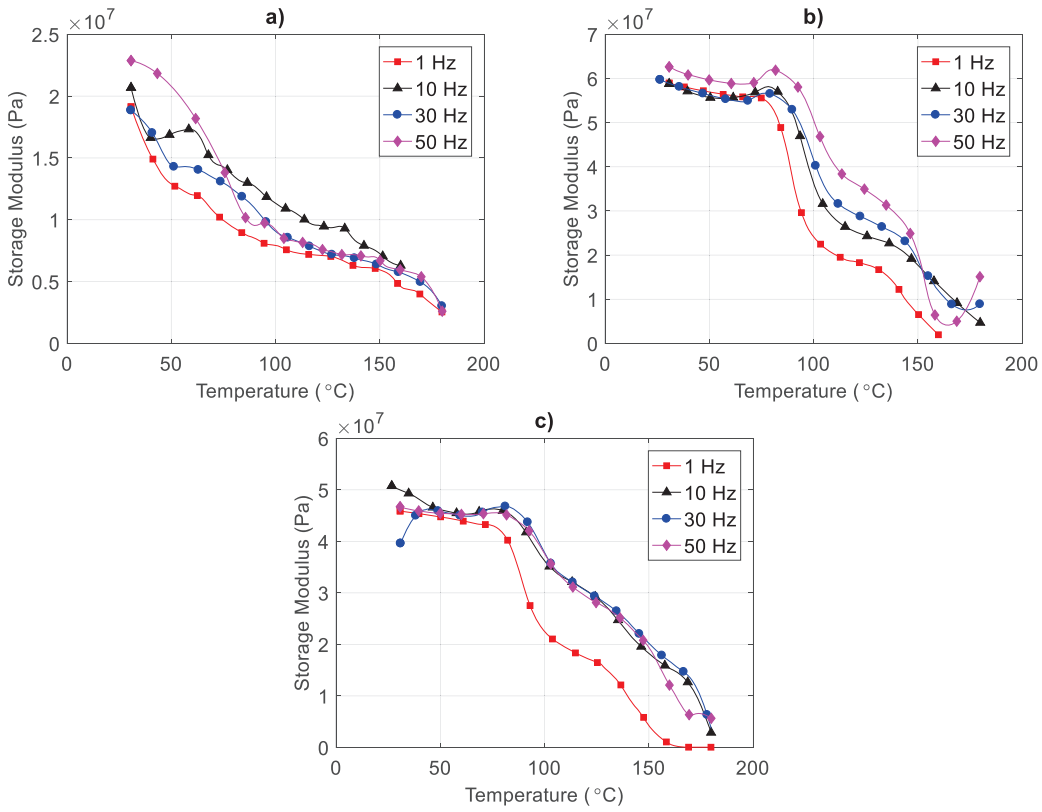

Figure 3.20 Storage modulus under temperature sweep at different frequencies for a) pure Onyx sample, b) composite with isotropic fiber configuration, and c) composite with concentric fiber configuration.

From the variation of the T_g from the storage modulus curves as a function of the frequency (Figure 3.20), transition maps can be constructed using linear regression and equation (3.3). Since the trends in the transition maps are straight-lines as shown in

Figure 3.21, the activation energy causing the viscoelastic behavior can be estimated.

Table 3.8 shows the activation energy (ΔH) of the three target samples in this study along with the R-squared value to assess the accuracy of the fitted data. The R-squared value for the Onyx specimen was low since T_g did not consistently increase with frequency. The results for the AM composites indicate that T_g increased with frequency for all samples. This can indicate that at higher frequencies the materials exhibited a γ- (i.e., glass) transition – local mode relaxation discussed in (Hatakeyama & Quinn, 1999). Since T_g and the activation energy of the concentric fiber-reinforced sample is higher than that of the isotropic sample, it is anticipated that the former creeps at a lower rate when compared to the isotropic sample. The results also indicate that the Onyx has the highest creep rate.

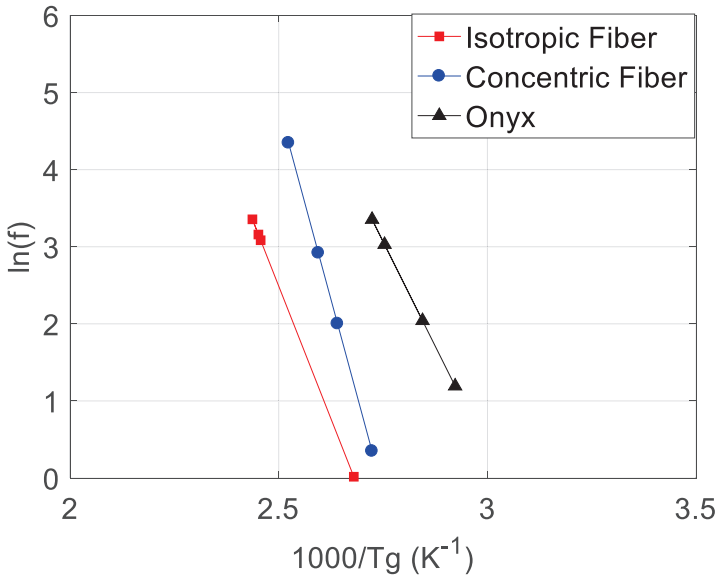

Figure 3.21 Variation of T_g with frequency for the three samples.

Table 3.8

Activation energy of glass transition for the three samples

Samples	$\frac{d(\ln(f))}{d(1/T_g)}$	R^2	ΔH (KJ/mol)
Concentric Fibers	-2.00e4	0.895	166.17
Isotropic Fibers	-1.37e4	0.765	114.27
Onyx	-1.09e4	0.021	90.3

4. Experimental Investigation of Additively Manufactured Continuous Fiber Reinforced Composite Parts with Optimized Topology and Fiber Paths

The current chapter focuses on demonstrating the fabrication feasibility of designs with optimized topology and fiber paths and validating the enhanced stiffness to weight ratio obtained using the optimization schemes. To this end, a fused filament fabrication (FFF) printer, modified by the Materials group at University of Texas at Austin, was employed to fabricate parts with customized infill patterns. In particular, this chapter presents a systematic design of three benchmark structures for maximum stiffness, including a cantilevered plate, an MBB beam, and an L-shaped bracket.

The initial design domain, loading, and boundary conditions are set up for each test case. The topology and fiber paths are designed to optimize the test case's stiffness subject to a volume fraction constraint. The optimized models are post-processed for AM and experimental testing. A code is developed to generate the AM input file (G-code) from the optimized fiber paths and topology and is provided to the 3D printer. The fabricated design was subsequently loaded under identical conditions to those used for the design optimization.

Detailed FEA is performed for the optimized designs, and the results are compared to the displacements captured via DIC. Finally, the stiffness to weight ratio of designs, both considering and not considering the AM constraints, is compared with traditionally designed composite parts consisting of unidirectional laminates. This chapter was published in (Fernandes et al., 2021) in collaboration with the University of Texas at Austin.

4.1. Materials and Methods

This subsection briefly discusses the topology and fiber placement optimization

methods and finite element modeling used for the three benchmark problems of this chapter. The manufacturing constraints are also presented.

4.1.1. Experimental

A composite 3D printer was built by the University of Texas at Austin using off-the-shelf components. Markforged functionalities were enhanced in this printer enabling the manufacture of customized fiber layouts using Markforged carbon fibers without the need for a matrix. This allowed the fabrication of the topology and orientation optimized parts which would not be otherwise possible using commercial composite 3D printers.

The optimized printed parts were experimentally tested by our collaborators using customized test fixtures and a tensile machine with a 25 kN load cell at a rate of 0.5 mm/s. DIC was again used to capture in-plane displacement. For more details on the manufacturing and testing please refer to our published article (Fernandes et al., 2021).

4.1.2. Stiffness Design Optimization

Papapetrou, Patel and Tamijani (2020) proposed several optimization schemes to maximize the stiffness of continuous fiber-reinforced parts subjected to a minimum weight constraint. They showed that no single optimization scheme achieved the highest stiffness for all the test cases. Therefore, the designs with the most enhanced stiffnesses reported by Papapetrou, Patel and Tamijani (2020) were selected.

One of the two topology optimization schemes – the SOMP and level-set methods – was applied to the three benchmark problems in the present study. The SOMP is a density-based method in which an elastic modulus proportional to a power law of the density is implemented to obtain an optimized solid-void design with filament (fiber) orientations. These filament orientations, however, produce discontinuous paths. Therefore, filament infill techniques such as the offset and the equally spaced (EQS)

methods, in the case of the present study, were introduced in the SOMP optimization to generate continuous filament paths.

The offset method yields fibers along the contours of the optimized boundary and at an equal distance from each other. A positive value is attributed to solid elements and a negative value to the voids. The method generates a line parallel to the boundaries of the structure on the solid elements. Subsequent lines are individually generated in a similar fashion at a constant distance from adjacent lines until the structure is completely filled with non-intersecting lines. The offset method is robust and can be used to design both simple and complex layouts, however, it often yields sharp edges that are not manufacturable. Eliminating sharp edges requires post-processing, as discussed later in the results section.

The EQS generates filament paths parallel to the boundary of the optimized structure and at an equal distance from each other. The EQS differs from the offset method because it places the fibers spanning along the longitudinal direction of the geometry starting from the constrained edge. In this approach, sections along the structure's transverse direction are divided by points according to the desired number of filaments. The points throughout the layout are then connected to form the fiber lines. The EQS method usually generates smoother filament paths than the offset method, but it is impracticable for complex layouts, as discussed by Papapetrou, Patel and Tamijani (2020). After implementing the offset or EQS approach, interpolation is used to obtain filament orientations in all adjacent finite elements.

As an alternative to the EQS and SOMP, the level-set topology optimization method was used for the MBB and L-shape problems. In this method, the boundaries of the

structure are represented by an implicit model and are allowed to move during optimization, according to the sensitivity of the objective function, until convergence is achieved (Wang, Wang & Guo, 2003). In the case of the level-set topology optimization, the filament path optimization using the offset method was introduced from the first iteration.

Three manufacturing constraints were considered in the post-optimization stage: 1) filament spacing is 0.9 mm; 2) minimum filament length that can be appropriately extruded without clogging is 45 mm; and 3) closed filament paths need to be modified into continuous loops of several filaments, reducing the number of filament cutting and making the printing process faster, easier, and more reliable.

In addition to these manufacturing limitations, variations between the experimental and optimized model boundary conditions (constraints and force applications) are present. The constraints and loads are applied to each part's edge in the optimization, which is not practical in experimental settings. This difference is significant for the cantilever and L-shape bracket parts, which require additional holes and fasteners to be mounted to the testing apparatus. The effect of the boundary conditions, of the experimental and optimized model, on the structure's stiffness, was studied in the Results and Discussion section.

4.1.3. Finite Element Analysis (FEA)

A framework was developed to perform the FEA of continuous fiber composites. Meshing was carried out using triangular shell elements. Modeling the continuous fiber-reinforced composite structures in a finite element software using the software’s graphical user interface is unfeasible and cumbersome since the fibers are not unidirectional, and their orientation and thus mechanical properties change from one

element to another. Therefore, the material property is attributed to each element and is dictated by the nearest filament orientation.

A MATLAB code was developed to generate the mesh and the bulk data file (.bdf) with the loads, constraints, and composite material properties. The MATLAB framework runs this file in MSC NASTRAN to obtain the displacements used in the computation of the structural stiffness.

During the optimization, point loads are applied at a single node while the structure's edge is constrained (line constraint). However, the FEA model replicates the experimental model in which holes were introduced to mount and apply the load. The FEA model is constrained around the holes' edges. The loads and constraints are equivalently applied to a patch of elements to eliminate stress concentrations and more reliably simulate the testing condition. The size of the patch depends on how the loads and constraints are experimentally applied. Material properties for composite material used in this study are summarized in Table 4.1.

Table 4.1.

Elastic material properties of carbon fiber reinforced filaments

E_1	E_2	G_{12}	ν_{12}
52.00 GPa	4.00 GPa	2.00 GPa	0.33

Note: this data was extracted from (van de Werken, Hurley, et al., 2019).

4.2. Results and Discussion

The feasibility study of the optimization methods by demonstrating the manufacturability of the parts and enhanced performance of optimized parts are now

presented. This subsection also compares the experimental and computational models and presents a study on the effects of the manufacturing constraints on the specific stiffnesses of three benchmark optimization cases: the cantilever plate, MBB beam and l-bracket.

4.2.1. Cantilever Plate Case Study

In this chapter, the terminology “cantilever plate” is used for brevity to refer to a plate clamped on one edge and free on the other three edges. The cantilever plate studied by Papapetrou, Patel and Tamijani (2020) was selected as the first case study. The plate is subjected to a 10 kN point load in the middle of its free edge, shown in Figure 4.1 (a). SOMP was used to optimize the 200 × 100 element-rectangular domain shown in Figure 4.1 (a) for an optimization filtering radius of r_{min} = 4.5 mm and volume constraint of 50% of the initial domain. As shown in Figure 4.1, two fiber layouts were considered for this problem: the EQS and the offset fiber infills.

The optimized load paths were analyzed to understand the SOMP topology presented in Figure 4.1 (b) and (c). Tamijani and his collaborators have recently developed a method to identify load paths (Tamijani et al., 2018) and later implemented the concept in topology optimization (Gharibi & Tamijani, 2021). Knowing how the load is transferred from the point of load application to the structure's constraints reveals the efficient use of material to increase the structural functionality. The optimized load paths in x (horizontal) and y (vertical) directions, ψ_x and ψ_y, for the cantilevered plate in the study (assuming isotropic properties) are represented in Figure 4.2. It is visible, comparing Figure 4.1 with Figure 4.2, that the regions that do not transfer loads, such as the far left top and bottom corners of the plate and the middle of the clamped (right) edge, are removed during optimization as they do not carry loads and only add to the structure’s

weight.

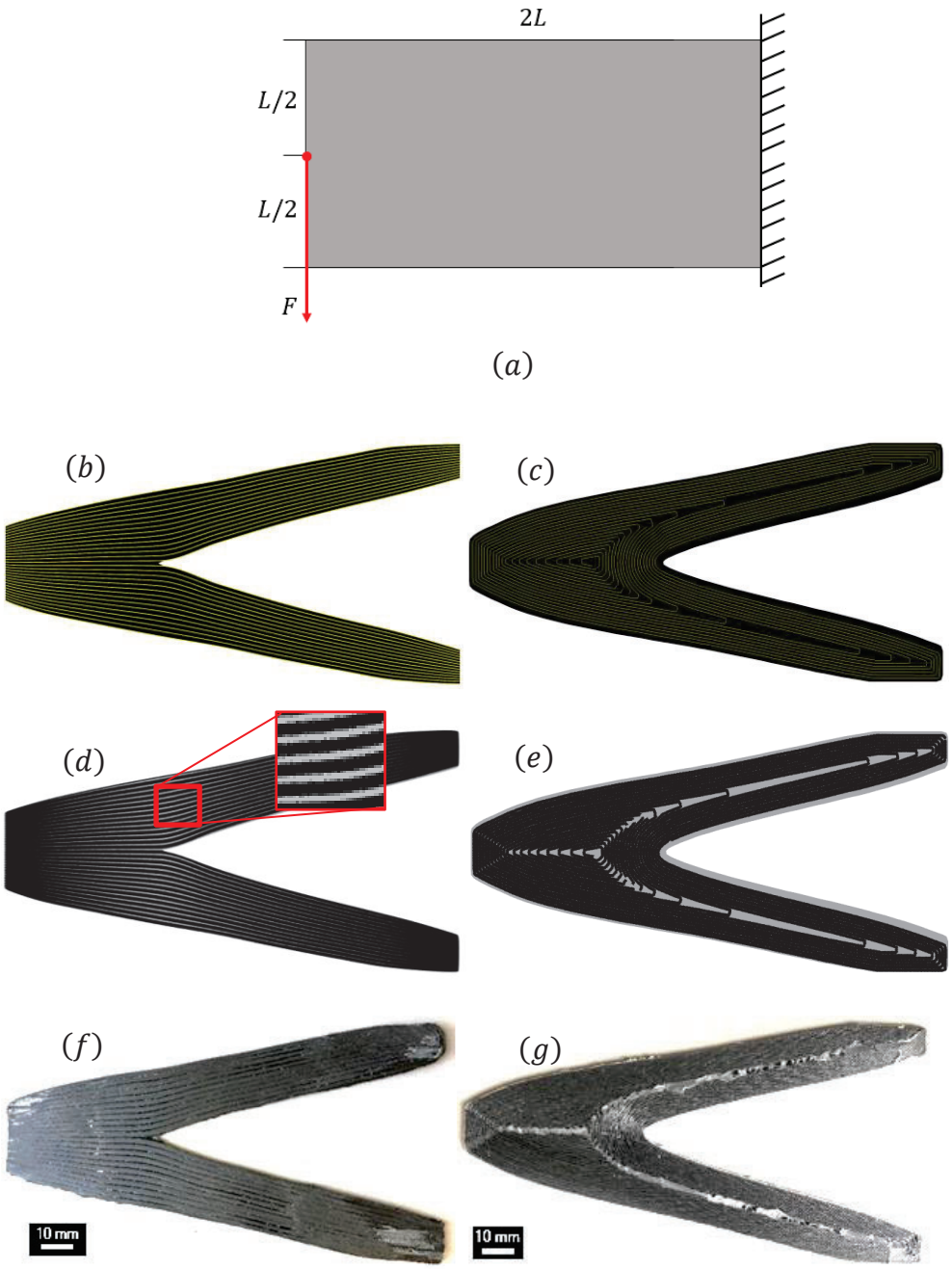

Figure 4.1 a) The original cantilever domain used for the optimization. The optimized cantilevered plate: (b) EQS and (c) offset fiber paths; (d) FEA computational model with EQS filament infill (inset shows gaps between filaments), and (e) computational model with offset filament infill; (f) Additively manufactured EQS (1 mm thick) and (g) offset designs (5 mm thick); both designs are ~150 x 75mm.

The optimization is performed assuming a 100% fiber infill density over the optimized topology. However, it is not possible to print the entire optimized area with fiber-reinforced filaments, as the printing filaments have a finite width, 0.9 mm in this study. A zero distance between adjacent filaments was not enforced in the optimization process. Therefore, laying filaments over the part resulted in gaps between adjacent rasters in some regions, as shown in Figure 4.1 (d). When possible, these gaps were filled with nylon, as shown in Figure 4.1 (g).

The two configurations, illustrated in Figure 4.1 (b) and (c), were additively manufactured, shown in Figure 4.1 (f) and (g), and experimentally tested. The computationally and experimentally vertical displacement for the optimized design with EQS and offset designs are shown in Figure 4.3. The vertical displacements agree well, although the region of low displacement (dark orange) in the computational EQS model is larger than in the experimental one ((a) and (b)). This discrepancy is due to the lack of rigidity in the fixtures that fix the plate, allowing a small rotation during the experiment.

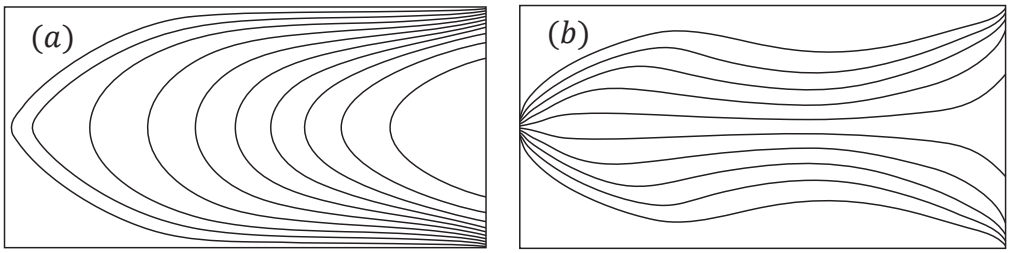

Figure 4.2. Optimized load paths (a) ψ_x and (b) ψ_y for an isotropic cantilever plate (Gharibi & Tamijani, 2021).

It is also worth noting that the gaps between the EQS rasters are visible in the FEA contours of Figure 4.3 (b) but not in the experimental DIC map, Figure 4.3 (a). This is

because the paint used to create the speckle pattern fills the inter-filament gaps and DIC does not have a high enough resolution to capture them.

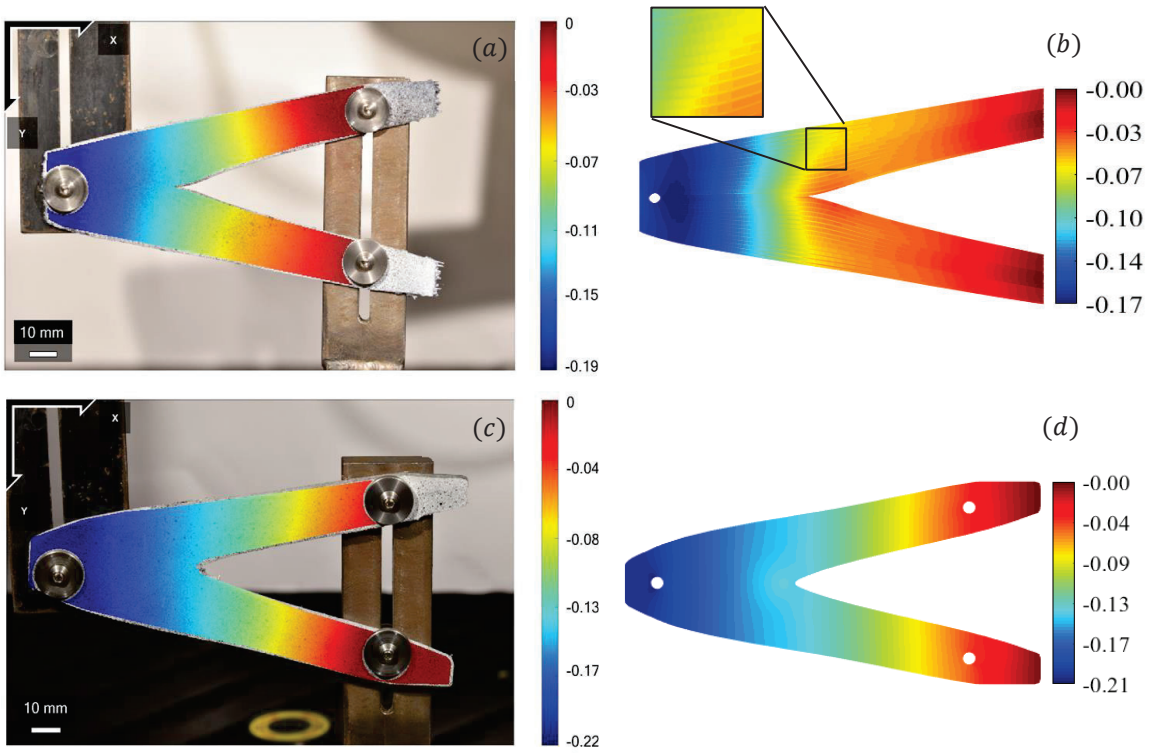

Figure 4.3. The full-field vertical displacement (mm): (a) DIC and (b) FEA results for EQS fibers at 6.14 N/g; (c) DIC and (d) FEA results for the offset fibers at 9.75 N/g.

Table 4.2 shows specific stiffness (stiffness per mass) values measured experimentally and computed via FEA. There is a relatively close agreement between the experimental and computational results for the structure's specific stiffness, with the highest percentage difference of 18% for the EQS model. This difference is attributed to the raster spacing, which is challenging to accurately represent in the FEA model.

The original optimized structures, without manufacturing constraints implemented,

are up to 2.8 times as stiff as the non-optimized one (a rectangular plate with all fibers in the horizontal direction). Since filaments are designed to carry loads in the longitudinal direction, along with their highest stiffness, the EQS designed part is expected to be stiffer than the offset one. The orientation of the EQS filaments at the fixed connection allows the fibers to transfer the load from the point of its application to the constraints more efficiently than the fibers in the offset design, which are perpendicular to the fixed connection. However, the gaps between the EQS filaments in the printed model weaken the structure, resulting in a stiffness lower than the offset sample and as good as the non-optimized model.

Table 4.2.

Specific stiffness ($Nmm^{-1}g^{-1}$) for the three cantilever plates in the study. "Previous design" refers to the design in the preceding row for that fiber path. "Exp." and "Comp." stand for experimental and computational, respectively.

Model	**Exp. Specific Stiffness**	**Comp. Specific Stiffness**	**% Improvement**
Non-optimized design w/o holes	----	35.60	----
EQS design:100% infill	----	99.50	179
Offset design:100% infill	----	59.00	66
EQS previous design + filaments 0.9 mm apart	----	43.10	21
Offset previous design + filaments 0.9 mm apart	----	36.20	3
EQS previous design + drilled holes	29.40	35.30	-1
Offset previous design + drilled holes	38.30	44.50	25

Since both the topology and filament layouts are simple, the optimized models satisfied the manufacturing constraints, and no post-processing was required for their manufacturing. The only adjustments needed were three 4.5 mm holes drilled into each of the parts (Figure 4.3), two of which were used to constrain the structure by screwing it to a testing fixture, and the other hole was used for load application. The effects of the drilled holes are captured in Table 4.2. For the EQS filament infill, the application of loads and constraints via these holes decreased the stiffness by 18%. The offset model, however, exhibited an increase in the stiffness with the introduction of drilled holes as the fibers near the right edge are running vertically, thus not bearing the load.

4.2.2. MBB Beam Case Study

The second benchmark design, the Messerschmitt-Bolkow-Blohm (MBB) beam, was performed by the level-set optimization of the 400 × 100 element-rectangular domain shown in Figure 4.4 (a); under a 1 kN point load and rollers' supports. The optimized topology is obtained after 151 iterations, and its volume is 43% of the initial volume (see Figure 4.4 (b)). A minimum thickness of 4.5 mm is considered in the optimization process. Level-set/offset yields an MBB beam with higher stiffness than other methods, such as the EQS, since the level-set/offset fills out 100% of the optimized part with filaments placed around the inner and outer edges, reinforcing the boundaries (Papapetrou, Patel & Tamijani, 2020).

A 100% infill is only possible if the filament width was infinitesimally small. In reality, the filament width is 0.9 mm, leaving some portions of the topology unfilled. Although the filament midlines are 0.9 mm away from each other, the optimized infill in Figure 4.4 (b) is not yet printable.

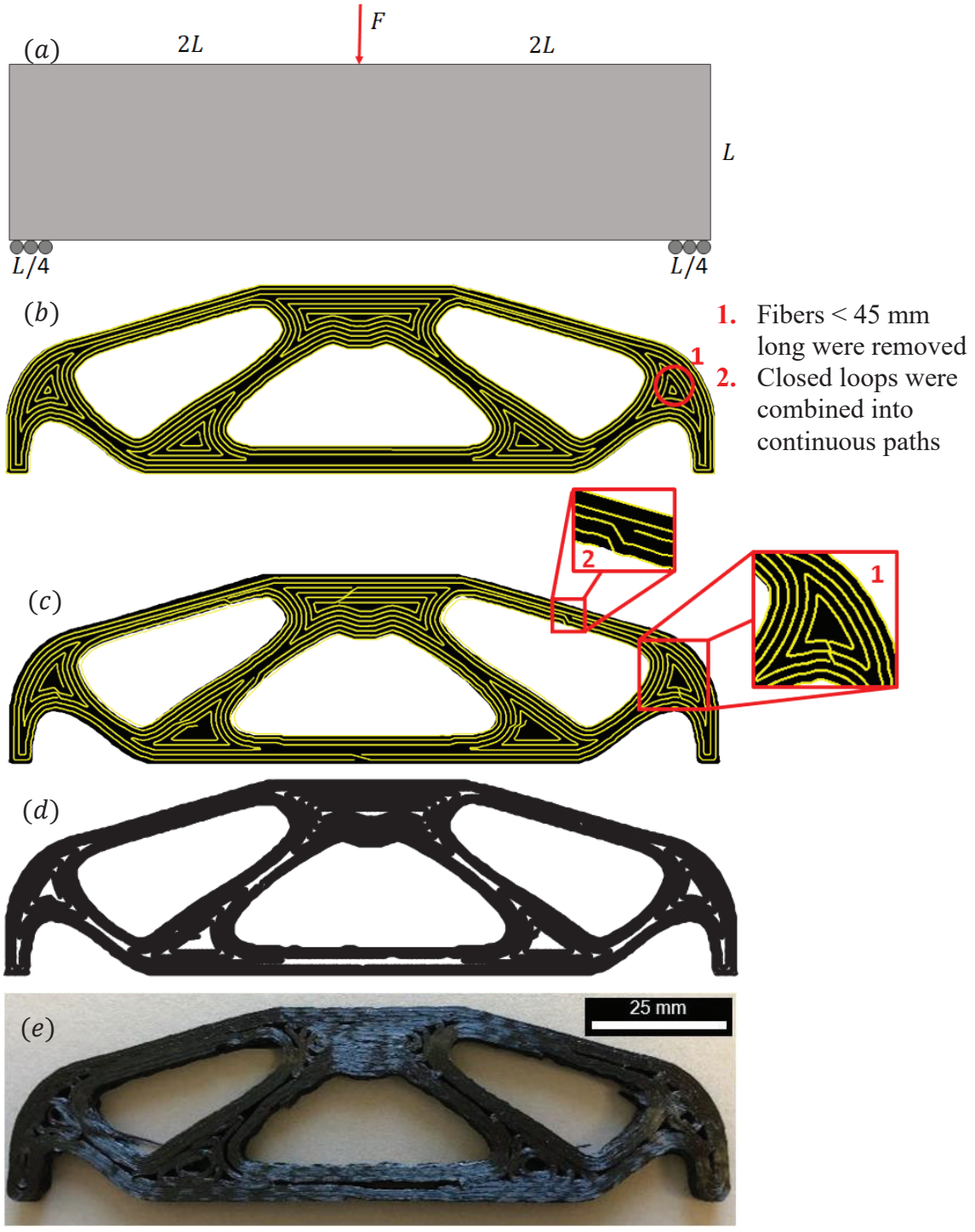

Figure 4.4. a) Original optimization domain for the bridge case for L = 37 mm. Optimized MBB model: (b) without and (c) with manufacturing constraints. MBB (d) FEA model and (e) AM part: 141 mm long, 37 mm tall, and 5 mm thick.

Short filament paths (less than 45 mm long) were removed to make this design printable.As shown Figure 4.4 (b) and (c), filament paths are designed as closed loops. Closed loops cannot be practically printed. To address this issue and reduce the number of filament cuttings, the closed filament loops were grouped with their adjacent ones, and each group was turned into a single continuous path, as shown in Figure 4.4 (c) (the printable model).

The optimized MBB structure was experimentally tested in a 3-point bending setup. The experimental DIC and FEA vertical displacements for this design are compared in Figure 4.5 and Table 4.3, showing a good correlation. There is a 6% difference between the specific stiffnesses measured via the DIC and FEA, stemming from the discrepancies between the designed model and the printed part. It is visible from Figure 4.4 (d) and (e) that the sharp corners in the computational model are printed slightly rounded as the printer's nozzle is unable to handle abrupt changes in the filament path. There is a relatively large displacement observed on the bottom middle section of the part in the experimental DIC contour but not in the computational one. The large displacement may be due to the horizontal gap between the printed filaments.

The following remarks can be pointed out from the analysis of AM constraints in Table 4.3: 1) the stiffness of the original optimized model without manufacturing constraints is 2.17 times the stiffness of the non-optimized unidirectional model with fibers oriented at 0º. Introducing the fiber width constraint (i.e., 0.9 mm) reduces the stiffness by 8%. 2) removing the short filaments, Figure 4.4(b) and (c), slightly affects the part response since the removed filaments were far from the load and constrained boundaries and would only take a minute portion of the loads. 3) Similarly, grouping the

fibers, Figure 4.4 (b) and (c), does not affect the elastic response of the part.

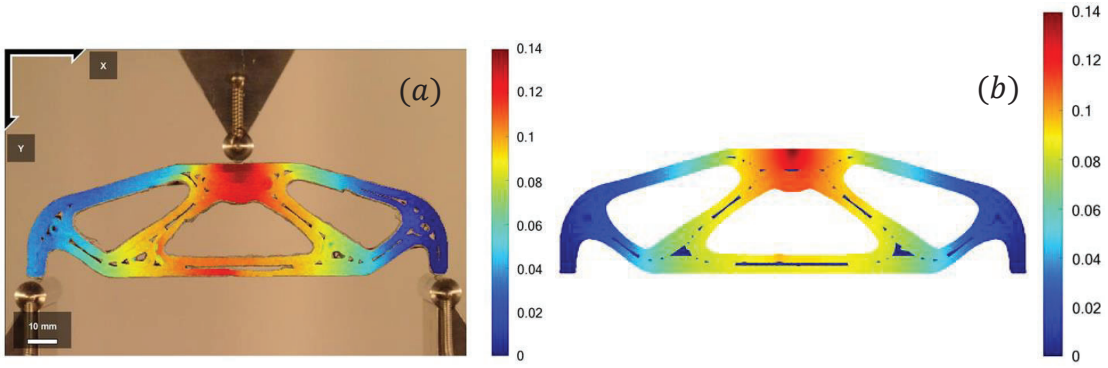

Figure 4.5. Vertical displacement (mm) from DIC (a) and FEA (b) at the 37.4 N/g force per mass.

Table 4.3

Specific stiffness ($Nmm^{-1}g^{-1}$) for the MBB beam in the study. "Previous design" corresponds to the design of the preceding row.

Model	**Experimental Specific Stiffness**	**Computational Specific Stiffness**	**% Improvement**
Reference design with 0º fibers	----	130.00	---
Optimized: 100% infill	----	282.00	117.00
Previous design + filaments 0.9 mm apart	----	261.00	100.00
Previous design + no short filaments	----	262.03	102.00
Previous design + all other AM constraints	245.60	261.00	101.00

4.2.3. L-Bracket Case Study

The L-bracket was selected as the last case study. The level-set optimization of the domain in Figure 4.6 (a) for 30,000 elements, 11 kN vertical load, and volume constraint

of 37% of the initial domain resulted in the design shown in Figure 4.6 (b), after 251 iterations. Level-set/offset method was selected for the L-bracket benchmark study since they result in one of the stiffest layouts for this problem; compared to SOMP combined with EQS and other methods discussed by (Papapetrou, Patel & Tamijani, 2020). In addition to the filament width constraint (0.9 mm), which is applied in the offset approach, three more constraints for testing and printing the bracket part were post-applied. First, holes need to be drilled adjacent to the boundaries for fixing the bracket and applying the vertical load to it; Figure 4.6 (c). Second, short filament paths were eliminated and closed filament loops were grouped Figure 4.6 (b) and (c).

The L-bracket, Figure 4.6 (c), was printed, Figure 4.6 (e), and tested in a specially designed fixture. Similar to the MBB case, the printer rounds the sharp edges defined in the model and present in the FEA model (Figure 4.6 (d)). The results for both the computational and experimental analyses are compared in Figure 4.7 and Table 4.4, respectively. Figure 4.7 shows identical vertical displacement contours for the FEA and experimental cases. Similarly Table 4.4 shows a good agreement with only a 6% difference between the specific stiffnesses measured via DIC and FEA, presumably caused by the gaps between the printed filaments.Table 4.4 evaluates the effects of the manufacturing constraints on the stiffness of the part by considering five models: I) the original optimized model constrained at the top edges of the L-bracket and the load applied to a patch of elements on the right edge of the part; II) the optimized model considering the fiber width constraint; III) model (II) with drilled holes simulating the fasteners used in the experiment to constrain and apply load to the part; IV) model (III) in which short fibers are removed; and V) model (IV) with filament rings grouped in spirals.

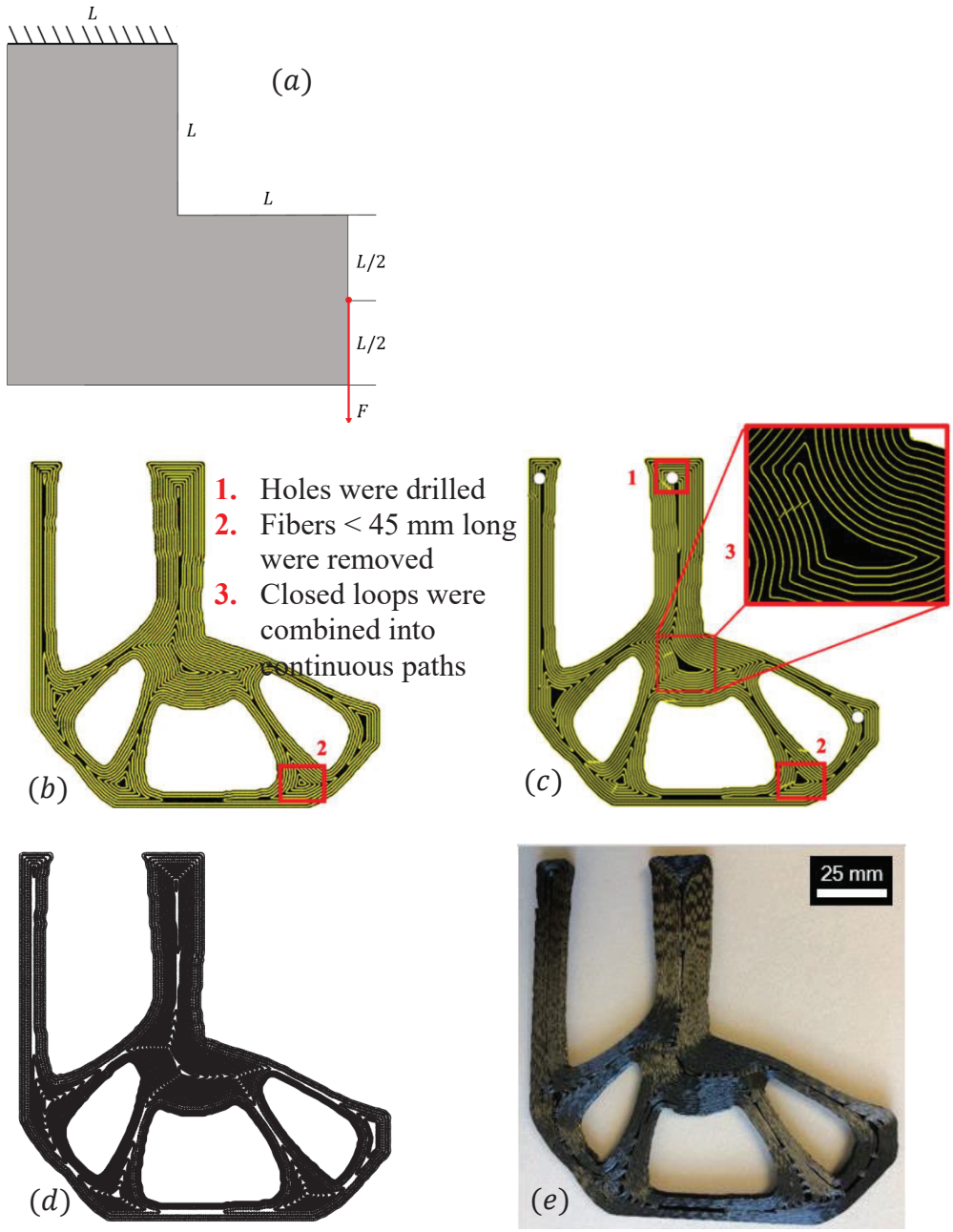

Figure 4.6 a) Original optimization domain for the L-bracket. L-bracket optimized using level-set with offset filaments: (b) without and (c) with manufacturing constraints. L-bracket (d) computational model and (e) AM part; the final part is 130 × 130 × 5.1 mm.

In addition, two non-optimized parts with fibers oriented in a symmetric $[\pm 45]_s$ and $[0/90]_s$ stacking sequence were considered. The $[0/90]_s$ laminate exhibited a higher

stiffness than the $[\pm 45]_s$ because some laminae are oriented parallel to the constraints and perpendicular to the applied force, providing better resistance to deformation. Therefore, the $[0°/90°]_s$ laminate was taken as the reference design relative to which the stiffness improvements and weight reductions of the optimized designs were calculated.

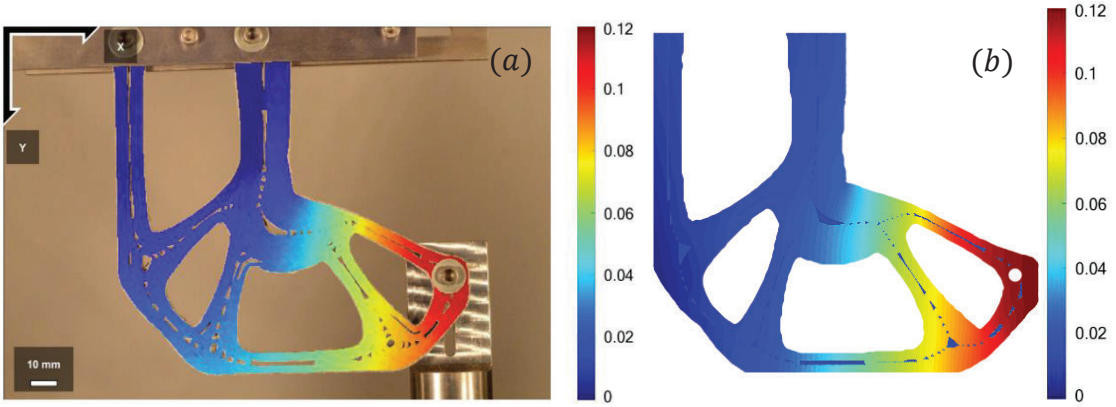

Figure 4.7. Vertical displacement (mm) of the loaded L-bracket obtained from the DIC (a) and FEA (b) at 4.14 N/g of force per mass.

The following additional observations can be made from Table 4.4: 1) The specific stiffness of the optimized geometry with 100% fiber infill (before applying any manufacturing constraints) is two times the reference $[0/90]_s$ configuration. The filament width constraint introduces gaps between the rasters, reducing the specific stiffness; the stiffness of the optimized design is 1.8 times that of the reference geometry. 2) Similar to the offset cantilever model, the drilled holes increased the structure's specific stiffness as the loads and constraints were applied at the drilled holes instead of the edges. The drilled holes constrain the vertical fibers at the top of the L-bracket, providing a stiffer built-in connection and smaller overall deflections. 3) Removing the short fibers had little effect on the stiffness as they only carry a tiny fraction of the loads. Similar to the MBB case,

removing the short filaments in the L-bracket design caused a minor change in both the deflection and overall weight, resulting in a slight reduction of the specific stiffness. 4) Grouping the close filaments into spirals marginally reduced the stiffness due to the discontinuities created from the shift at the end of a fiber to the adjacent one. Thus, the model with all the manufacturing constraints exhibited a 90% increase in stiffness than the $[0/90]_s$ model.

Table 4.4

Specific stiffness **($Nmm^{-1}g^{-1}$)** for the L-bracket part. "Previous design" corresponds to the design of the preceding row.

Model	**Experimental Specific Stiffness**	**Computational Specific Stiffness**	**% Improvement**
Reference $[0^o/90^o]_s$	----	19.70	---
Reference $[\pm 45^o]_s$	----	9.50	-52
Optimized: 100% infill	----	40.90	107
Previous design + filaments 0.9 mm apart	----	35.40	79
Previous design + with drilled holes	----	39.70	101
Previous design + no short filaments	----	38.50	95
Previous design + all other AM constraints	35.10	37.40	90

4.2.4. Summary

Table 4.5 summarizes the experimental and computational results for all the studied cases. The simulated optimized specific stiffness was compared against the simulated non-optimized specific stiffness for the three cases. In general, the computational specific

stiffnesses are in a relatively close agreement with the experimental specific stiffnesses.

The most considerable difference between experimental and computational values was observed for the cantilever plate with EQS infill with a difference of 18%. This difference could be due to the flawed interfaces between the printed filaments, resulting in the incomplete load transfer between fibers, which also explain the unexpected no-improvement in the specific stiffness of the EQS model relative to the non-optimized model.

Table 4.5

Experimental and computational specific stiffnesses ($Nmm^{-1}g^{-1}$) of the tested benchmark specimens

Description	**Exper. Specific Stiffness**	**Comp. Specific Stiffness**	**% Difference**	**% Specific Stiffness Improvement**	**% Weight Reduction**
Offset cantilever	38	45	15	25	20
EQS cantilever	29	35	18	0	0
MBB beam	246	261	6	102	50
L-bracket	35	37	6	90	47

The other optimized designs exhibited an enhanced specific stiffness and significant weight reduction compared with their non-optimized counterparts, with a stiffness improvement of up to two times in the MBB beam case. The percent weight reduction is calculated based on structures with identical stiffnesses but different weights. For

example, suppose an optimized design has a specific stiffness that is twice that of a traditional design (100% enhancement). In that case, the traditional design's mass should be twice the optimized one to achieve the same absolute stiffness. The optimized design, therefore, realizes a 50% weight reduction.

AM composites offer several design freedoms that can be exploited to fabricate parts with unprecedented mechanical performances. The ability to manufacture a part without special tooling and with optimized topology and fiber path opens up new avenues to fabricate AM end-use parts, which require high strength or stiffness. As a result, AM composites can replace metals and plastics for low-volume production markets and applications, especially when high specific strength and stiffness are critical or short production times are required. AM composites are, however, expensive compared with high-volume manufacturing methods for plastics and metals. This is not true for conventional composites where their manufacturing cost does not typically decrease with their production volume. AM composites can therefore, replace traditional composite parts.

5. Design Optimization of Lattice Structures with Stress Constraints

The goal of this chapter is to investigate the optimization of the topologies and morphologies of lattice structures that are subject to stress constraints. Square cells with rectangular holes with two characterizing parameters related to the void are used as the base cells. The effective unit cell stiffness and yield stress are obtained using numerical homogenization and compared to those found experimentally. Effective properties are obtained for various cell parameters in order to construct response surfaces. The response surfaces are implemented using a homogenization-based optimization algorithm. The modified Hill's criterion is implemented to establish the stress constraints and a material indicator variable is used to address the stress singularity issue. The stress constraints are represented using a p-mean function and a clustering approach is utilized to preserve some of the local nature of the stress. The optimized homogenized designs are then projected onto a fine mesh to generate the lattice structure. Finally, the projected lattice designs are post-processed to remove thin and floating members and enforce a minimum manufacturable feature size.

The framework is tested for two cases: an L-shaped bracket and a single-edge notched bend (SENB) problem. Comparison of the compliance-based and stress-constrained designs for these cases clearly demonstrates that the optimized material distribution is different when the stresses are considered as constraints. In addition, the projected SENB design is additively manufactured and experimentally evaluated. The optimized design is shown to be manufacturable and to exhibit yield strength similar to those implemented via stress constraints. The four major contributions of this study are: (1) comparison of the effective stiffnesses and yield stresses obtained using numerical homogenization and experimental evaluation; (2) implementation of stress constraints

and related sensitivity analyses in homogenization-based optimization of lattice structures; (3) incorporation of unit cell orthotropic properties in the optimization process to further improve the stiffness; and (4) demonstrating the fabrication feasibility of the lattice design and experimentally validating the optimized yield strength.

5.1. Effective Cell Properties

Square cells with rectangular holes are considered in the current study. As shown in Figure 5.1, the cell is parameterized using two parameters (h_1 and h_2). The member thicknesses can be found using the corresponding parameter $t_n = 1 - h_n$ (n is the parameter number) and the corresponding cell volume fraction is $1 - h_1 h_2$.

The homogenized stiffness tensor ($\bar{\boldsymbol{C}}$) is found via numerical homogenization (Andreassen & Andreasen, 2014; Guedes & Kikuchi, 1990; Hassani & Hinton, 1998) over a representative volume element (RVE):

$$\int_Y C_{ijpq}\left(\frac{\partial \chi_p^{kl}}{dy_q} - \varepsilon_{pq}^{(0)kl}\right)\frac{\partial v_i}{\partial y_j}\, dY = 0$$

$$\bar{C}_{ijkl}(\boldsymbol{r}) = \frac{1}{|Y|}\int_Y C_{mspq}(\boldsymbol{r},\boldsymbol{y})\left(\varepsilon_{pq}^{(0)kl} - \varepsilon_{pq}(\chi^{kl})\right)\left(\varepsilon_{ms}^{(0)ij} - \varepsilon_{ms}(\chi^{ij})\right) dY \tag{5.1}$$

where Y is the cell domain, $\boldsymbol{\varepsilon}^{(0)kl}$ are the three macroscopic unit strains, $\boldsymbol{\chi}^{kl}$ are the displacement fields**,** v_i is the virtual displacement field, and $\boldsymbol{C}$ is the stiffness tensor of the cell material. Using $\varepsilon_{pq}(\chi^{kl})$ allows the relation between the local micro-stress ($\boldsymbol{\sigma}$) and effective macro-stress ($\bar{\boldsymbol{\sigma}} = \bar{\boldsymbol{C}}\,\bar{\boldsymbol{\varepsilon}}$; $\bar{\boldsymbol{\varepsilon}}$ is the effective strain) to be established (Hollister & Kikuchi, 1992):

$$\boldsymbol{\sigma} = \boldsymbol{C}\,\boldsymbol{M}\,\bar{\boldsymbol{S}}\,\bar{\boldsymbol{\sigma}};\; M_{ijkl} = \frac{1}{2}\left(\delta_{ik}\delta_{jl} + \delta_{il}\delta_{jk}\right) - \varepsilon_{ij}(\chi^{kl}) \tag{5.2}$$

where δ_{ij} is the Kronecker delta and $\bar{\boldsymbol{S}}$ is the inverse of the homogenized stiffness

tensor. Since it is assumed that the cell is composed of an isotropic material, the von Mises yield criterion is chosen to describe the strength at the microstructure level. The von Mises yield criterion is expressed as:

$$SR^{rs}\left(\left(\frac{\sigma_{22}^{rs}}{\sigma^{Y}}\right)^{2}+\left(\frac{\sigma_{11}^{rs}}{\sigma^{Y}}\right)^{2}-\frac{\sigma_{11}^{kl}\sigma_{22}^{rs}}{{\sigma^{Y}}^{2}}+\left(\frac{\sqrt{3}\sigma_{12}^{rs}}{\sigma^{Y}}\right)^{2}\right)-1=0 \tag{5.3}$$

where SR^{rs} in equation (5.3) represents the strength ratios and σ^{Y} is the material yield strength. Four macroscopic unit stresses ($\boldsymbol{\sigma}^{(0)rs}$; $rs = 11,22,12,44$), including uniaxial in each direction, pure shear and hydrostatic, are applied in order to obtain SR^{rs}. Then, the macroscopic effective yield stresses ($\overline{\boldsymbol{\sigma}}^{\mathrm{Y}}$) are obtained based on the strength ratios:

$$\overline{\sigma}_{\mathrm{rs}}^{\mathrm{Y}} = SR^{rs} \tag{5.4}$$

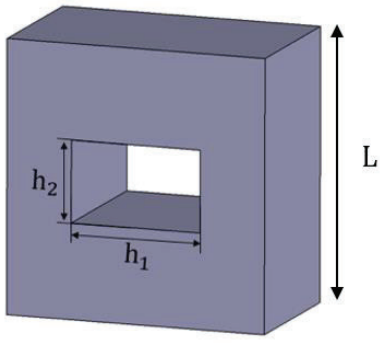

Figure 5.1. Parameterization of a square cell with a rectangular hole.

In order to validate the properties obtained using the homogenization method and evaluate the effect of the characterizing parameters on the effective tensile yield strength, 14 x 4 cell lattice structures were manufactured using an HP 3D High Reusability PA 12 Multi Jet Fusion (MJF) printer (HP Jet Fusion 5200 Series). Through the MJF, fusing and

detailing agents were deposited along with heat onto thin layers of powder. This process was repeated until all layers were formed. The material properties were determined by testing five specimens according to ASTM D638-14. The Young's modulus of the material was $E = 1288.30 \pm 45$ MPa; the yield strength was $\sigma^Y = 18.3 \pm 0.9$ MPa, and the Poisson's ratio was $\nu = 0.375 \pm 0.1$.

The lattice specimens were subjected to tensile loads using an MTS Criterion Model 43 test machine with a 50 kN load cell at a constant crosshead displacement rate of 0.875 mm/min. The test was terminated when the samples fractured fully. The strains were measured using DIC. The samples were 20 mm wide, 70 mm long and 3 mm thick for 5 mm long square cells. In the first set of experiments, $h_2 = 0.5L$ was kept constant and five different h_1 values ($h_1 = 0.1L, 0.3L, 0.5L, 0.7L$ and $0.9L$) were considered. L is the cell size. In the other set of experiments, h_1 was kept constant at $0.5L$ and four different h_2 values ($h_2 = 0.1L, 0.3L, 0.7L$ and $0.9L$) were considered.

The results presented are the average of five samples that were 3D printed for each configuration. Figure 5.2 (a) shows the printed model for a cellular solid with $h_1 = 0.7L$ and $h_2 = 0.5L$. The strain distribution for the middle of the sample was obtained via DIC and a single cell was extracted, Figure 5.2 (b) and (c).

The results are compared to the distribution obtained via homogenization theory ($\varepsilon = M\bar{S}\,\bar{\sigma}$) in Figure 5.2 (d). The numerical homogenization contour shows that high strains appear around the hole with the highest strains near the four corners of the hole. In contrast, the experimental contour shows a high but more distributed strain on the side of the hole with the highest strain at the corner of the hole and expanding to the corner of the cell. Quantitatively, the experimental and numerical homogenization strains are

within similar ranges. Figure 5.2 (e)-(h) compares the experimental and computational strain contours for ($h_1 = 0.5L$ and $h_2 = 0.5L$) and ($h_1 = 0.5L$ and $h_2 = 0.3L$), for which observations similar to those from ($h_1 = 0.7L$ and $h_2 = 0.5L$) can be drawn.

Stress-strain curves are plotted for various h_1 values in Figure 5.3 (a). All of the samples deform linearly before yielding. This is followed by nonlinear deformation and fracture. It is also observed that the strength and elastic modulus decrease as h_1 increases. A larger h_1 implies that a smaller area carries the load; this results in higher stresses. The stress-strain curves produced when h_2 varies (Figure 5.3 (b)) exhibit trends similar to those noted when h_1 is allowed to vary, although the change in the yield strength is not as significant. The experimental and computational yield strength and elastic modulus of each sample are compiled in Table 5.1 and Table 5.2. The experimental yield stresses are determined from the 0.2% offset lines of the stress-strain curves (Figure 5.3).

The difference between the numerical homogenization and experimental results is less than 16%. This validates the results obtained using the homogenization method. The largest difference of 15% is observed for $h_1 = 0.9L$ (Table 5.1). This can be attributed to geometric differences between the CAD model and the actual printed model. More specifically, the printer resolution forces the holes to be printed with some curvature instead of being completely rectangular. Rounded holes have lower stress concentrations. To compensate for this, a filtering technique based on the weighted average distance function is applied to the homogenization results to remove concentrated stress from the corners of the holes. After experimental validation of the effective properties, properties were determined for various cell parameters and used to construct the response surfaces, $\bar{C}\ (h_n)$ and $\overline{\sigma}^{Y}(h_n)$, as shown in Figure 5.4.

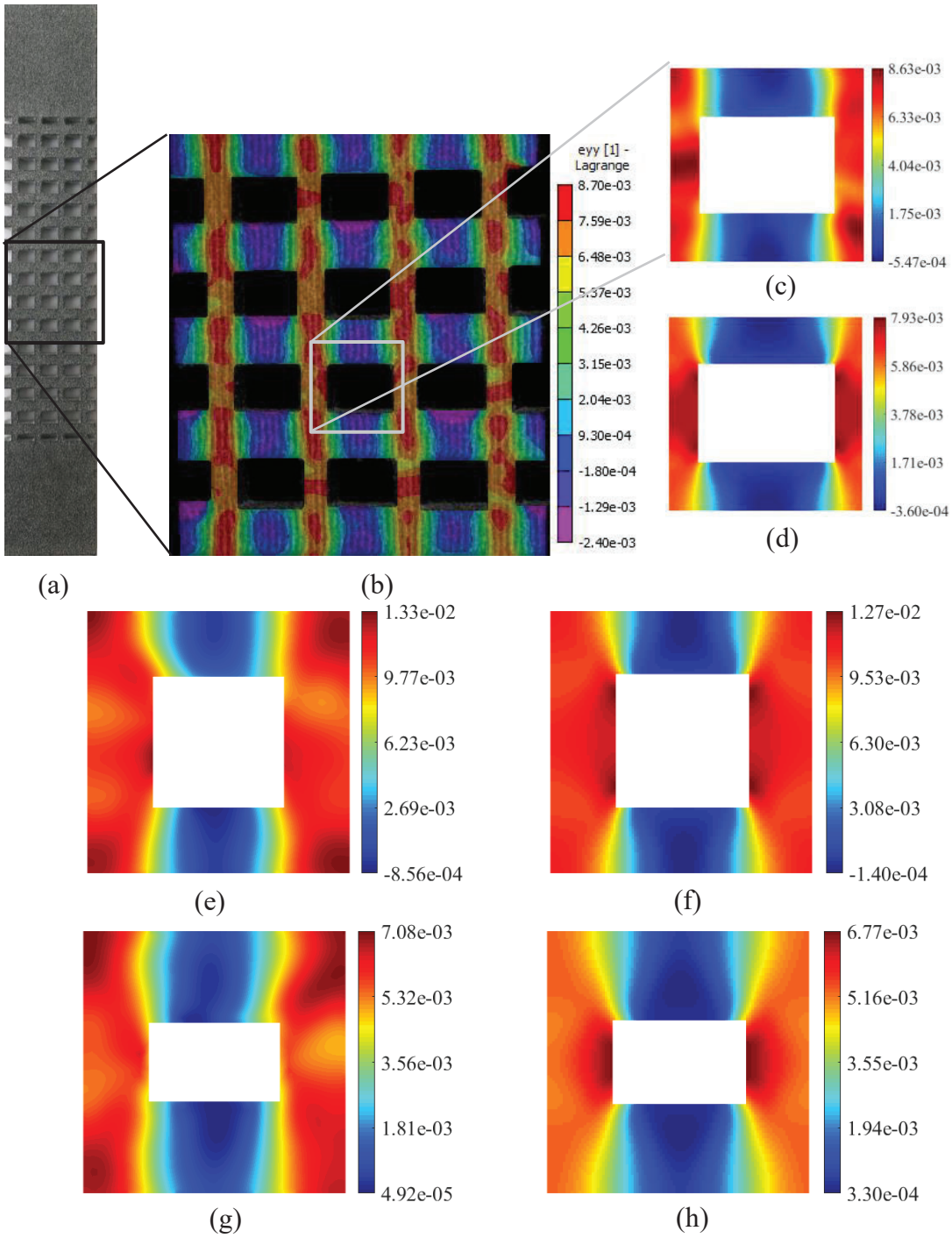

Figure 5.2. Lattice structure strain contours: (a) printed specimen, (b) DIC strain contour, (c) DIC image of one cell and (d) numerical homogenization strain contour for $h_1 = 0.7L$ at 182.6 N; (e) DIC and (f) numerical homogenization strain contours of one cell with $h_1 = 0.5L$ at 444 N; (g) DIC and (h) numerical homogenization strain contours of one cell with $h_2 = 0.3L$ at 240 N.

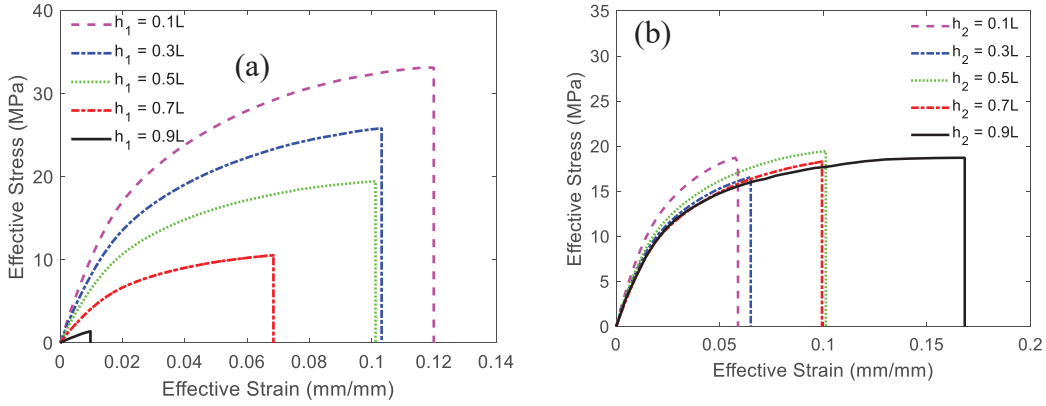

Figure 5.3. Stress vs. strain curves: (a) variation with h_1 and (b) variation with h_2.

The homogenized stiffness matrix $\overline{\boldsymbol{C}}$ is derived with respect to the principal axes of anisotropy. When the cell is rotated by angle θ, the stiffness matrix is updated using the transformation matrix (R):

$$\overline{\boldsymbol{C}}_{\theta}(\theta, h_1, h_2) = \boldsymbol{R}\,(\theta)\overline{\boldsymbol{C}}\,(h_1, h_2)\boldsymbol{R}^{T}\,(\theta) \tag{5.5}$$

Table 5.1

Variation in effective properties with h_1

h_1	0.1 L	0.3 L	0.5 L	0.7 L	0.9 L
Young's modulus variation (MPa)					
Experimental	1105 ±106.59	881 ±30.85	728 ±29.51	453 ±11.09	178 ±6.27
Numerical	1188	945	702	448	172
% Difference	7.24	6.97	3.63	1.00	3.70
Yield strength variation (MPa)					
Experimental	14.93 ±2.80	12.17 ±1.18	9.3 ±0.66	5.77 ±0.81	1.55 ±0.37
Numerical	14.5	11.05	8.27	5.33	1.8
% Difference	2.94	9.62	11.72	7.87	15.14

It should be noted that the stress and strain tensors are expressed as vectors using Voigt notation. Due to the orthotropic behavior of the square cell with a rectangular hole, Hill's yield criterion is chosen to describe the lattice strength. It is assumed in Hill's yield criterion that the hydrostatic pressure does not affect the yield strength. However, this assumption is not accurate for lattice cells. Thus, a modified Hill's criterion (Deshpande, Fleck & Ashby, 2001) is utilized that includes the hydrostatic yield strength. The effective yield stresses ($\bar{\boldsymbol{\sigma}}^{\mathrm{Y}}$) are used in the macroscopic modified Hill's yield criterion for each element:

$$F_e - 1 = 0;\ F_e = \sqrt{\bar{\boldsymbol{\sigma}}^{\boldsymbol{T}}\,\mathbb{V}\bar{\boldsymbol{\sigma}}}$$

$$\mathbb{V}_{11} = \left(\frac{1}{\bar{\sigma}^{\mathrm{Y}}_{11}}\right)^2 + \frac{1}{9}\left(\frac{1}{\bar{\sigma}^{\mathrm{Y}}_{44}}\right)^2, \qquad \mathbb{V}_{22} = \left(\frac{1}{\bar{\sigma}^{\mathrm{Y}}_{22}}\right)^2 + \frac{1}{9}\left(\frac{1}{\bar{\sigma}^{\mathrm{Y}}_{44}}\right)^2 \tag{5.6}$$

$$\mathbb{V}_{12} = -\frac{1}{2}\left(\left(\frac{1}{\bar{\sigma}^{\mathrm{Y}}_{11}}\right)^2 + \left(\frac{1}{\bar{\sigma}^{\mathrm{Y}}_{22}}\right)^2 - \left(\frac{1}{\bar{\sigma}^{\mathrm{Y}}_{33}}\right)^2 - \frac{2}{9}\left(\frac{1}{\bar{\sigma}^{\mathrm{Y}}_{44}}\right)^2\right),$$

$$\mathbb{V}_{33} = \frac{1}{2}\left(\frac{1}{\bar{\sigma}^{\mathrm{Y}}_{12}}\right)^2$$

where $\bar{\sigma}^{\mathrm{Y}}_{11}$, $\bar{\sigma}^{\mathrm{Y}}_{22}$, and $\bar{\sigma}^{\mathrm{Y}}_{12}$ are the effective uniaxial and shear yield strengths, $\bar{\sigma}^{\mathrm{Y}}_{44}$ is the hydrostatic yield strength, and $\bar{\sigma}^{\mathrm{Y}}_{33}$ is obtained from $\min(\bar{\sigma}^{\mathrm{Y}}_{11}, \bar{\sigma}^{\mathrm{Y}}_{22})$. The yield criterion in equation (5.6) is developed in the principle axes of anisotropy. The stresses and strains in the reference axes ($\bar{\boldsymbol{\sigma}}_\theta$ and $\bar{\boldsymbol{\varepsilon}}_\theta$) are obtained using the transformation matrix (R).

Table 5.2

Variation in effective properties with h_2

h_2	0.1 L	0.3 L	0.5 L	0.7 L	0.9 L
Young's modulus variation (MPa)					
Experimental	886 ± 33.16	700 ± 37.34	728 ± 29.51	642 ± 45.47	632 ± 51.25
Numerical	840	757	702	668	652
% Difference	5.34	7.79	3.63	4.00	3.16
Yield strength variation (MPa)					
Experimental	11 ± 0.4	8.97 ±0.15	9.30 ±0.66	8.33 ±0.29	8.43 ±0.38
Numerical	9.71	8.35	8.27	8.15	8.1
% Difference	12.46	7.12	11.72	2.22	4.03

5.2. Material Models and Stress Constraints

As mentioned earlier, one issue related to stress constraints in topology optimization is that of stress singularities at low densities. This issue was first observed during a three-bar truss optimization (Sved & Ginos, 1968). It was shown that removing members is necessary to obtain a global minimum. However, the stress in a member increases as the member's thickness approaches zero. This prevents removal of the member. Several approaches to addressing this issue are discussed in the introduction section. The stress interpolation scheme (Le et al., 2010) is adopted in this work. In order to establish the stress interpolation scheme, a material indicator variable (ϕ) is implemented. The material indicator has previously been used to obtain stiffness-optimized, coated structures with orthotropic infill (Groen, Wu & Sigmund, 2019). In our work, the material indicator is used mainly to address the singularity issue during stress-constrained optimization. The stiffness matrix ($\overline{\boldsymbol{C}}_{\theta}$), density ($\rho$), and failure index ($F_e^r$) are updated using the material indicator variable:

$$\overline{\boldsymbol{C}}_{\theta}(\theta, h_1, h_2, \phi) = \phi^{q_1}\boldsymbol{R}\,(\theta)\overline{\boldsymbol{C}}\,(h_1, h_2)\boldsymbol{R}^{T}\,(\theta)$$

$$\rho = \phi\,(1 - h_1 h_2) \tag{5.7}$$

$$F_e^r = \phi^{q_2}\sqrt{\overline{\boldsymbol{\sigma}}^{\boldsymbol{T}}\,\mathbb{V}\overline{\boldsymbol{\sigma}}}$$

where q_1 and q_2 are parameters that penalize the intermediate density. Based on previous research (Groen, Wu & Sigmund, 2019; Le et al., 2010), $q_1 = 3.0$ and $q_2 = 0.5$ are used in this work. The second challenge in stress-constrained topology optimization is related to the large number of stress constraints. To address this issue, the element failure index can be aggregated to a single constraint using the p-mean function. In order to preserve some of the local nature of the stress while avoiding excessive computational cost, a clustering approach is utilized (Alacoque, Watkins & Tamijani, 2021; Le et al., 2010). In the clustering approach, elements in the design domain are sorted based on their failure indexes. Then, the sorted elements are placed in N groups. The failure indexes of the elements in each group are aggregated into a single value using a p-mean function:

$$F_m^P = \left(\left(\frac{1}{\Omega_m}\right)\int_{\Omega_m}(F_e^r)^p\,d\Omega\right)^{\frac{1}{p}} \tag{5.8}$$

where m is the group number, Ω_m is the total volume of the elements in each group, and p is a tuning coefficient. Since the p-mean function in equation. (5.8) converges to a lower value of $\max(F_e)$, a scaling factor (s) is implemented during each iteration to decrease the difference between the p-mean function and the $\max(F_e)$ (Le et al., 2010):

$$g_m = s_m^k F_m^P - 1;\;\; s_{\mathrm{m}}^k = \alpha^k \frac{\max(F_e^r)^{k-1}}{(F_{\mathrm{m}}^P)^{k-1}} + (1 - \alpha^k)s_m^{k-1} \tag{5.9}$$

where g_m is the stress constraint for each group. The parameter α^k is selected based on the s_m^k in two consecutive iterations; $\alpha^k = 0.5$ if s is oscillating, otherwise $\alpha^k = 1.0$.

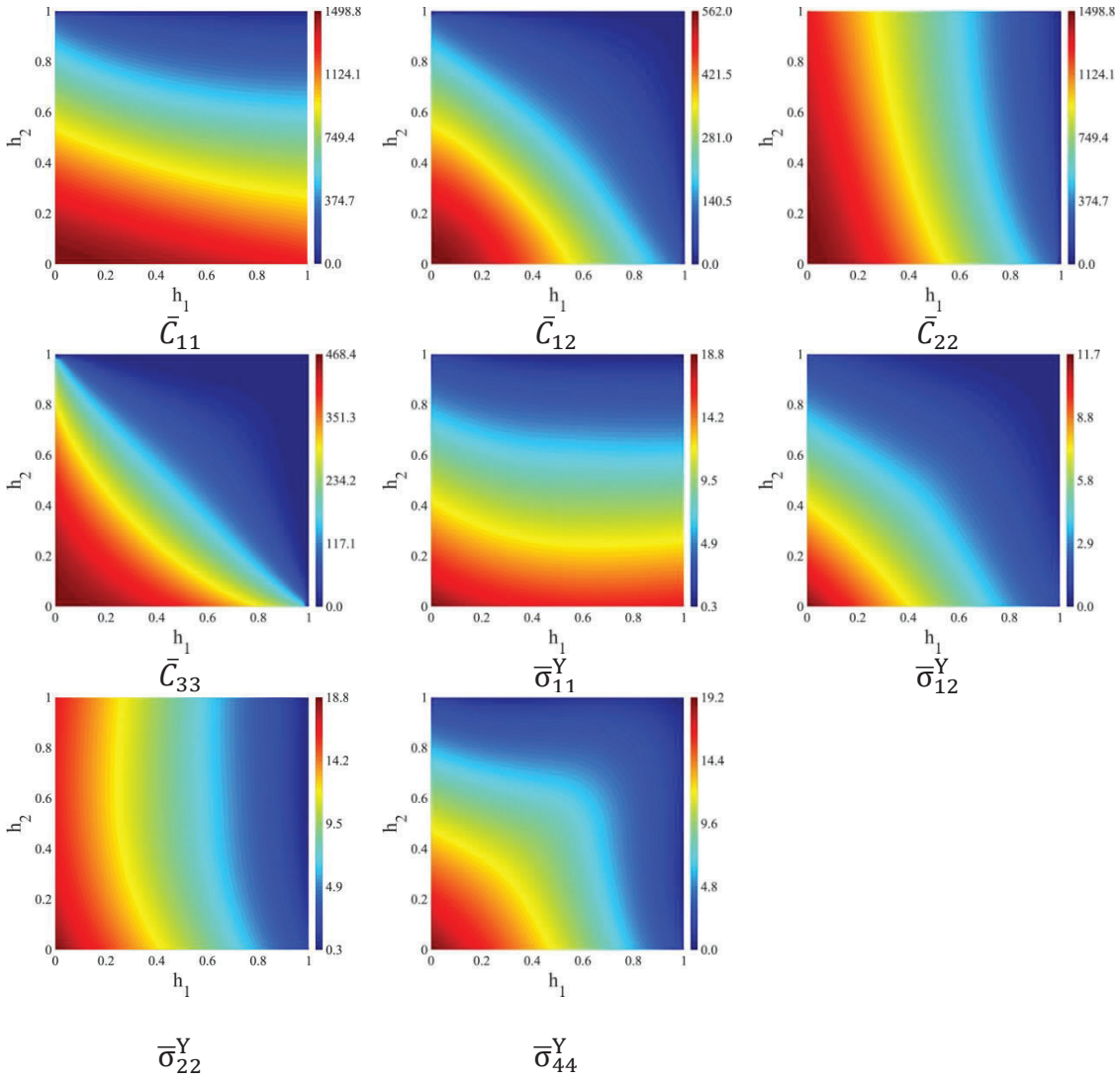

Figure 5.4. Response surfaces for the homogenized stiffness (MPa) and yield strength (MPa).

5.3. Topology and Morphology Design Optimization Algorithms

In each optimization iteration, the topology and morphology optimizations are performed in two steps. The characteristic parameters and material indicator variable are optimized in the first step and the optimized cell orientation is obtained in the second step. Two topology optimization problems are considered in this research: (1) minimizing the compliance (maximizing stiffness) subjected to the equilibrium equation and volume

constraint (V_g), and (2) minimizing the volume subjected to the equilibrium equation and stress constraints. For the compliance optimization problem, we start with initial variables (h_1^k, h_2^k, ϕ^k, and θ^k for $k = 0$) and perform the following steps during each optimization iteration:

(a) Find $\overline{\boldsymbol{C}}$ (h_1^k, h_2^k).

(b) Solve the elasticity problem, $\boldsymbol{KU} = \boldsymbol{F}$, where $\boldsymbol{K}$, $\boldsymbol{U}$, and $\boldsymbol{F}$ are the stiffness matrix, the displacement vector, and the force vector, respectively.

(c) Filter the design variables h_1^k, h_2^k, and ϕ^k

(d) Obtain the sensitivity of the objective function and constraint with respect to the design variables h_1^k, h_2^k, ϕ^k, and θ^k.

(e) Perform topology optimization (5.10) and update $\boldsymbol{h}_{\mathrm{n}}^{\mathrm{k+1}}$ and $\boldsymbol{\phi}^{k+1}$.

(f) Perform morphology optimization (5.11) and update $\boldsymbol{\theta}^{k+1}$.

(g) The process continues (k=$k+1$) until convergence.

$$\begin{gathered} \min SE \\ \text{subjected to } (\frac{1}{\mathrm{V}_0}) \int_{\Omega} \rho d\Omega - V_g \leq 0 \\ \text{design variables } \ 0 < \boldsymbol{h}_{\mathrm{n}} \text{ and } \boldsymbol{\phi} \leq 1. \ \ n = 1, 2 \end{gathered} \tag{5.10}$$

$$\begin{gathered} \min SE/SE_0 + P_\theta/2P_{\theta 0} \\ \text{design variables } \ -2\pi \leq \boldsymbol{\theta} \leq 2\pi \end{gathered} \tag{5.11}$$

where SE is compliance $\left(SE = \bar{\boldsymbol{\varepsilon}}^T \overline{\boldsymbol{C}} \bar{\boldsymbol{\varepsilon}}\right)$, and SE_0 is the compliance in the first iteration. V_0 is the volume of the design domain, and V_g is the volume fraction constraint. P_θ is a control function that penalizes sudden changes in orientation among neighboring elements and $P_{\theta 0}$ is the penalty function in the first iteration (Stutz et al., 2020):

$$P_\theta = \sum_{e=1}^{ne} \sum_{i=1}^{f} \left(\frac{1}{2} - \frac{1}{2} \cos\left(4\theta_e - 4\theta_i\right) \right) \tag{5.12}$$

where f is the number of elements connected to the element e. The topology optimization problem presented in (5.10) is solved using the method of moving asymptotes (Svanberg, 1987). The morphology optimization problem (5.11) is solved using the Broyden–Fletcher–Goldfarb–Shanno (BFGS) algorithm from the open-source library NLopt (Johnson). The stress-constrained optimization steps are similar to those from compliance optimization, but incorporate the following changes: $\mathbb{V}\left(h_1^k, h_2^k\right)$ is also calculated in step (a) and topology optimization with stress constraints (5.13) is performed in step (e).

$$\begin{gathered} \min V_f = \left(\frac{1}{\mathrm{V}_0}\right) \int_\Omega \rho d\Omega \\ \text{subjected to } F_m^p - 1 \leq 0 \\ \text{design variables} \quad 0 < \boldsymbol{h}_\mathrm{n} \text{ and } \boldsymbol{\phi} \leq 1. \;\; n = 1, 2 \end{gathered} \tag{5.13}$$

The sensitivity analyses for the compliance objective function, stress constraints, and volume fraction constraint are required in the optimization process. The sensitivity of the volume fraction is:

$$\begin{gathered} \frac{d}{dh_{1e}} \int_\Omega v d\Omega = -\phi \; h_{2e} \Omega_\mathrm{e} \\ \frac{d}{dh_{2e}} \int_\Omega v d\Omega = -\phi \; h_{1e} \Omega_\mathrm{e}, \;\; \frac{d}{d\phi_e} \int_\Omega v d\Omega = (1 - h_{1e} h_{2e}) \Omega_\mathrm{e} \end{gathered} \tag{5.14}$$

where Ω_e is the area of each element. The sensitivities of the compliance and p-mean stress measure are obtained using the adjoint method. The compliance objective function is self-adjoint and its sensitivity is:

$$\frac{dSE}{dh_{ne}} = -\phi^{q_1}\bar{\boldsymbol{\varepsilon}}^{\,T}\frac{d\overline{\boldsymbol{C}}}{dh_{ne}}\bar{\boldsymbol{\varepsilon}}\,\Omega_{\mathrm{e}};$$

$$\frac{dSE}{d\phi_e} = -q_1\phi^{(q_1-1)}\bar{\boldsymbol{\varepsilon}}^{\,T}\overline{\boldsymbol{C}}\bar{\boldsymbol{\varepsilon}}\,\Omega_{\mathrm{e}}; \tag{5.15}$$

$$\frac{dSE}{d\theta_e} = -2\phi^{q_1}\bar{\boldsymbol{\varepsilon}}^{T}\overline{\boldsymbol{C}}\frac{d\boldsymbol{R}^{\boldsymbol{T}}}{d\theta_i}\bar{\boldsymbol{\varepsilon}}_{\boldsymbol{\theta}}\Omega_{\mathrm{e}}$$

The sensitivity analysis of the p-mean stress measure is obtained using equation (5.8):

$$\begin{aligned}\frac{dF_m^P}{dh_{ne}} = \Bigg(&-\phi^{q_1}\boldsymbol{\varepsilon}(\boldsymbol{\lambda_m^T})\boldsymbol{R}\frac{d\overline{\boldsymbol{C}}}{dh_{ne}}\bar{\boldsymbol{\varepsilon}} \\ &+\frac{(F_m^P)^{1-p}}{2\Omega_e}(F_e^r)^{p-1}\left(\frac{\phi^{q_2}}{F_e}\right)\Bigg(2\bar{\boldsymbol{\sigma}}^{\boldsymbol{T}}\,\mathbb{V}\frac{d\overline{\boldsymbol{C}}}{dh_{ne}}\bar{\boldsymbol{\varepsilon}} \\ &+\bar{\boldsymbol{\sigma}}^{\boldsymbol{T}}\frac{d\mathbb{V}}{dh_{ne}}\bar{\boldsymbol{\sigma}}\Bigg)\Bigg)\Omega_{\mathrm{e}}\end{aligned} \tag{5.16}$$

$$\frac{dF_m^P}{d\phi_e} = \left(-q_1\phi^{q_1-1}\boldsymbol{\varepsilon}(\boldsymbol{\lambda_m^T})\boldsymbol{R}\overline{\boldsymbol{C}}\bar{\boldsymbol{\varepsilon}} + \frac{(F_m^P)^{1-p}}{2\Omega_e}(F_e^r)^{p-1}q_2\phi^{q_2-1}F_e\right)\Omega_{\mathrm{e}}$$

where the adjoint variables are:

$$\boldsymbol{\lambda_m^T K} = \boldsymbol{F_m^a}$$

$$\boldsymbol{F_m^a} = \sum_{e\in\Omega_{\mathrm{m}}}\int_{\Omega_e}\frac{(F_m^P)^{1-p}}{\Omega_{\mathrm{m}}}(F_e^r)^{p-1}\left(\frac{\phi^{q_2}}{F_e}\right)(\bar{\boldsymbol{\sigma}}^{\boldsymbol{T}}\,\mathbb{V}\overline{\boldsymbol{C}}\boldsymbol{R}^{\boldsymbol{T}}\boldsymbol{B})d\Omega_{\mathrm{e}} \tag{5.17}$$

The topology and morphology optimization framework are developed using the open-source PDE solver FreeFem++ (Hecht & Pironneau, 2013). P_1-functions are utilized to discretize the displacements and adjoint variables and P_0-functions are implemented to discretize all other variables, such as stress, strain, characteristic parameters, the material indicator variable, and orientation. In order to regularize the characteristic parameters and material indicator variable, the Helmholtz-type filtering approach is adopted in this research (Lazarov & Sigmund, 2011):

$$-\left(\frac{r_f}{2\sqrt{3}}\right)^2 \nabla^2 \tilde{h}_{\mathrm{n}} + \tilde{h}_{\mathrm{n}} = h_n \text{ on } \Omega$$
$$\frac{\partial \tilde{h}_{\mathrm{n}}}{\partial \Gamma} = \mathbf{0} \quad on\ \partial\Gamma \tag{5.18}$$

where r_f is the filter radius, Ω is the design domain, $\partial\Gamma$ is the boundary of the design domain, and $\tilde{h}_{\mathrm{n}}$ is the intermediate filtered variable. P_1-functions are used to discretize $\tilde{h}_{\mathrm{n}}$, which is then transformed into a P_0-function to obtain the filtered characteristic parameters. The same procedure is applied to obtain the filtered material indicator variable ($\tilde{\phi}$). In addition, a smoothed Heaviside projection (Wang, Lazarov & Sigmund, 2011) is applied to the material indicator variable to produce the 0/1 design variable:

$$\bar{\phi} = \frac{\tanh(\beta\eta) + \tanh\left(\beta\left(\tilde{\phi} - \eta\right)\right)}{\tanh(\beta\eta) + \tanh\left(\beta\left(1 - \eta\right)\right)} \tag{5.19}$$

where β is the projection parameter used to control the intensity of the projection. The parameter η specifies the inflection point and is set to $\eta = 0.5$. It was previously shown that the use of homogeneous Neumann boundary conditions in the filtering formulation may cause several issues in the optimized design, such as forcing structural members to be perpendicular to the boundary (Clausen & Andreassen, 2017). A boundary padding approach is suggested to address this issue (Clausen & Andreassen, 2017; Lazarov, Wang & Sigmund, 2016). In the padding technique, the boundary of the design domain is extended by a width equal to the filter radius, except at the support and load. This approach is adopted in the current research to address the boundary effects of Helmholtz-type filtering.

The material properties, state variables, and objective and constraint functions are obtained using the projected material indicator variable $\bar{\phi}$ and filtered characteristic

parameters $\tilde{h}_{\mathrm{n}}$. In order to retrieve the sensitivities of the objective and constraint functions (f) with respect to the design variables ϕ and h_n, the following chain rules are implemented (Lazarov & Sigmund, 2011; Wang, Lazarov & Sigmund, 2011):

$$\frac{\partial f(\widetilde{\boldsymbol{h}}_{\mathrm{n}})}{\partial \boldsymbol{h}_n} = \frac{\partial f}{\partial \widetilde{\boldsymbol{h}}_{\mathrm{n}}} \frac{\partial \widetilde{\boldsymbol{h}}_{\mathrm{n}}}{\partial \boldsymbol{h}_n}$$
$$\frac{\partial f(\bar{\boldsymbol{\phi}})}{\partial \boldsymbol{\phi}} = \frac{\partial f}{\partial \bar{\boldsymbol{\phi}}} \frac{\partial \bar{\boldsymbol{\phi}}}{\partial \widetilde{\boldsymbol{\phi}}} \frac{\partial \widetilde{\boldsymbol{\phi}}}{\partial \boldsymbol{\phi}} \tag{5.20}$$

Compliance-based and stress-constrained topology and morphology optimization are applied to an L-bracket problem. The dimensions and boundary conditions for the L-shaped bracket problem, including the clamped top edge and distributed load applied to the right corner ($F = 1000\ N/cm$) are shown in Figure 5.5. The load is distributed over $0.1\ cm$ and a region with an area of $0.2 \times 0.2\ cm^2$ near the applied load is excluded from the design domain.

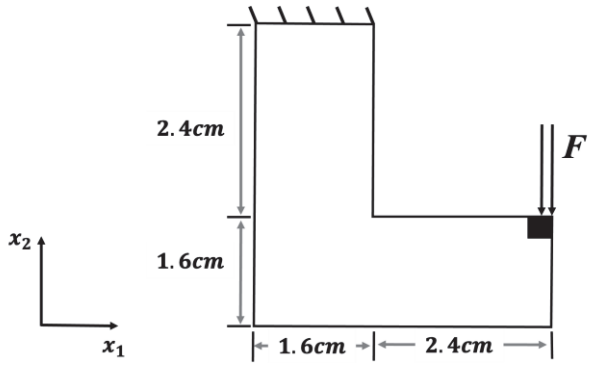

Figure 5.5. Dimensions and boundary conditions for the L-shaped bracket test case.

The domain is discretized using 23,544 triangular elements. The filter radius is $0.2\ cm$ and the maximum value of the projection parameter is $\beta = r_f/\sqrt{3}l_e$ (da Silva et

al., 2021), where l_e is the minimum elemental edge length (l_e=0.03) in this study.

As suggested in (da Silva et al., 2021), β is updated every 100 iterations until it reaches the maximum value. The response surfaces (Figure 5.4) are used to obtain homogenized properties $\overline{\boldsymbol{C}}$ and $\overline{\boldsymbol{\sigma}}^{\mathrm{Y}}$ during optimization. First, the stress-constrained optimization is performed. Ten regional stress constraints ($m = 10$) and a p-mean parameter of $p = 10$ are selected. The optimized volume fraction, compliance, and maximum of the failure index are reported in Table 5.3. The optimized material distribution ($\rho = \bar{\phi}(1 - \tilde{h}_1\tilde{h}_2)$), orientation, and failure index are shown in Figure 5.6 (a), (b), and (c), respectively. As shown in the figure, the material at the re-entrant corner is removed during the topology optimization process, the failure index is uniformly distributed, and the stress constraint is satisfied.

Table 5.3

L-bracket optimized design volume fractions, compliances, and maximum of failure index

Optimization Problem	V_g	SE (Ncm)	max(F_e^r)
Stress-constrained optimization	33.6%	28	1.0
Compliance-based optimization	33.6%	20	3.1

Next, the compliance-based optimization problem with volume fraction constraints is considered. The upper bound of the volume fraction is taken as the optimized volume fraction of the stress-constrained optimized design ($V_g = 33.6\%$). Upon comparing the material distributions and failure indexes of the two optimization problems in Figure 5.6,

it is evident that the stress constraint is not satisfied in the compliance-based design because of the stress concentration at the right-angle corner of the design. The results presented in Table 3.3 shows that lower compliance is obtained by using compliance optimization for the same volume fraction.

5.4. Projection and Post-Treatment of Lattice Structures

The homogenized design presented in Figure 5.6 is obtained based on the assumption of an infinitesimal length scale. The projection of the homogenized design to a finite length scale is discussed in this section. As shown in (Rumpf & Pazos, 2012; Tamijani, Velasco & Alacoque, 2020), a cellular solid can be represented by Fourier series expansions. For the square cell with a rectangular hole considered in this research, implementing two cosine terms is sufficient to represent the lattice structure (Pantz & Trabelsi, 2008):

$$\begin{aligned} \Omega_M = \{(x_1, x_2) \in D \mid \cos\left(\frac{2\pi\psi_1(x_1, x_2)}{\Lambda}\right) \\ > cos(\pi\phi(1-h_1)) \ \cup \ \cos\left(\frac{2\pi\psi_2(x_1, x_2)}{\Lambda}\right) \\ > cos(\pi\phi(1-h_2))\} \end{aligned} \tag{5.21}$$

where Λ is the periodicity parameter and ψ_n is the mapping function used to project the homogenized design. The mapping functions are obtained using the optimized orientation ($\boldsymbol{v} = [cos(\theta), sin(\theta)]$) (Allaire, Geoffroy-Donders & Pantz, 2019):

$$\nabla \psi_1 = \mathrm{e}^{\gamma} \boldsymbol{v} \tag{5.22}$$

where γ is a dilatation factor used to adjust the lattice spacing (Allaire, Geoffroy-Donders & Pantz, 2019):

$$\nabla\gamma = (-\nabla \times \boldsymbol{v})\overline{\boldsymbol{v}} + (\nabla \times \overline{\boldsymbol{v}})\boldsymbol{v} \tag{5.23}$$

and $\overline{\boldsymbol{v}}$ is a vector that is perpendicular to $\boldsymbol{v}$. The mapping function ψ_2 can also be obtained by using equation (5.22) and changing $\boldsymbol{v}$ to $\overline{\boldsymbol{v}}$. However, the mapping functions fail to produce the projected lattices due to irregularities in the optimized orientation (see Figure 5.6 (b) and (e)). In order to create a locally continuous vector field, we adapted the vector field combing suggested in (Groen et al., 2020). In this procedure, we start with an element in the lower left corner, the element is added to the visited element vector (i), the adjacent element (e) with minimum x_2 (see Figure 5.6*)* is selected, and the following function is calculated for four possible frame orientations (j), including $(0, \pi, \pi/2, -\pi/2)$:

$$R_e^j = \sum_i (1 - \boldsymbol{v}_i . \boldsymbol{v}_e) \tag{5.24}$$

The best frame orientation occurs at minimum of R_e^j. The element (e) is added to the visited vector and the next adjacent element is considered. While following this procedure does not ensure that singularities are prevented, they occur only in the void or solid region and not in the area with intermediate density for the test cases considered in this research. After combing procedure, the mapping functions are obtained using equation (5.22) and the homogenized design is projected using equation (5.21). The projected design for the periodicity parameter $\Lambda = 0.065$ is shown in Figure 5.7 (a). Post-projection treatment must be implemented to ensure the manufacturability of the optimized designs.

Details of the post-processing framework are discussed in our previous work (Tamijani, Velasco & Alacoque, 2020). A summary of the process is outlined here. The process consists of five steps: 1) implementing the minimum feature size; 2) enforcing

the density threshold; 3) imposing the density boundary; 4) removing small holes; and 5) eliminating floating members and smoothing boundaries.

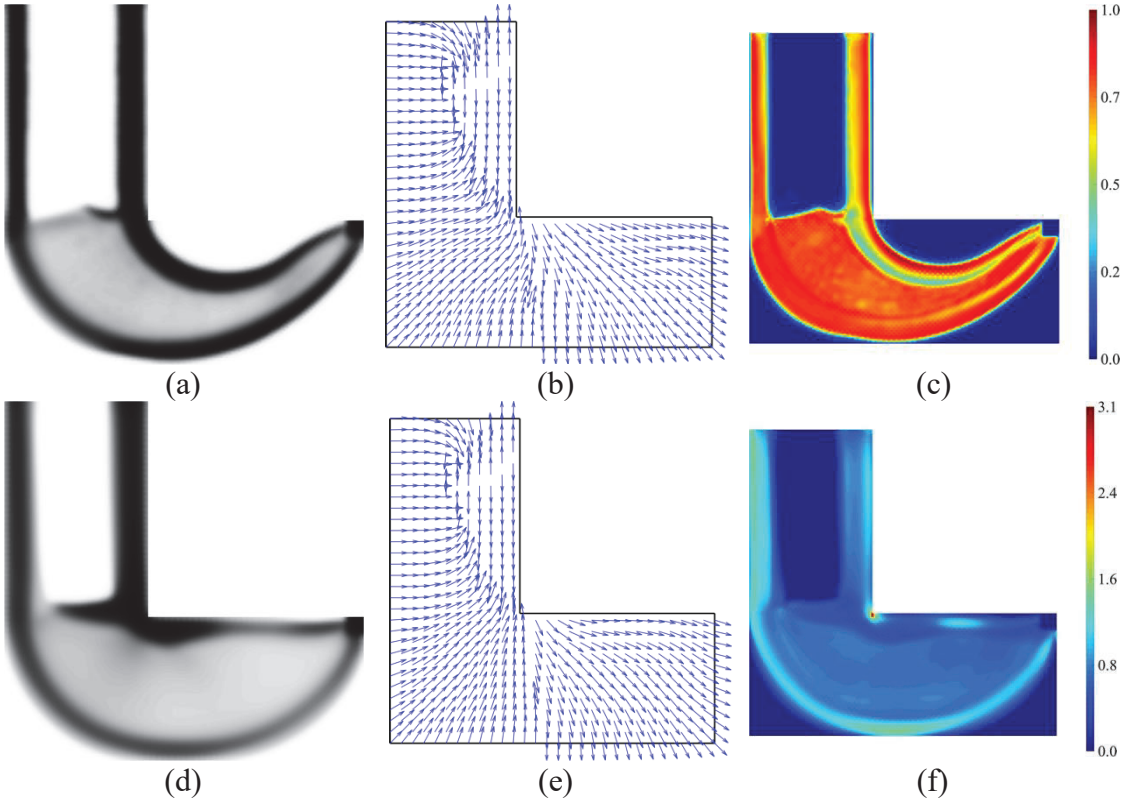

Figure 5.6. Optimized stress-constrained design: (a) material distribution; (b) orientation; and (c) failure index (F_e^r). Optimized compliance-based design: (d) material distribution; (e) orientation; and (f) failure index (F_e^r).

Within the first step, the cell size is defined based on the modified periodicity ($t_f = \Lambda e^{-\gamma}$ (Allaire, Geoffroy-Donders & Pantz, 2019)), which is plotted in Figure 5.7 (b). Cells smaller than $2h_{min}$ ($h_{min} = 0.3\Lambda$ is selected for the L-bracket projected designs) are identified and two conditions are used to ensure that all features are greater than the minimum threshold (h_{min}). Small cells ($t_f < 2h_{min}$) in the region $\rho \leq 0.5$ are removed ($1 - h_n = 0$). The small cells that fail that condition are made solid ($1 - h_n = 1$). The

Heaviside filter is then applied to the material indicator value ϕ eliminating some of the floating members at low density regions. Figure *5.8* (a) shows the resulting design.

The second step modifies the thicknesses of the features in the $t_f \geq 2h_{min}$ region based on the condition that if $\rho > \rho_{th}$ (for a given density threshold ρ_{th}) and $t_f h_n < h_{min}$, then $t_f h_n$ is set equal to h_{min}. Otherwise, the member is removed. The thicker members among the small cells at the center left of the design in Figure 5.8 (b) compared to Figure 5.8 (a) are visible. The boundaries of the projected design might exhibit gaps for some periodicities. In the third step, this issue is addressed, and the boundaries are preserved. The density distribution is modified by setting regions with $\rho > 0.7$ to 1 and superimposing them on the design in step 2. Consequently, a thick boundary is seen in Figure 5.8 (c).

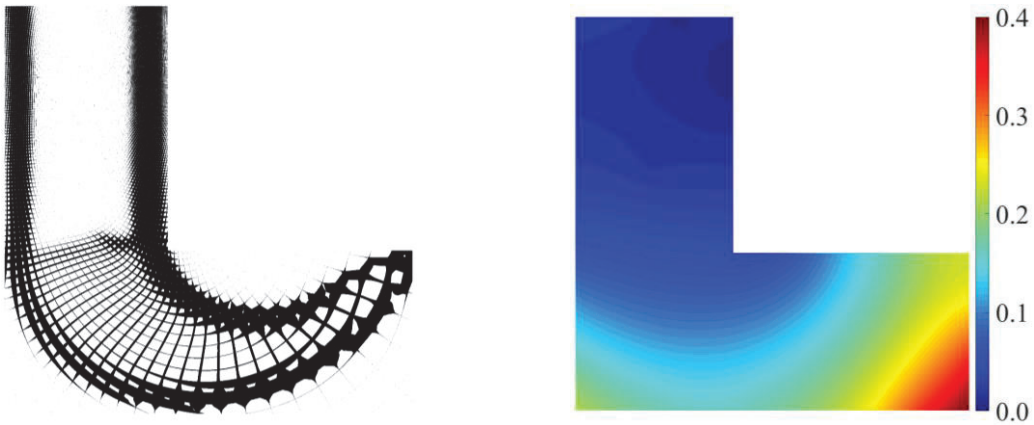

(a) (b)

Figure 5.7. The projected (a) stress-constrained design and (b) feature size for $\Lambda = 0.065$.

In the fourth step, the small regions are filled to guarantee manufacturability and improve structural performance. For this effect, the analog lattice is thresholded with

h_{min} and superimposed on the design from the previous step (Figure 5.8 (c)). The complement of the superposition is partitioned into regions. Regions for $\rho > \rho_{th}$ with inscribed circles smaller than h_{min} of the diameter are filled. This produces the shape shown in Figure 5.8 (d).

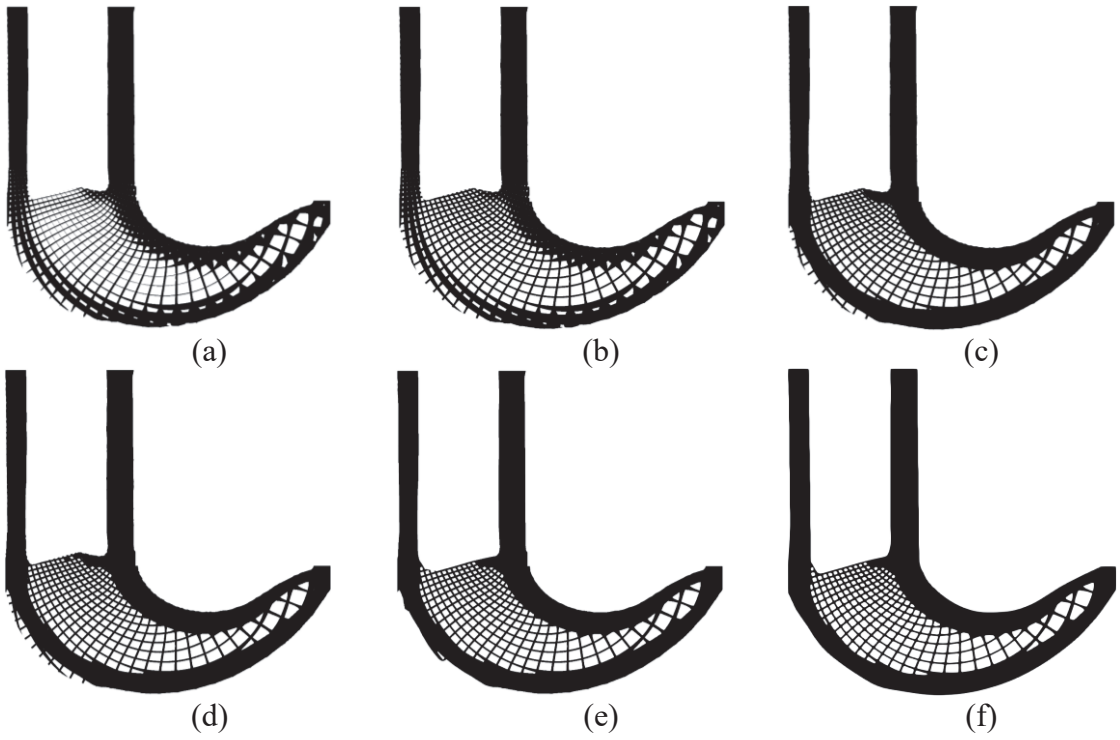

Figure 5.8. Projected design: (a) after implementing the minimum feature size; (b) after increasing the thicknesses of members where $\rho > \rho_{th}$; (c) after superposing the density boundary; (d) after small regions have been filled; (e) without floating members; and (f) with smoothed boundaries.

In the last step, the closed holes inside the design are filled temporarily and their complement is divided into two regions: the solid and void. The shapes of these regions are created using Delaunay triangulation. Adjusting the triangulation factor produces smoother boundaries and exposes vertices inside the boundaries of the regions. These

vertices are added to the regions, eliminating floating members. The complement of the shape is taken and the interior holes remain unfilled (Figure 5.8 (e)). Several iterations might be required to remove all of the floating members.

To produce a smoother shape, the boundary points created using a non-uniform rational basis spline (NURBS) are added to the projected design. Finally, the projected design is imported into MeshLab and is further smoothed using Taubin Filtering with 45 smoothing steps (Figure 5.8 (f)). As will be shown later, the outlined post-processing may increase the volume of the optimized structure.

In addition to the stress-constrained design with $\Lambda = 0.065$ (Figure 5.8 (f)), the post-processed projected stress-constrained design with a larger periodicity ($\Lambda = 0.13$) is obtained and shown in Figure 5.9 (a). The post-processed projected compliance-based design with $\Lambda = 0.065$ is also shown in Figure 5.9 (b). The post-processed projected designs are analyzed using ANSYS for the same loading and constraint conditions as the optimization model. The failure index for the three designs is shown in Figure 5.10 (a) – (c). Weighted filtering is applied to a small radius of $0.02\ cm$ to eliminate the artificial regions of high stress concentration.

The small cells in the stress-constrained design for $\Lambda = 0.065$ produce a more uniform stress distribution than those in the design for $\Lambda = 0.13$. The maximum stresses of the projected stress-constrained designs are distributed over the central boundary of the L-shape. In contrast, the compliance-based design has a high stress concentration at the sharp middle corner that leads to premature yield. The results demonstrate the effectiveness of stress-constrained optimization.

The compliance and failure indexes are reported in Table 5.4. Upon comparing Table

5.4 to Table 5.3, it is observed that post-treatment decreases the compliance by 29% and 25% for the stress-constrained and compliance-based designs, respectively. This difference is explained by the 17% and 26% increases in the volume fractions of the stress-constrained and compliance-based designs, respectively.

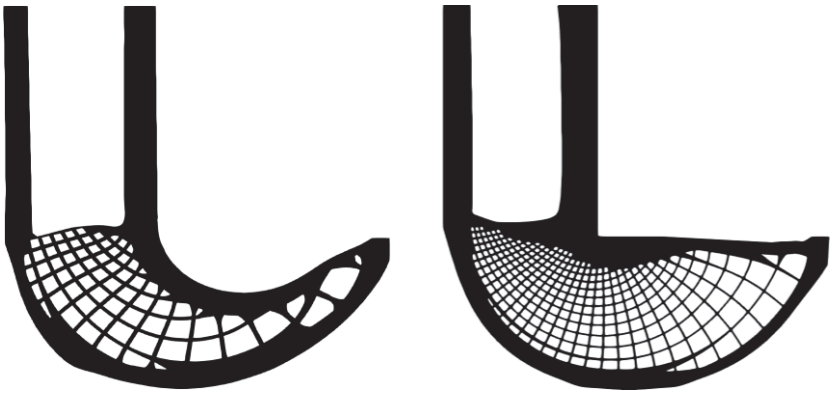

Figure 5.9. Post-processed projected designs produced via (a) stress-constrained optimization with $\Lambda = 0.13$ and (b) compliance-based optimization with $\Lambda = 0.065$.

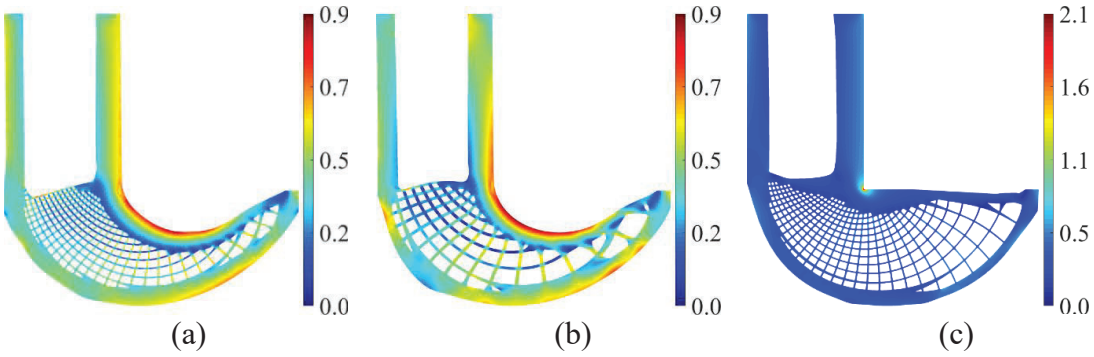

Figure 5.10. Failure indexes for the three optimized designs: (a) a stress-constrained optimized design with $\Lambda = 0.065$; (b) a stress-constrained optimized design with $\Lambda = 0.13$; and (c) a compliance-optimized design with $\Lambda = 0.065$.

Table 5.4

The volume fraction, compliance, and failure index for post-treated L-bracket designs

Designs	V_g	**SE** (Ncm)	$\max(F_e)$
Stress-constrained, $\Lambda = 0.065$	39.2	20	0.9
Stress-constrained, $\Lambda = 0.13$	39.4	20	0.9
Compliance-based, $\Lambda = 0.065$	42.3	15	2.1

5.5. Experimental Evaluation of Lattice Structures and Solid Isotropic Materials with Penalization Designs

The second test case considered in this research is the single-edge notched bend problem. Figure 5.11 shows the dimensions and boundary conditions of the SENB test case. The thickness of the structure is $20\ mm$. The notch causes stress concentration at its tip. The distributed load ($F = 240\ N/mm$) is applied over $6\ mm$ in the middle of the top surface. A region with an area of $12 \times 6\ mm^2$ near the applied load is excluded from the design domain. The domain is discretized using 62,580 elements. A length parameter of $r_f = 3\ mm$ is selected. As in the previous case, the maximum of the projection parameter is $\beta = r_f/\sqrt{3}l_e$ with $l_e = 0.04$, and ten regional stress constraints and a p-mean parameter of $p = 10$ are selected.

The optimized material distributions for the compliance-based and stress-constrained designs are shown in Figure 5.12, and the corresponding volume fraction, specific stiffness, and yield load are reported in the homogenized design section of Table 5.5. The reported effective specific stiffness (K_{eff}) is obtained from $K_{eff} = \frac{F}{V_f \delta}$, where δ is the deflection at the top region where the load (F) is applied.

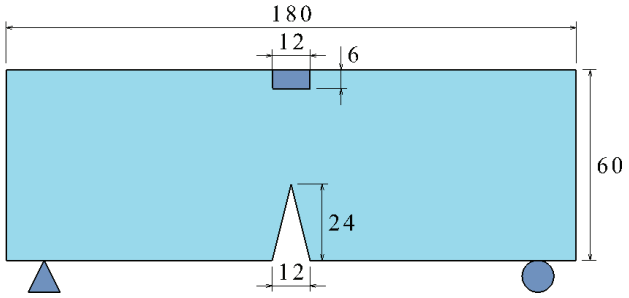

Figure 5.11. The SENB test case with dimensions in mm.

The post-processed lattice structures are shown in Figure 5.13 (a) and (c). The minimum manufacturable feature size is $h_{min} = 0.8\,mm$. Some of the small holes in the post-processed designs are filled and the walls thickened to comply with the minimum manufacturable feature size. This leads to a considerable increase in the volume fraction (V_g) as reported in the projected design section of Table 5.5. The effective stiffnesses and yield loads for the projected designs are also reported in Table 5.5. As shown in the table, in the case of the compliance-based design, the specific stiffnesses of the homogenized and projected designs differ by 15.6% because the projected model has a larger volume fraction that reduces the specific stiffness considerably. The increased volume has a less adverse effect on the specific stiffness of the stress-constrained design.

(a) (b)

Figure 5.12. Optimized (a) stress-constrained and (b) compliance-based designs.

The test case is also optimized using a solid isotropic material with penalization (SIMP) method. In SIMP, the elastic modulus is related to the density using a power law in order to penalize the intermediate density and restrict the design space to obtain a solid-void design. Details of the SIMP method with stress constraint implementation are discussed in Ref. (Le et al., 2010). A compliance-based design and a stress-constrained design were generated using the SIMP topology optimization. The SIMP designs are shown in Figure 5.13 (e) and (g). The volume fractions, effective stiffnesses, and yield loads of the SIMP designs are reported in Table 5.6. Figure 5.13 shows the failure index distribution for a load of 1440 N.

As in the optimization model, the region near the load application (blue rectangle) is neglected in the stress analysis. Concentrated stress is eliminated in the stress-constrained models, which exhibit more uniform stress distributions throughout the structure. The stresses on the SIMP stress-constrained design (Figure 5.13 (f)) are uniformly high throughout the structure, while the lattices in its homogenized counterpart (Figure 5.13 (b)) seem to provide low stress and good load transfer from load application to support through the solid regions. The latter design exhibits high stresses mostly at the bottom bulky region and the inner sides of its legs. The compliance-based designs yield considerably sooner than the stress-constrained designs due to high localized stresses in the notch and at the inner sides of the legs (Figure 5.13 (d) and (h)). These results are expected since the stress constraint is not implemented in the compliance optimization approach. The homogenization-based, compliance-based design also exhibits significantly high stresses on its thin, outer members (Figure 5.13 (d)) since they are quite thin and play an important role in transferring the load to the supports.

Table 5.5

Yield loads (F) and stiffnesses (K_{eff}) for homogenization-based designs

Designs	Optimized Design			Printed Design		
	Homogen. design	FEA for proj. design	% diff	FEA	DIC	% diff
Homogenization-based, stress-constrained design						
$\mathbf{V_g}$	22.9%	28.0%		30.4%	30.4%	
F (N)	1440	1440	0.00	1350.00	1451.05	7.22
δ (mm)	3.30	2.72	19.27	2.43	2.39	1.29
$\mathbf{K_{eff}}$ **(N/mm)**	1905.52	1890.76	0.78	1831.37	1993.95	8.50
Homogenization-based, compliance-based design						
$\mathbf{V_f}$	22.9%	28.5%		29.7%	29.7%	
F (N)	360.00	370.18	2.79	420.00	415.00	1.20
δ (mm)	0.63	0.60	3.40	0.72	0.78	6.95
$\mathbf{K_{eff}}$ **(N/mm)**	2515.28	2151.57	5.59	1949.77	1797.12	8.15

The models were manufactured using a PA12 printer with multi jet fusion (MJF) technology and tested experimentally in an MTS system with a 50 kN load cell. Three modifications are introduced to the designs to make them experimentally reliable (Figure 5.14 (a), (c), (e), and (g)). To allow more surface area for the roller constraints and prevent the supports from sliding off the rollers, the lower supports are extended.

The first set of tests reveals that the top of the model tends to slide off to the side (Figure 5.15). To address this rigid translation, a semi-circular crown is added such that the top roller can fit inside while remaining as centered as possible throughout the test. The described modifications are responsible for the increased volume fractions among the printed designs in Table 5.5 and Table 5.6. Due to these alterations, Table 5.5 and Table 5.6 distinguish between optimized and printed models. It is also observed that the support legs, especially those of the stress-constrained designs, rotate too easily as the

load increases. Thus, the models fail to reproduce the desired boundary conditions. A thick aluminum plate is placed between the parts and the support rollers, as shown in Figure 5.14. However, the homogenization-based, compliance-based design is tested without the plate since the portion of its bottom region near the constraints is low and would hit the plate at high loads. For these reasons, a rotation was verified for this sample, as will be discussed later.

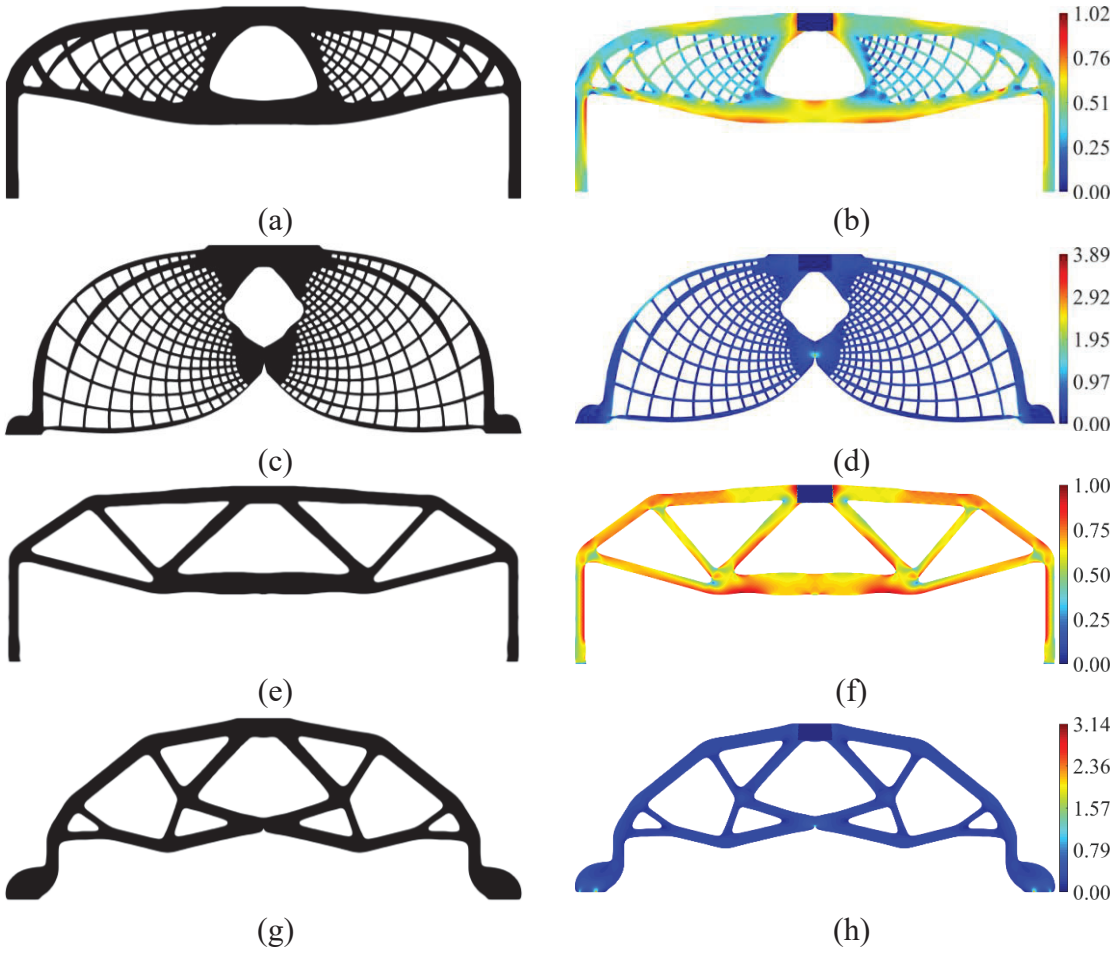

Figure 5.13. SENB-optimized designs and failure index distributions at 1440 N: (a) and (b), the homogenization-based stress-constrained design; (c) and (d), the homogenization-based compliance-based design; (e) and (f), the SIMP stress-constrained design; and (g) and (h), the SIMP compliance-based design.

Table 5.6

Yield loads (F) and stiffnesses (K_{eff}) for SIMP designs

Designs	**Optimized Design**	**Printed Design**		
	FEA	**FEA**	**DIC**	**% diff**
SIMP stress-constrained design				
$\mathbf{V_f}$	19.9%	22.1%	22.1%	
F (N)	1440.00	1425.00	1360.00	4.67
δ (mm)	3.52	3.35	3.21	4.26
$\mathbf{K_{eff}}$ **(N/mm)**	2056.77	1924.17	1916.31	0.41
SIMP compliance-based design				
$\mathbf{V_f}$	21.8%	24.6%	24.6%	
F (N)	458.60	590.00	645.00	8.91
δ (mm)	0.87	0.86	0.83	3.62
$\mathbf{K_{eff}}$ **(N/mm)**	2432.96	2786.93	3159.03	12.52

The displacements were measured using DIC. Symmetry was assumed and the two DIC cameras were focused on one side of the structure to magnify the field of view and increase the resolution. This was especially important for lattice structures with smaller members. Figure 5.16 shows the applied force per volume fraction versus the vertical displacement per unit of structure height (H) for the four samples. The yield loads (F) for the experimental evaluations reported in Table 5.5 and Table 5.6 are determined from the 0.2% offset line of the curve presented in Figure 5.16.

The experimental and computational displacement contours at yield are shown in Figure 5.17 (a) - (h). The two sets of contours for each design are in good agreement and the computational model predicts a slightly higher maximum displacement than is observed experimentally. However, the homogenization-based, compliance-based design seems to be an exception. For this model, the experimental displacements are higher than

the computational displacements. This might indicate that the real model is less constrained and rotates more than is predicted via FEA. Another reason for this discrepancy might be that bending of the real sample is not perfectly symmetric.

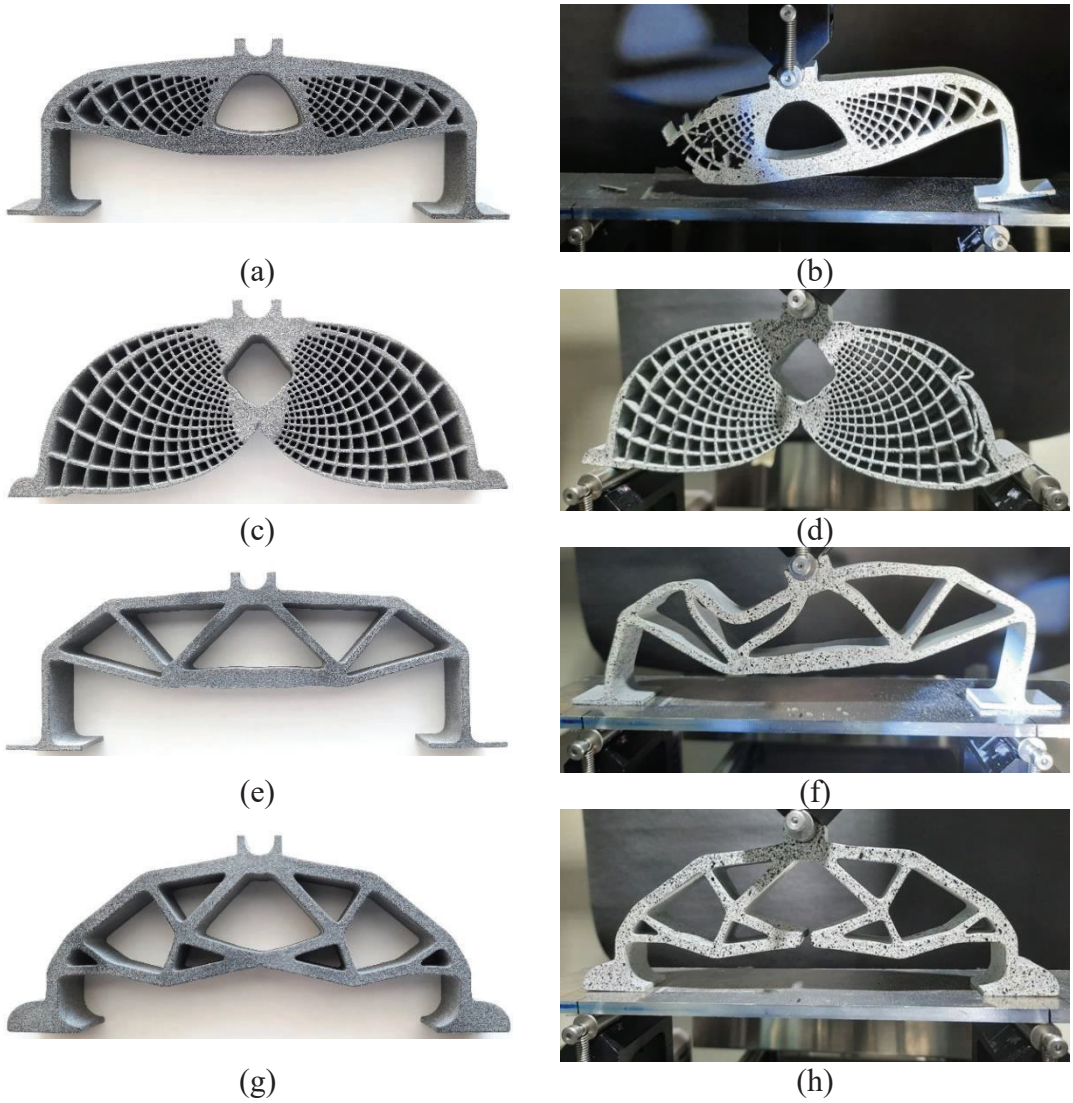

Figure 5.14. Designs produced via AM: the homogenization-based, stress-constrained design (a) before and (b) after testing; the homogenization-based, compliance-based design (c) before and (d) after testing; the SIMP stress-constrained design (e) before and (f) after testing; and the SIMP compliance-based design (g) before and (h) after testing.

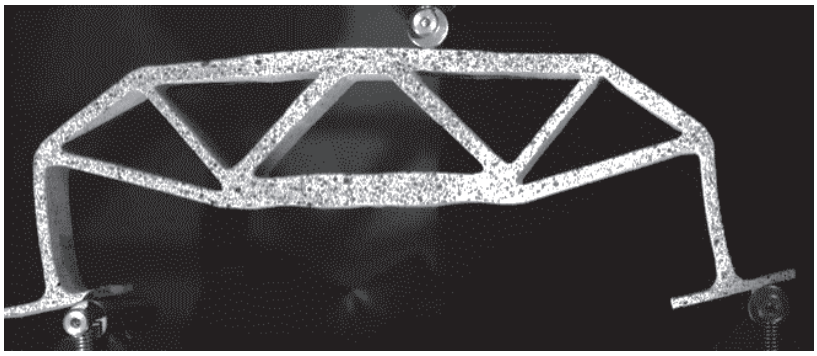

Figure 5.15. A three-point bending test showing the specimen sliding off the rollers.

As shown in the printed design computational and experimental results in Table 5.5, the homogenization-based, stress-constrained design exhibits an enhanced yield load. Both the yield load and specific stiffness for this design are similar to those of the homogenized and projected designs. Overall, this design provides a higher ultimate strength than the other three designs (Figure 5.16). As the load increases, some of its thin walls deflect, buckle, and ultimately break (Figure 5.14 (b)).

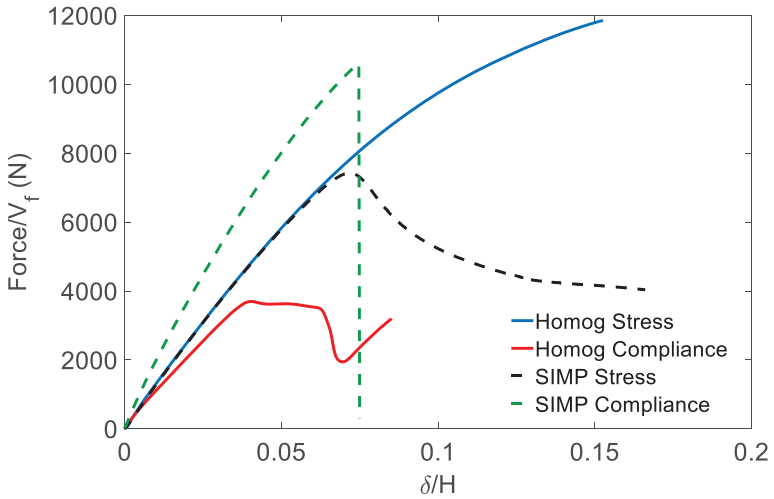

Figure 5.16 The force (per volume fraction) versus DIC vertical displacement (per unit of structure height) plot.

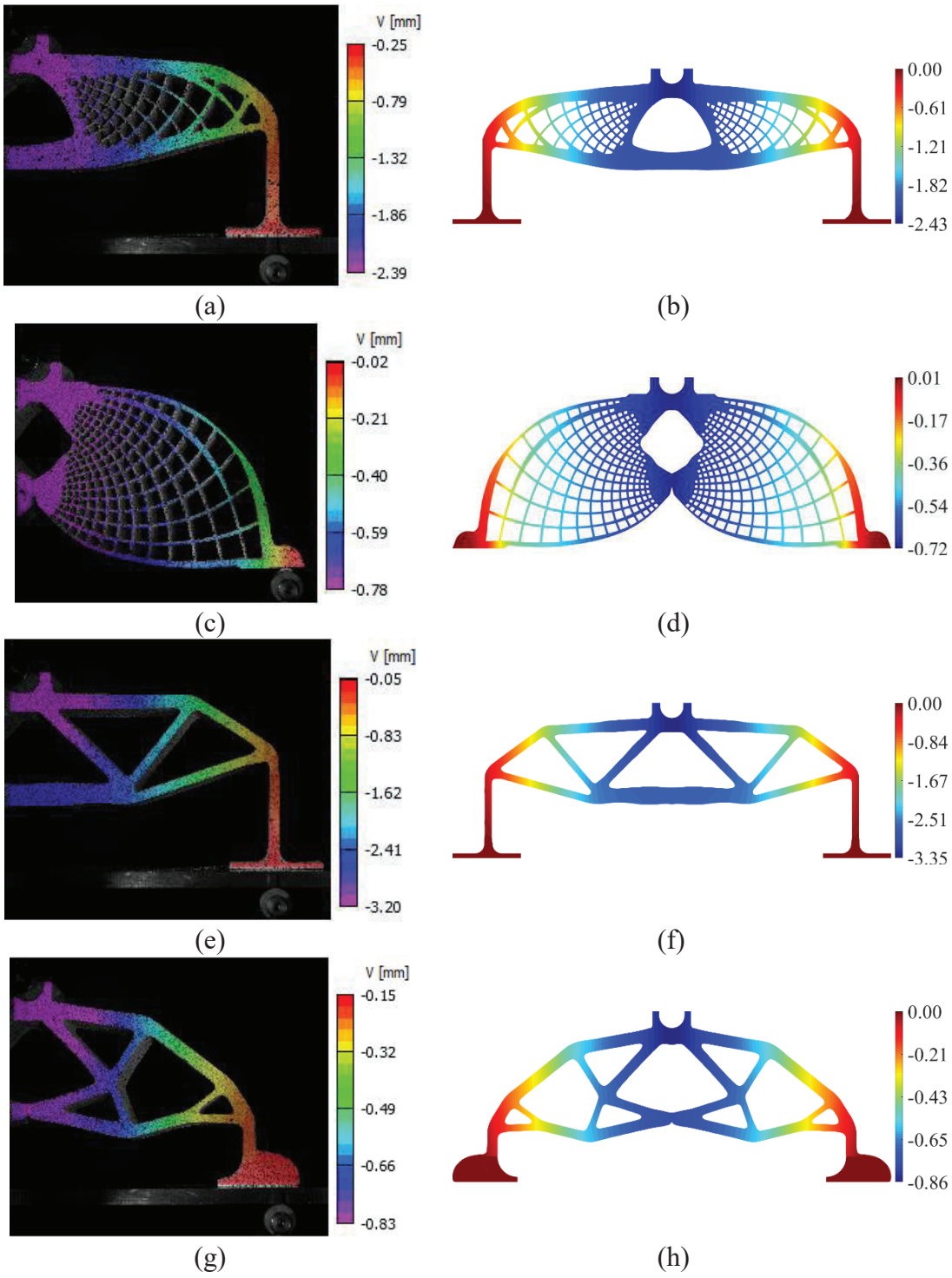

Figure 5.17. Displacement contour plots [mm] for three-point bending for the: (a) experimental and (b) computational homogenization-based, stress-constrained design; (c) experimental and (d) computational homogenization-based, compliance-based design; (e) experimental and (f) computational SIMP stress-constrained design; and (g) experimental and (h) computational SIMP compliance-based design.

The homogenization-based, compliance-based design has the lowest stiffness and strength of the four designs. It exhibits high plasticity and deforms considerably before some of its thin members buckle (Figure 5.14 (d)). Although the computational model exhibits some deformation among the thin walls, it predicts yield due to a high stress concentration at the point where the bottom supports touch the rollers. This design has low stiffness because its supports rotate (see Figure 5.14 (d)) since no plate is used. FEA of the homogenization-based, compliance-based design shows that the stiffness would be closer to that of the SIMP compliance-based design ($2678.5\ N/mm$ instead of the $1949.8\ N/mm$ shown in Table 5.5) if no rotation was allowed. This demonstrates that similar specific stiffnesses can be achieved using the SIMP and homogenization methods for the same boundary conditions.

Upon comparing the printed design experimental and computational results reported in Table 5.5 and Table 5.6, it can be seen that the stress-constrained lattice and SIMP designs exhibit similar specific stiffnesses. Both the experimental (Figure 5.14 (f)) and computational models of the SIMP stress-constrained design demonstrate yield due to bending. The specific stiffnesses of the two models are in good agreement and differ by less than 1%. Experimentally, the model deflects more on one side, Figure 5.14 (d) despite the effort made to center it during test preparation.

Comparison of the printed and optimized models in Table 5.6 indicates similar specific stiffnesses and yield loads. This occurs because the supports are thin and compliant and extending them for testing did not produce significant effects.

The experimental and computational SIMP compliance-based designs yield expectedly due to high stress concentrations at the notch as the load increases (Figure

5.14 (h)). The bulky bottom supports provide more stability and better load bearing, resulting in better stiffness than other models, especially relative to the stress-constrained designs in which the long, thin supports tend to buckle. The FEAs of the printed and optimized designs indicate that the modifications made to the SIMP compliance-based design to make it testable affect its yield load and stiffness. The experimental model is 13% stiffer than computationally predicted. This might indicate that the boundary conditions applied in the FEA model do not fully resemble the real boundary conditions. That is, the aluminum plate provides a much stiffer contact than is predicted computationally. The printed designs also have higher yield loads since their bulky supports become even stronger when additional material is added.

Overall, the experimental and computational models, Figure 5.17 (a) – (h), are in good agreement with the maximum 12.5% difference in the stiffness of the SIMP compliance-based design. This difference can be attributed to the difficulty of applying perfectly symmetric constraints and loading conditions experimentally and the difficulty of reproducing the experimental boundary conditions via FEA.

6. Analysis of an Additively Manufactured Flexible Wing Model

An optimized fighter wing was additively manufactured and tested in a low-speed wind tunnel to obtain the aerodynamic coefficients and deflections at different speeds and angles of attack. This data was used to validate a finite element framework that will be utilized in the future study of the aeroelastic performance of different wing models. Although the model chosen was a supersonic fighter wing, it was tested in a low-speed wind tunnel for variety of subsonic wind speeds and angles of attack for proof-of-concept and validation purposes.

6.1. Wind-Tunnel Model

A supersonic fighter wing was selected as the model in this study. The weight of the model was optimized by Locatelli, Mulani and Kapania (2011) subjected to stress and buckling constraints. The particle-swarm optimization was performed considering the internal topology, the size of the skin, spars and ribs as design variables. The optimized wing (2.4 m semi-span, 2.54 m root chord and 0.84 m tip chord) has curved spars and ribs which have shown to produce lighter designs with better aeroelastic and structural performance (Fernandes & Tamijani, 2017; Locatelli, Mulani & Kapania, 2011).

The planform model was scaled down by a factor of 5.2 due to the limitation of the manufacturing built volume. The dimensions of the wing shown in Figure 6.1 are different from the wing planform reported in Locatelli, Mulani and Kapania (2011)'s article because a 2.59 mm thickness was attributed to the skin extending the chord by 11.03 mm at the leading edge and 35.44 mm at the trailing edge so that the top and bottom skin could meet in a single edge.

The model was further modified to comply with the manufacturing and test requirements discussed later. The geometry and size of the model is shown in Figure 6.1

and listed in Table 6.1. Since the data for the original airfoil NACA 65A004.8 was not available, the symmetric NACA 64A006 (Abbott & Von Doenhoff, 2012) was modeled instead. A blunt trailing edge (TE), shown in Figure 6.1 (b) was considered since the sharp TE would be too thin to meet the minimum manufacturable thickness as discussed later in this chapter. However, this modification came with a compromise since blunt TEs cause flow recirculation and flow separation more upstream than the sharp counterpart (Thompson & Whitelaw, 1988).

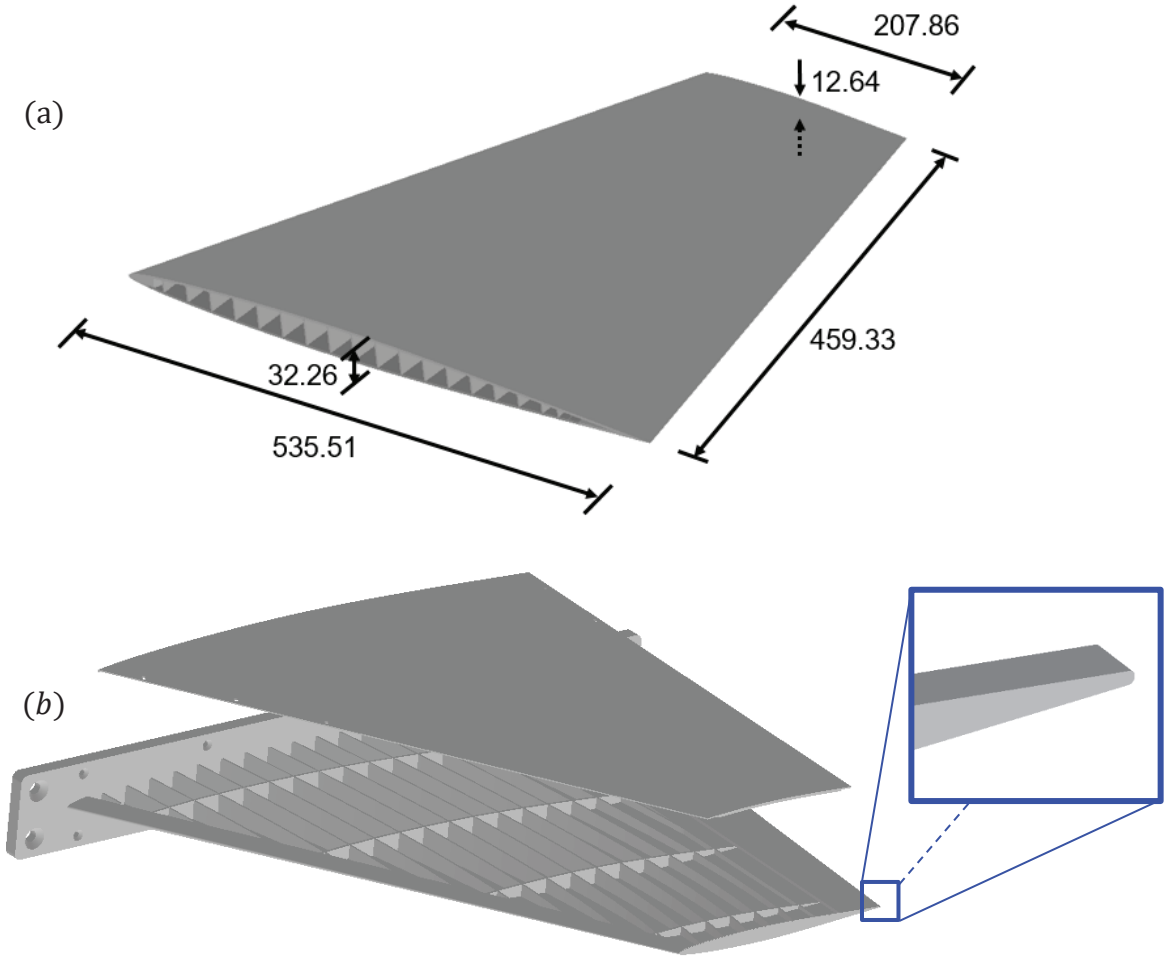

Figure 6.1 (a) Wing geometry with dimensions in mm (b) wing model showing bottom skin detached from the rest of the model and blunt trailing edge.

Table 6.1

Summary of the model dimensions

Dimensions	**Value**
Semi-span (mm)	459.33
Root Chord (mm)	535.51
Tip Chord (mm)	207.86
Root Airfoil Thickness (mm)	32.26
Tip Airfoil Thickness (mm)	12.64
Quarter Chord Sweep Angle (°)	24.03
Skin Thickness (mm)	2.59
Spar Thickness (mm)	1.73
Rib Thickness (mm)	2.34

Initially, the model was printed in PA12 through SLS. However, due to its large dimensions and thin skin as well as the nature of SLS (operates at high temperatures and parts cool off at uneven rates), the residual stresses caused warping as shown in Figure 6.2. Later, the wing was successfully printed without warping and with smoother surface finish through SLA using a 3D Systems ProX 950 printer. See Figure 6.3. The model was built layer-by-layer in the span direction. The build time was around 24 hours for a layer thickness of 100 μm. The material was chosen based on the availability and its properties. The selected Accura 25 is a resin similar to ABS and polypropylene which, according to preliminary calculations, would resist the wind forces but would not be too stiff to prevent visible deformation. The material properties of Accura 25 were determined according to ASTM D638-14: $E = 1377\ MPa$, $\nu = 0.37$ and $\rho = 1190\ kg/m^3$.

The model was modified to account for the manufacturing and experimental constraints. The initial focus was satisfying the experimental requirements. 1) A mounting base was added to the model to allow it to be properly attached to the wind tunnel turntable. 2) The model could not be scaled down below 457 mm span to allow

detectable deformation with the apparatus used; not only for the fact that reducing the size increases the stiffness but also because the deformations would become difficult to capture through the glass window of the tunnel with the set of cameras outside. 3) Printing the model in more than one part was not desirable to prevent surface irregularities and mismatches resulting from printing tolerances and gluing parts together. 4) Any modification made or hardware used should not disturb the wind flow.

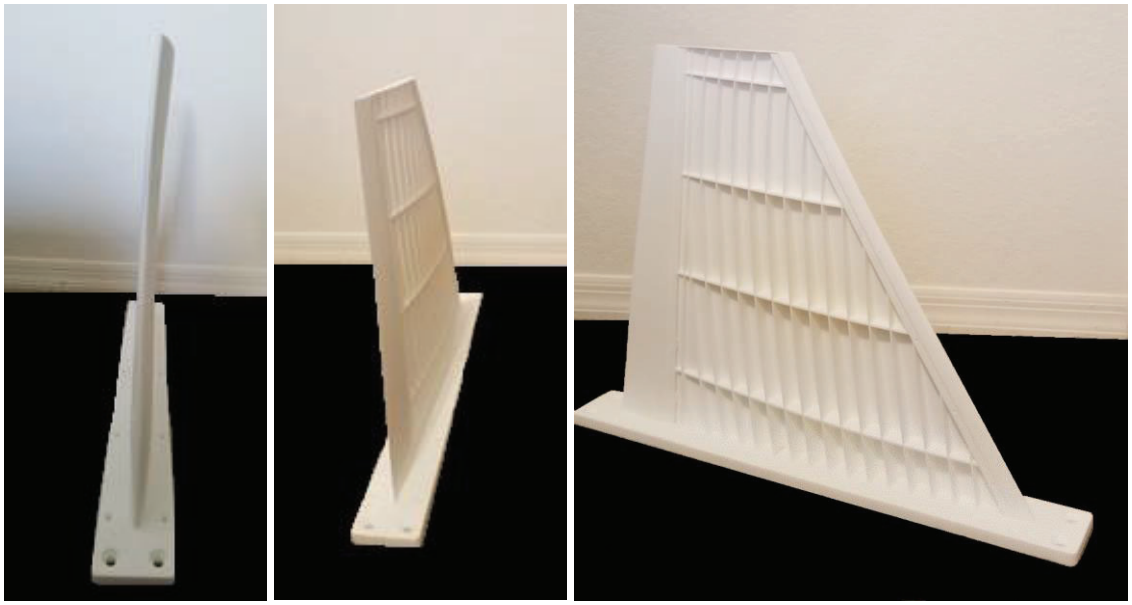

Figure 6.2 Warped SLS wing model.

With these four constraints in mind, the manufacturing constraints were also considered. 1) For the AM technique used the maximum build volume was 1500 x 750 x 550 mm and the minimum feature size was 0.6 mm. Any feature smaller than that was changed to the minimum size. 2) the bottom skin was printed separately, as shown in Figure 6.1 (b) to allow any excess material to be removed after printing. Escape holes

through all the spars and ribs would not be as effective in eliminating the excess material and would compromise the structure's strength. Although the wing was, therefore, printed in two pieces, the cavity was created on the bottom of the wing and it was glued (using a two-part epoxy) and sanded to ensure surface smoothness and reduce flow perturbation.

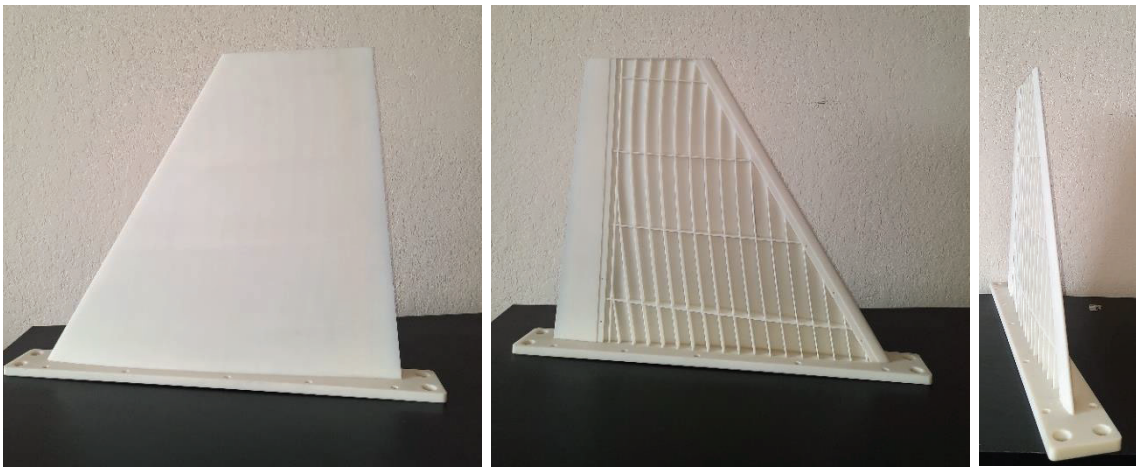

(a) (b) (c)

Figure 6.3 Additively manufactured wing model: (a) top surface, (b) bottom surface without cover skin and showing internal structures and (c) side view showing no warping.

6.2. Wind Tunnel and Set-up

The model was tested in a low-speed closed circuit wind tunnel at Embry-Riddle Aeronautical University facilities. Capable of reaching Mach number 0.38 with a 1200 hp motor, the test section is 1.8 m wide, 3.65 m long and 1.2 m tall. The wing was vertically mounted to the turntable on the floor of the test section as shown in Figure 6.4. This position was chosen taking advantage of the screw holes on the turntable and avoiding modifications to the wind tunnel set-up.

(a)

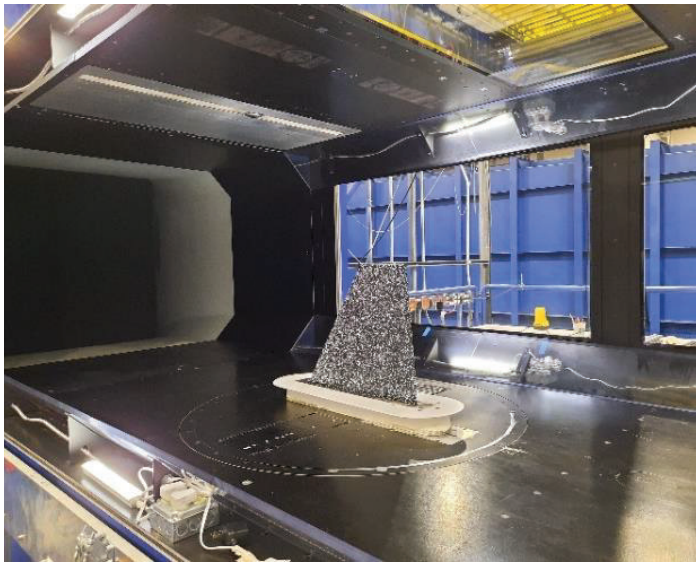

(b)

Figure 6.4 Model inside wind tunnel test section: (a) outside view and (b) inside view.

The wing was bolted to a thick aluminum plate which provided some stiffness to its plastic base. The aluminum plate was bolted to the steel post that mounted to the force balance. The aluminum plate and the base of the wing were involved by a splitter plate which is bolted to the turntable and is used to inhibit the effect of the boundary layer from the floor on the model, reducing the drag. The splitter plate was modeled according

to the guidelines established by Diebold et al. (2015) and fabricated with SLS PA12. The distance between the leading edge of the splitter plate and the wing leading edge was 25% of the chord. The plate shown in Figure 6.4 was 273 mm wide, 6.35 mm thick and with edge profile based on NACA 0012 airfoil.

A DIC system composed of two high resolution cameras (AF Nikkor 60 mm f/2.8D) were used to measure deflection during the test. The cameras were mounted outside the wind tunnel at approximately 90 degrees from each other. The wing model was spray painted in black with white random speckle particles. DIC measures deflection by tracking the change in position of the speckles relative to the reference image (at zero speed). The cameras collected 10 s of images for a set speed and angle of attack.

6.3. Finite Element Model

Three different groups were identified from the CAD model: the skin, spars and ribs. A brief inspection has shown that considering the base of the wing would not affect the results. Therefore, the base was ignored to reduce the mesh and computational time. The midsurfaces of each component were extracted, imported and meshed in MSC. Patran with 94,000 linear triangular shell elements (CTRIA3). A surface mesh was preferred since a solid mesh would be computationally expensive.

Contact bodies were implemented to ensure proper connection between the different parts. All degrees-of-freedom, except the out-of-plane translation (y-axis) and the rotation about the y-axis, for the nodes at the wing root were constrained. A torsional spring element about the y-axis was applied to those nodes. The springs had a stiffness close to the estimated torsional stiffness of the wing ($70\ kNm^2$). The translation in the y-axis for the nodes at the wing root midsurface were also constrained.

A MATLAB framework was developed to generate and run the Nastran input file

(.bdf) for different types of analyses such as static structural, modal, buckling, static aeroelasticity and flutter. The framework requires the user to provide the mesh, loading, boundary conditions, material properties and flow characteristics for the case of aeroelastic analyses.

In the aeroelastic analysis, the loads are computed in a new grid (aerodynamic boxes) and the displacements are computed in the structural grid. The interpolation of the results between the two grids happens through the use of splines. Nastran computes the aerodynamic loads using the Doublet Lattice Method (DLM). The method is based on the linear potential theory and represents the lifting surfaces as trapezoidal boxes parallel to the flow. A pressure of unknown strength is assumed to act on the quarter chord line of each panel. The pressure is determined by satisfying the downwash boundary condition at the control points, located at ¾ chord, mid-span of each panel to satisfy the Kutta condition (Albano & Rodden, 1969). DLM is an extension of the Vortex Lattice Method (VLM) to unsteady flow, and it relates the pressure at the doublet line to the downwash at the control points ($p_i = \sum_{j=1}^{n} A_{ij} w_j$ where A_{ij} is the aerodynamic influence coefficient matrix). This relationship can be solved using virtual work and the pressure is used to compute the aerodynamic force coefficients (Tewari, 2015).

6.4. Results and Discussion

To validate the finite element model, the fighter wing was tested in the wind tunnel for a range of speeds from 46 m/s to 91 m/s, and for 36 angles of attack from -5° to 30°. The yaw, pitch, and roll angles were kept constant at zero. The test was run twice on different days to ensure repeatability. The aerodynamic loads and moments were recorded and the aerodynamic coefficients for five speeds are plotted against the angle of

attack in Figure 6.5.

As expected, the lift coefficient is directly proportional to the angle of attack for angles below 12°. The end of linearity indicates flow starts separating in certain parts of the wing. Due to the lift produced by the remaining attached flow the lift coefficient still increases up to the stall angle of 18° (Zhang et al., 2019). Up to that point, lift was the predominant load. Beyond stall, the lift coefficient decreases with the increase of the angle of attack. At low angles of attack (below 8°), the drag is low but it rapidly increases with lift as it approaches stalling. The coefficient of pitching moment at the quarter chord consistently decreases with lift in an almost linear fashion up to the stall angle. These observations are consistent with the study done by Zhang et al. (2019) on a subsonic 40° swept wing.

The described aerodynamic behavior is independent of the wind speed. That is the case for inviscid flow in which viscous effects are not significant compared to the potential forces. This observation is corroborated by the high Reynold's number shown in Table 6.2.

The aerodynamic coefficients as a function of angle of attack obtained computationally were plotted against the experimental curves demonstrating a very good agreement for the lift coefficient curve at angles of attack lower than the stall angle. The experimental and computational curves for the drag and moment coefficients are within acceptable agreement up to the stall angle. The finite element solution becomes invalid for higher angles of attack (near stall) because of its assumption of inviscid, linear potential flow (MSC, 1987) and the viscous effect becomes more critical for high angles of attack. Only the computational curve at 91 m/s is shown in Figure 6.5 since the

relationship between the aerodynamic coefficients and angle of attack is independent of the speed as previously discussed.

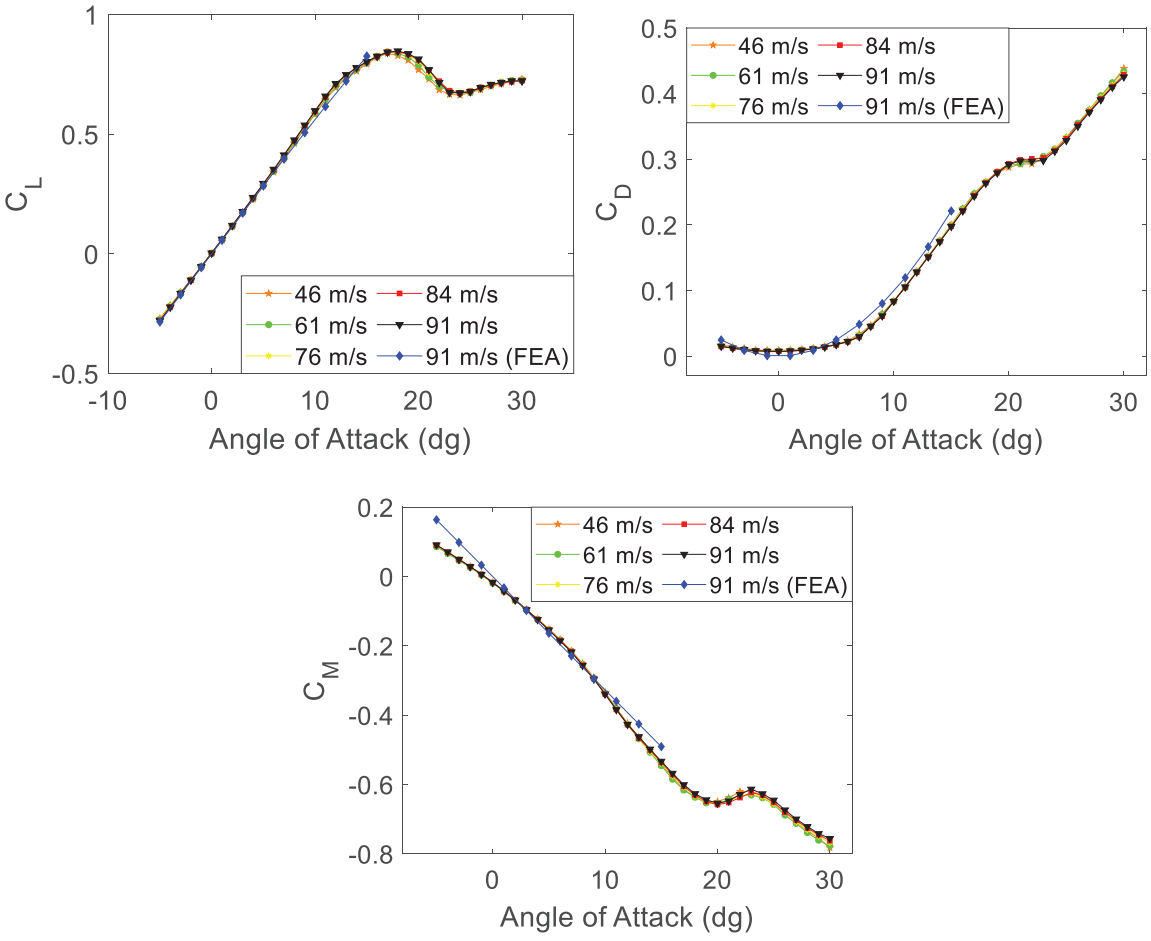

Figure 6.5 Variation of aerodynamic coefficients with angle of attack.

A closer look at the aerodynamic parameters and coefficients are present in Table 6.2 and Table 6.3 for a 10° angle of attack. The dynamic pressure (q), lift (L) and Reynold's number (R_e) were obtained experimentally. The three parameters expectedly increase with speed. The dynamic pressure, Mach number and angle of attack were used as input for the computational model. The computational and experimental results for the lift and

moment coefficient show very good agreement with less than 7% difference. However, a higher difference, yet less than 17%, is obtained for the drag coefficient.

Another important result is the out-of-plane deflection (δ) experimentally obtained using DIC at a sampling rate of 100 Hz for 10 s for a constant speed and 10° angle of attack. The deflection was averaged over time and the maximum value on the surface of the structure, which happens at the tip, is shown in Table 6.3. The computational and experimental results are in reasonable agreement with a maximum difference of 13%. The difference between the two sets of results increase with the magnitude of deflection and may be related to the resolution of the DIC system that becomes less accurate for displacements larger than 20 mm. This observation results from a preliminary test done by translating a flat plate pre-determined distances to check the setup and calibration of the cameras before the actual test.

Table 6.2

Wind tunnel data

$\boldsymbol{v}\ (\boldsymbol{m/s})$	$\boldsymbol{q}\ (\boldsymbol{Pa})$	$\boldsymbol{L}\ (\boldsymbol{N})$	$\boldsymbol{R_e}$
45.72	1234.94	122.00	1,097,487
60.96	2199.12	220.49	1,471,746
76.2	3415.50	345.84	1,826,089
83.82	4125.47	419.12	2,002,350
91.44	4899.59	499.39	2,178,286

The computational and experimental displacement contours at 45.72 m/s and 10°

angle of attack are also in good agreement as shown in Figure 6.6. The contours for the other speeds are similar and were omitted for sake of succinctness. Another important observation is that the roughness produced by the speckle particles did not significantly affected the results or compromised the validation. Overall, the aforementioned observations validate the computational aeroelastic model before stall condition.

Table 6.3

Comparison of experimental and computational aerodynamic coefficients and deflection

$v\ (m/s)$	Data	C_L	C_D	C_M	$\delta\ (mm)$
45.72	**Experimental**	0.58	0.08	-0.33	5.39
	FEA	0.55	0.10	-0.32	5.45
	% difference	5.90	-13.99	4.01	-1.07
60.96	**Experimental**	0.59	0.08	-0.34	10.14
	FEA	0.55	0.10	-0.32	9.76
	% difference	6.19	-15.06	4.57	3.86
76.2	**Experimental**	0.59	0.08	-0.34	16.90
	FEA	0.56	0.10	-0.32	15.28
	% difference	6.53	-15.49	4.33	10.06
83.82	**Experimental**	0.60	0.08	-0.34	21.01
	FEA	0.56	0.10	-0.33	18.56
	% difference	6.44	-16.39	4.06	12.40
91.44	**Experimental**	0.60	0.08	-0.34	25.15
	FEA	0.56	0.10	-0.33	22.18
	% difference	6.26	-16.83	3.62	12.57

The computational and experimental displacement contours at 45.72 m/s and 10° angle of attack are also in good agreement as shown in Figure 6.6. The contours for the other speeds are similar and were omitted for sake of succinctness. Another important observation is that the roughness produced by the speckle particles did not significantly affected the results or compromised the validation. The aforementioned observations

validate the computational aeroelastic model before stall condition.

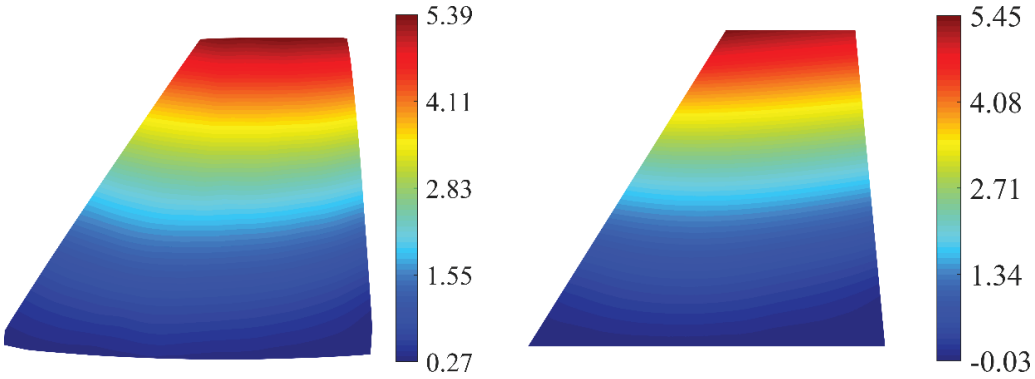

Figure 6.6 Out-of-plane displacement [mm] contours obtained from (a) DIC and (b) FEA at 45.72 m/s and 10° angle of attack.

7. Conclusions

This dissertation provides a feasibility study for different optimized variable-stiffness structures by demonstrating its manufacturability and enhanced stiffness and reduced weight. The first part of the research probed the effects of continuous fibers on the mechanical and viscoelastic properties of AM composites. Specimens made of neat Onyx and two different continuous fiber orientations were subjected to tensile and interlaminar shear tests and DMA. Delamination, porosity and failure mechanism were analyzed through SEM. The results from the interlaminar tests indicate that the continuous fibers tripled the ILSS of Onyx. The fiber-reinforced specimens showed some elasticity and failed due to delamination while the Onyx samples failed due to crack propagation exhibiting a more plastic behavior.

The tensile test highlighted the superior strength and stiffness of the AM continuous fibers compared to the Onyx. Although the two fiber layouts had the same stiffness, concentric fibers showed an ultimate strength 14% larger than the isotropic fiber infill since the fibers in the concentric layout progressively failed transferring the loads to intact fibers while the isotropic infill experienced crack propagation through the matrix and fiber pull-out. The failure of the tensile specimens was simulated using FEA and the results were in good agreement with the experimental.

DMA has been used in the viscoelastic characterization of AM continuous fiber composites. The results showed that the presence of continuous fibers increased the glass transition temperature by 53.8% (concentric) and 44.6% (isotropic) because the molecules require more energy to reach the rubbery state. The concentric fiber composite revealed a higher T_g because its storage modulus decreased with the increase of

temperature at a rate slower than the isotropic fiber infill due to the presence of the polymeric middle region. This fact was consistently observed at different frequencies leading to concentric samples with higher activation energy of glass transition relaxation than the isotropic fiber samples. The continuous fibers increased the activation energy by 26.5% (isotropic) and 84% (concentric) in comparison with Onyx. As a result, the concentric sample had the lowest creep rate.

The second part of the research demonstrated a comprehensive stiffness design optimization, AM, and testing/validation of continuous fiber composites for three benchmark problems. The fiber paths generated for an optimized cantilever plate, MBB beam, and L-bracket were additively manufactured. The computational specific stiffnesses was experimentally validated in collaboration with the University of Texas at Austin. The suitability of the SOMP and level-set optimization methods were shown to depend on the problem.

In many cases, the offset method leads to better results as it assumes fibers to be parallel to the boundary of the layout and often along the principal stress direction. The computational results agreed closely with the experimental ones in most cases, with a maximum difference of 18% for the EQS cantilever plate design. These discrepancies were due to the inability of the printer to perfectly match the designed fiber layouts. The optimized specific stiffnesses were compared with non-optimized geometries based on unidirectional laminates, such as those found in traditional composites. The optimized cantilever plate, MBB beam, and L-bracket improved parts' stiffness by up to 25%, 102%, and 90% compared with their respective non-optimized geometries.

The third part of this dissertation discusses the implementation of stress constraints in

topological and orientation optimization of lattice structures. The effective properties were calculated using the numerical homogenization method. The results were validated experimentally and then utilized in the optimization algorithm. Compliance-based and stress-constrained optimization algorithms were developed and homogenized designs were obtained. These designs were projected to generate optimized lattice structures. An advantage of the de-homogenization methodology is that optimization can be performed efficiently using a coarse mesh and high-resolution lattice structures can be obtained via projection onto a fine mesh.

Two case studies were considered to demonstrate the feasibility of the proposed method. For the first case, the L-shaped bracket, it was observed that the implementation of stress constraints during the optimization process resulted in removal of material at the re-entrant corner and a more uniform failure index distribution. For the SENB test case, the homogenization-based stress-constrained and compliance-based designs were compared to those obtained using SIMP. The two stress-constrained designs exhibited similar structural performance; the two designs had similar stiffnesses and yield strength.

Comparison to the compliance-optimized design indicated that stress-constrained optimization is effective in inhibiting yield but compromises stiffness. Experimental evaluation of the optimized designs showed that the additively manufactured models could reach the yield strength determined via the optimization algorithm. However, the experimental results also demonstrated the adverse effects of enforcing a minimum manufacturable feature size. This increases the volume fraction and thus decreases the specific stiffnesses of the lattice structures.

For the fourth and last part of this dissertation, an optimized flexible fighter wing was

modeled and fabricated through SLA after manufacturing considerations. The model was tested in a low-speed wind tunnel and the aerodynamic loads (lift and drag) and the pitching moment were recorded for different angles of attack and speeds. The aerodynamic coefficients were calculated and the displacements were captured using DIC. The experimental results were used to validate a computational framework that will be used to analyze the aeroelastic performance of different optimized wing models.

The present dissertation demonstrates the feasibility of different topology and orientation optimization frameworks and the manufacturability of the optimized designs owing to the advances in AM techniques. Also, the use of topology and orientation optimization and AM has resulted in lighter designs with superior stiffness or strength.

8. Future Recommendation

The analysis of the continuous fiber reinforced optimized parts demonstrated that the manufacturing constraints have a significant impact in the specific stiffness of the structure. Therefore, the author recommends the integration of the manufacturing constraints (fiber width, drilled holes, and fiber length) in the optimization framework. Future work should also extend the design of AM composites to 3D.

As for the third part of this dissertation, the computational and experimental results indicate the importance of including buckling constraints in future studies. As shown in the SENB compliance-based design, thin members are susceptible to buckling. Depending on the minimum member thickness, this may occur before the yield stress is reached. Another important observation is that while there was no intent to obtain coated structures with infill lattices, the optimized designs resemble them due to the use of a minimum manufacturable feature size and a material indicator variable to address stress singularities. The implementation of stress constraints to obtain coated structures and comparison of their performances to those reported in this article is the subject of future research. Future research also includes extension of this framework to 3D lattice structure designs.

Finally, for the last part of the work, a preliminary FEA study has shown that the type of fixed connection at the root of the wing could affect the critical stresses and play an important role in failure. Based on that, a failure analysis in FEA would provide a valuable insight for future models and experiments. Since the existing wind tunnel cannot not achieve higher speeds, it would be interesting to predict flutter through FEA. Furthermore, the computational framework could be applied to other wing models. Taking advantage of the benefits of the optimization of lattice structures, the framework

could be applied to wing model with optimized microstructure to compare the aeroelastic performance (flutter and divergence characteristics) and the aerodynamic coefficients between different wings. Previous research has demonstrated the use of composites to prevent flutter. Therefore, the analysis of a composite wing would be valuable. Lastly, an AM model of a forward swept wing could be built and tested to experimentally study divergence. The experimental study of the effect of surface roughness due to the speckle particles is recommended. That understanding would be helpful to determine better ways to produce the irregular pattern necessary for DIC without compromising the aerodynamic response of the model

.

REFERENCES

Abbott, I. H., & Von Doenhoff, A. E. (2012). *Theory of wing sections: including a summary of airfoil data* (1st ed.). Dover.

Aghanajafi, C., & Daneshmand, S. (2010). Integration of three-dimensional printing technology for wind-tunnel model fabrication. *Journal of Aircraft*, *47*(6), (pp. 2130-2135). https://doi.org/10.2514/1.C031032

Ahn, S. H., Montero, M., Odell, D., Roundy, S., & Wright, P. K. (2002). Anisotropic material properties of fused deposition modeling ABS. *Rapid Prototyping Journal*, *8*(4), (pp. 248-257). https://doi.org/10.1108/13552540210441166

Alacoque, L., Watkins, R. T., & Tamijani, A. Y. (2021). Stress-based and robust topology optimization for thermoelastic multi-material periodic microstructures. *Computer methods in applied mechanics and engineering*, *379*, (pp. 113749). https://doi.org/10.1016/j.cma.2021.113749

Albano, E., & Rodden, W. P. (1969). A doublet-lattice method for calculating lift distributions on oscillating surfaces in subsonic flows. *AIAA Journal*, *7*(2), (pp. 279-285). https://doi.org/10.2514/3.5086

Allaire, G., Geoffroy-Donders, P., & Pantz, O. (2019). Topology optimization of modulated and oriented periodic microstructures by the homogenization method. *Computers & Mathematics with Applications*, *78*(7), (pp. 2197-2229). https://doi.org/10.1016/j.camwa.2018.08.007

Andreassen, E., & Andreasen, C. S. (2014). How to determine composite material properties using numerical homogenization. *Computational Materials Science*, *83*, (pp. 488-495). https://doi.org/10.1016/j.commatsci.2013.09.006

Anuar, H., Ahmad, S., Rasid, R., Ahmad, A., & Busu, W. W. (2008). Mechanical properties and dynamic mechanical analysis of thermoplastic-natural-rubber-reinforced short carbon fiber and kenaf fiber hybrid composites. *Journal of Applied Polymer Science*, *107*(6), (pp. 4043-4052). https://doi.org/10.1002/app.27441

Asadi, D., & Farsadi, T. (2020). Active flutter control of thin walled wing-engine system using piezoelectric actuators. *Aerospace Science and Technology*, (pp. 105853). https://doi.org/10.1016/j.ast.2020.105853

ASTM. (2001). *ASTM-6641 Standard Test Method for Compressive Properties of Polymer Matrix Composite Materials using a Combined Loading Compression (CLC) Test Fixture*. https://doi.org/10.1520/D6641_D6641M-16E01

ASTM. (2010). *ASTM-D695-15 Standard Test for Compressive Properties of Rigid Plastics*. https://doi.org/10.1520/D0695-15

ASTM. (2014). *ASTM-E2015-04 Standard Guide for Preparation of Plastics and Polymeric Specimens for Microstructural Examination*. https://doi.org/10.1520/E2015-04R14

ASTM. (2015). *ASTM-D7028-07 Standard Test Method for Glass Transition Temperature (DMA Tg) of Polymer Matrix Composites by Dynamic Mechanical Analysis (DMA)*. https://doi.org/10.1520/D0638-14

Ayyagari, S., Al-Haik, M., & Rollin, V. (2018). Mechanical and Electrical Characterization of Carbon Fiber/Bucky Paper/Zinc Oxide Hybrid Composites. *C*, *4*(1), (pp. 6). https://doi.org/10.3390/c4010006

Banks, J., Giovannetti, L. M., Soubeyran, X., Wright, A., Turnock, S., & Boyd, S. (2015). Assessment of digital image correlation as a method of obtaining deformations of a structure under fluid load. *Journal of Fluids and Structures*, *58*, (pp. 173-187). https://doi.org/10.1016/j.jfluidstructs.2015.08.007

Barlow, J. B., Rae, W. H., & Pope, A. (1999). *Low-speed wind tunnel testing* (3rd ed.). John wiley & sons.

Blok, L. G., Longana, M. L., Yu, H., & Woods, B. K. (2018). An investigation into 3D printing of fibre reinforced thermoplastic composites. *Additive Manufacturing*, *22*, (pp. 176-186). https://doi.org/10.1016/j.addma.2018.04.039

Boutemedjet, A., Samardžić, M., Rebhi, L., Rajić, Z., & Mouada, T. (2019). UAV aerodynamic design involving genetic algorithm and artificial neural network for wing preliminary computation. *Aerospace Science and Technology*, *84*, (pp. 464-483). https://doi.org/10.1016/j.ast.2018.09.043

Brenken, B., Barocio, E., Favaloro, A., Kunc, V., & Pipes, R. B. (2018). Fused filament fabrication of fiber-reinforced polymers: A review. *Additive Manufacturing*, *21*, (pp. 1-16). https://doi.org/10.1016/j.addma.2018.01.002

Brooks, H., & Molony, S. (2016). Design and evaluation of additively manufactured parts with three dimensional continuous fibre reinforcement. *Materials & Design*, *90*, (pp. 276-283). https://doi.org/10.1016/j.matdes.2015.10.123

Callister Jr, W. D., & Rethwisch, D. G. (2020). *Callister's Materials Science and Engineering* (10th ed.). John Wiley & Sons.

Caminero, M., Chacón, J., García-Moreno, I., & Reverte, J. (2018). Interlaminar bonding performance of 3D printed continuous fibre reinforced thermoplastic composites using fused deposition modelling. *Polymer Testing*, *68*, (pp. 415-423). https://doi.org/10.1016/j.polymertesting.2018.04.038

Capela, C., Oliveira, S., Pestana, J., & Ferreira, J. (2017). Effect of fiber length on the mechanical properties of high dosage carbon reinforced. *Procedia Structural Integrity*, *5*, (pp. 539-546). https://doi.org/10.1016/j.prostr.2017.07.159

Chartoff, R., Menczel, J., & Dillman, S. (2009). Dynamic Mechanical Analysis In J. D. Menczel & R. B. Prime (Eds.), *Thermal Analysis of Polymer Fundamental and Applications* (1 ed.). Hoboken, NJ: John Wiley & Sons, Inc.

Cheng, L., Bai, J., & To, A. C. (2019). Functionally graded lattice structure topology optimization for the design of additive manufactured components with stress constraints. *Computer methods in applied mechanics and engineering*, *344*, (pp. 334-359). https://doi.org/10.1016/j.cma.2018.10.010

Clausen, A., & Andreassen, E. (2017). On filter boundary conditions in topology optimization. *Structural and Multidisciplinary Optimization*, *56*(5), (pp. 1147-1155). https://doi.org/10.1007/s00158-017-1709-1

Crease, A. (2016a). Designing for 3D printing: Making most of additive manufacturing. *Markforged webinar series.* Retrieved from https://markforged.com/resources/blog/design-for-additive-manufacturing-dfam

Crease, A. (2016b). Introducing our new Markforged material: Onyx. Retrieved from https://markforged.com/blog/introducing-our-new-markforged-material-onyx/

Crease, A. (2016c). Reinforcing 3D printed parts with efficient fiber routing: part 1. Retrieved from https://markforged.com/blog/reinforcing-3d-printed-parts-part-1/

da Silva, G. A., Aage, N., Beck, A. T., & Sigmund, O. (2021). Three-dimensional manufacturing tolerant topology optimization with hundreds of millions of local stress constraints. *International Journal for Numerical Methods in Engineering*, *122*(2), (pp. 548-578). https://doi.org/10.1002/nme.6548

Deshpande, V. S., Fleck, N. A., & Ashby, M. F. (2001). Effective properties of the octet-truss lattice material. *Journal of the Mechanics and Physics of Solids*, *49*(8), (pp. 1747-1769). https://doi.org/10.1016/S0022-5096(01)00010-2

Diebold, J. M., Woodard, B., Monastero, M., & Bragg, M. (2015). Experimental study of splitter plates for use with semispan wing models. In *53rd AIAA aerospace sciences meeting*. https://doi.org/10.2514/6.2015-1227.

Donders, P. G. (2018). *Homogenization method for topology optmization of struc-tures built with lattice materials*. Doctoral dissertation, [Université Paris-Saclay].

Duysinx, P., & Bendsøe, M. P. (1998). Topology optimization of continuum structures with local stress constraints. *International Journal for Numerical Methods in Engineering*, *43*(8), (pp. 1453-1478). https://doi.org/10.1002/(SICI)1097-0207(19981230)43:8

Duysinx, P., & Sigmund, O. (1998). New developments in handling stress constraints in optimal material distribution. In *7th AIAA/USAF/NASA/ISSMO symposium on multidisciplinary analysis and optimization*. https://doi.org/10.2514/6.1998-4906.

Feng, W., Ait-Kadi, A., Brisson, J., & Riedl, B. (2003). Polymerization compounding composites of nylon-6, 6/short glass fiber. *Polymer composites*, *24*(4), (pp. 512-524). https://doi.org/10.1002/pc.10049

Fernandes, R., & Tamijani, A. (2016). Flutter Analysis of Laminated Curvilinear-Stiffened Plates. In *57th AIAA/ASCE/AHS/ASC Structures, Structural Dynamics, and Materials Conference*. https://doi.org/10.2514/6.2016-1720.

Fernandes, R. R., & Tamijani, A. Y. (2017). Flutter analysis of laminated curvilinear-stiffened plates. *AIAA Journal*, *55*(3), (pp. 998-1011). https://doi.org/10.2514/1.J055021

Fernandes, R. R., Tamijani, A. Y., & Al-Haik, M. (2021). Mechanical characterization of additively manufactured fiber-reinforced composites. *Aerospace Science and Technology*, *113*, (pp. 106653). https://doi.org/10.1016/j.ast.2021.106653

Fernandes, R. R., van de Werken, N., Koirala, P., Yap, T., Tamijani, A. Y., & Tehrani, M. (2021). Experimental investigation of additively manufactured continuous fiber reinforced composite parts with optimized topology and fiber paths. *Additive Manufacturing*, *44*, (pp. 102056). https://doi.org/10.1016/j.addma.2021.102056

Gbaguidi, A., Anees, M., Namilae, S., & Kim, D. (2017). Dynamic piezoresistive response of hybrid nanocomposites. In *Sensors and Smart Structures Technologies for Civil, Mechanical, and Aerospace Systems 2017*. https://doi.org/10.1117/12.2260208.

Gharibi, K., & Tamijani, A. Y. (2021). Load-Path-Based Topology Optimization of Two-Dimensional Continuum Structures. *AIAA Journal*, (pp. 1-10). https://doi.org/10.2514/1.J059642

Ghebretinsae, F. (2019). *Mechanical Testing And Finite Element Analysis Of 3D Printed Continuous Carbon Fiber Reinforced Onyx® Thermoplastic*. Master's Thesis, [University of Stavanger], Norway. Retrieved from https://uis.brage.unit.no/uis-xmlui/handle/11250/2621028

Gibson, I., Rosen, D. W., & Stucker, B. (2014). *Additive manufacturing technologies* (Vol. 17). Springer.

Goertzen, W. K., & Kessler, M. (2007). Dynamic mechanical analysis of carbon/epoxy composites for structural pipeline repair. *Composites Part B: Engineering*, *38*(1), (pp. 1-9). https://doi.org/10.1016/j.compositesb.2006.06.002

Goh, G., Agarwala, S., Goh, G., Dikshit, V., Sing, S. L., & Yeong, W. Y. (2017). Additive manufacturing in unmanned aerial vehicles (UAVs): Challenges and potential. *Aerospace Science and Technology*, *63*, (pp. 140-151). https://doi.org/10.1016/j.ast.2016.12.019

Groen, J., & Sigmund, O. (2018). Homogenization-based topology optimization for high-resolution manufacturable microstructures. *International Journal for Numerical Methods in Engineering*, *113*(8), (pp. 1148-1163). https://doi.org/10.1002/nme.5575

Groen, J. P., Stutz, F. C., Aage, N., Bærentzen, J. A., & Sigmund, O. (2020). De-homogenization of optimal multi-scale 3D topologies. *Computer methods in applied mechanics and engineering*, *364*, (pp. 112979). https://doi.org/10.1016/j.cma.2020.112979

Groen, J. P., Wu, J., & Sigmund, O. (2019). Homogenization-based stiffness optimization and projection of 2D coated structures with orthotropic infill. *Computer methods in applied mechanics and engineering*, *349*, (pp. 722-742). https://doi.org/10.1016/j.cma.2019.02.031

Guedes, J., & Kikuchi, N. (1990). Preprocessing and postprocessing for materials based on the homogenization method with adaptive finite element methods. *Computer methods in applied mechanics and engineering*, *83*(2), (pp. 143-198). https://doi.org/10.1016/0045-7825(90)90148-F

Hale, A. (2002). *Handbook of Thermal Analysis and Calorimetry, vol. by Cheng SZD* (1st ed., Vol. 3). Elsevier.

Hassani, B., & Hinton, E. (1998). A review of homogenization and topology optimization I—homogenization theory for media with periodic structure. *Computers & Structures*, *69*(6), (pp. 707-717). https://doi.org/10.1016/S0045-7949(98)00131-X

Hatakeyama, T., & Quinn, F. (1999). *Fundamentals and applications to polymer science* (2nd ed.). John Wiley & Sons Ltd.

Hecht, F., & Pironneau, O. (2013). freefem+. Retrieved from https://www.ljll.math.upmc.fr/hecht/ftp/ff++days/2013/2013-FF++-days/2013-ff++-days

Hofstätter, T., Pedersen, D. B., Tosello, G., & Hansen, H. N. (2017). State-of-the-art of fiber-reinforced polymers in additive manufacturing technologies. *Journal of Reinforced Plastics and Composites*, *36*(15), (pp. 1061-1073). https://doi.org/10.1177/0731684417695648

Hollister, S. J., & Kikuchi, N. (1992). A comparison of homogenization and standard mechanics analyses for periodic porous composites. *Computational mechanics*, *10*(2), (pp. 73-95). https://doi.org/10.1007/BF00369853

Holmberg, E., Torstenfelt, B., & Klarbring, A. (2013). Stress constrained topology optimization. *Structural and Multidisciplinary Optimization*, *48*(1), (pp. 33-47). https://doi.org/10.1007/s00158-012-0880-7

Hou, Z., Tian, X., Zheng, Z., Zhang, J., Zhe, L., Li, D., Malakhov, A. V., & Polilov, A. N. (2020). A constitutive model for 3D printed continuous fiber reinforced composite structures with variable fiber content. *Composites Part B: Engineering*, (pp. 107893). https://doi.org/10.1016/j.compositesb.2020.107893

International, A. (2016). *ASTM-D2344/D2344M Standard Test Method for Short-Beam Strength of Polymer Matrix Composite Materials and their Laminates*. https://doi.org/10.1520/D2344_D2344M-16

Isobe, T., Tanaka, T., Nomura, T., & Yuasa, R. (2018). Comparison of strength of 3D printing objects using short fiber and continuous long fiber. In *IOP Conference Series: Materials Science and Engineering*. https://doi.org/10.1088/1757-899X/406/1/012042.

Jiang, D., Hoglund, R., & Smith, D. E. (2019). Continuous fiber angle topology optimization for polymer composite deposition additive manufacturing applications. *Fibers*, *7*(2), (pp. 14). https://doi.org/10.3390/fib7020014

Johnson, S. G. The NLopt nonlinear-optimization package. In. http://github.com/stevengj/nlopt.

Jones, R. M. (1998). *Mechanics of composite materials* (2nd ed.). CRC press.

Junk, S., Schröder, W., & Schrock, S. (2017). Design of additively manufactured wind tunnel models for use with UAVs. *Procedia CIRP*, *60*, (pp. 241-246). https://doi.org/10.1016/j.procir.2017.02.027

Karbhari, V. M., & Wang, Q. (2004). Multi-frequency dynamic mechanical thermal analysis of moisture uptake in E-glass/vinylester composites. *Composites Part B: Engineering*, *35*(4), (pp. 299-304). https://doi.org/10.1016/j.compositesb.2004.01.003

Kroll, E., Artzi, D., & Ralbag, G. (2010). Structural design guidelines for wind tunnel models made by rapid prototyping. In *27th International Congress of the Aeronautal Sciences, Nice, France*. Retrieved from https://www.icas.org/ICAS_ARCHIVE/ICAS2010/PAPERS/084.PDF

Kuester, M., Intaratep, N., & Borgoltz, A. (2018). Laser Displacement Sensors for Wind Tunnel Model Position Measurements. *Sensors*, *18*(12), (pp. 4085). https://doi.org/10.3390/s18124085

Lazarov, B. S., & Sigmund, O. (2011). Filters in topology optimization based on Helmholtz-type differential equations. *International Journal for Numerical Methods in Engineering*, *86*(6), (pp. 765-781). https://doi.org/10.1002/nme.3072

Lazarov, B. S., Wang, F., & Sigmund, O. (2016). Length scale and manufacturability in density-based topology optimization. *Archive of Applied Mechanics*, *86*(1-2), (pp. 189-218). https://doi.org/10.1007/s00419-015-1106-4

Le, C., Norato, J., Bruns, T., Ha, C., & Tortorelli, D. (2010). Stress-based topology optimization for continua. *Structural and Multidisciplinary Optimization*, *41*(4), (pp. 605-620). https://doi.org/10.1007/s00158-009-0440-y

Li, N., Link, G., Wang, T., Ramopoulos, V., Neumaier, D., Hofele, J., Walter, M., & Jelonnek, J. (2020). Path-designed 3D printing for topological optimized continuous carbon fibre reinforced composite structures. *Composites Part B: Engineering*, *182*, (pp. 107612). https://doi.org/10.1016/j.compositesb.2019.107612

Livne, E. (2018). Aircraft active flutter suppression: State of the art and technology maturation needs. *Journal of Aircraft*, *55*(1), (pp. 410-452). https://doi.org/10.2514/1.C034442

Locatelli, D., Mulani, S. B., & Kapania, R. K. (2011). Wing-box weight optimization using curvilinear spars and ribs (SpaRibs). *Journal of Aircraft*, *48*(5), (pp. 1671-1684). https://doi.org/10.2514/1.C031336

Melo, J. D. D., & Radford, D. W. (2005). Time and temperature dependence of the viscoelastic properties of CFRP by dynamic mechanical analysis. *Composite Structures*, *70*(2), (pp. 240-253). https://doi.org/10.1016/j.compstruct.2004.08.025

Menard, K. P. (2008). *Dynamic mechanical analysis: a practical introduction* (2nd ed.). CRC press.

Menard, K. P., & Menard, N. R. (2002). Dynamic mechanical analysis in the analysis of polymers and rubbers. *Encyclopedia of Polymer Science and Technology*, (pp. 1-33). https://doi.org/10.1002/0471440264.pst102.pub2

Meng, S., He, H., Jia, Y., Yu, P., Huang, B., & Chen, J. (2017). Effect of nanoparticles on the mechanical properties of acrylonitrile–butadiene–styrene specimens fabricated by fused deposition modeling. *Journal of Applied Polymer Science*, *134*(7), (pp. 1-9). https://doi.org/10.1002/app.44470

Miyano, Y., & Nakada, M. (2006). Time and temperature dependent fatigue strengths for three directions of unidirectional CFRP. *Experimental mechanics*, *46*(2), (pp. 155-162). https://doi.org/10.1007/s11340-006-6834-5

Morovat, F., Mozaffari, A., Roshanian, J., & Zare, H. (2019). A novel aspect of composite sandwich fairing structure optimization of a two-stage launch vehicle (Safir) using multidisciplinary design optimization independent subspace approach. *Aerospace Science and Technology*, *84*, (pp. 865-879). https://doi.org/10.1016/j.ast.2018.10.033

MSC. (1987). Aeroelastic Analysis User's Guide. Retrieved from https://simcompanion.mscsoftware.com/infocenter/index?page=content&id=DOC9182

Ning, F., Cong, W., Hu, Z., & Huang, K. (2017). Additive manufacturing of thermoplastic matrix composites using fused deposition modeling: A comparison of two reinforcements. *Journal of Composite Materials*, *51*(27), (pp. 3733-3742). https://doi.org/10.1177/0021998317692659

Pankonien, A. M., Reich, G. W., Lindsley, N., & Smyers, B. (2017). 3d-printed wind tunnel flutter model. In *58th AIAA/ASCE/AHS/ASC Structures, Structural Dynamics, and Materials Conference*. https://doi.org/10.2514/6.2017-0411.

Pantz, O., & Trabelsi, K. (2008). A post-treatment of the homogenization method for shape optimization. *SIAM Journal on Control and Optimization*, *47*(3), (pp. 1380-1398). https://doi.org/10.1137/070688900

Papapetrou, V., Patel, C., & Tamijani, A. (2020). Stiffness-based optmization framework for the topology and fiber paths of continuous fiber composites. *Composites Part B: Engineering*, (pp. 1-15). https://doi.org/10.1016/j.compositesb.2019.107681

Parandoush, P., & Lin, D. (2017). A review on additive manufacturing of polymer-fiber composites. *Composite Structures*, *182*, (pp. 36-53). https://doi.org/10.1016/j.compstruct.2017.08.088

Pipes, R. B. (1971). Moire analysis of the interlaminar shear edge effect in laminated composites. *Journal of Composite Materials*, *5*(2), (pp. 255-259). https://doi.org/10.1177/002199837100500211

Pipes, R. B., & Pagano, N. J. (1970). Interlaminar Stresses in Composite Laminates Under Uniform Axial Extension. *Journal of Composite Materials*, *4*(4), (pp. 538-548). https://doi.org/10.1177/002199837000400409

Rajpal, D., Gillebaart, E., & De Breuker, R. (2019). Preliminary aeroelastic design of composite wings subjected to critical gust loads. *Aerospace Science and Technology*, *85*, (pp. 96-112). https://doi.org/10.1016/j.ast.2018.11.051

Raza, A., Farhan, S., Nasir, S., & Salamat, S. (2021). Applicability of 3D Printed Fighter Aircraft Model for Subsonic Wind Tunnel. In *2021 International Bhurban Conference on Applied Sciences and Technologies (IBCAST)*, Islamabad, Pakistan. https://doi.org/10.1109/IBCAST51254.2021.9393214.

Rêgo, I. d., Marcos, T. V., Galvão, V. A., Vilela, R. G., Minucci, M. A., Martos, J. F., & Oliveira, A. C. (2018). Preliminary Studies on Hypersonic Flows Over 3D Printed Models. In *22nd AIAA International Space Planes and Hypersonics Systems and Technologies Conference*. https://doi.org/10.2514/6.2018-5321.

Rozvany, G., & Sobieszczanski-Sobieski, J. (1992). New optimality criteria methods: forcing uniqueness of the adjoint strains by corner-rounding at constraint intersections. *Structural optimization*, *4*(3-4), (pp. 244-246). https://doi.org/10.1007/BF01742752

Rudin, A., & Choi, P. (1999). *Polymer science and engineering*. Academic Press.

Rumpf, R. C., & Pazos, J. (2012). Synthesis of spatially variant lattices. *Optics express*, *20*(14), (pp. 15263-15274). https://doi.org/10.1364/OE.20.015263

Safonov, A. A. (2019). 3D topology optimization of continuous fiber-reinforced structures via natural evolution method. *Composite Structures*, *215*, (pp. 289-297). https://doi.org/10.1016/j.compstruct.2019.02.063

Saito, Y., Fernandez, F., Tortorelli, D. A., Compel, W., Lewicki, J., & Lambros, J. (2019). Experimental validation of an additively manufactured stiffness-optimized short-fiber reinforced composite clevis joint. *Experimental mechanics*, *59*(6), (pp. 859-869). https://doi.org/10.1007/s11340-019-00514-2

Sanei, S. H. R., Lash, Z., Servey, J., Gardone, F., & Nikhare, C. P. (2019). Mechanical properties of 3D printed fiber reinforced thermoplastic. In *ASME International Mechanical Engineering Congress and Exposition*. https://doi.org/10.1115/IMECE2019-10303.

Scrocco, M., Chamberlain, T., Chow, C., Weinreber, L., Ellks, E., Halford, C., Cortes, P., Conner, B. P., & Incubator, Y. B. (2018). Impact Testing of 3D Printed Kevlar-Reinforced Onyx Material. *Proceedings of the 29th Annual International Solid Freeform Fabrication*, (pp. Retrieved from http://utw10945.utweb.utexas.edu/sites/default/files/2018/091%20ImpactTestingof3DPrintedKevlarReinforcedOny.pdf

Stutz, F., Groen, J., Sigmund, O., & Bærentzen, J. (2020). Singularity aware de-homogenization for high-resolution topology optimized structures. *Structural and Multidisciplinary Optimization*, *62*(5), (pp. 2279-2295). https://doi.org/10.1007/s00158-020-02681-6

Sugiyama, K., Matsuzaki, R., Malakhov, A. V., Polilov, A. N., Ueda, M., Todoroki, A., & Hirano, Y. (2020). 3D printing of optimized composites with variable fiber volume fraction and stiffness using continuous fiber. *Composites Science and Technology*, *186*, (pp. 107905). https://doi.org/10.1016/j.compscitech.2019.107905

Svanberg, K. (1987). The method of moving asymptotes—a new method for structural optimization. *International Journal for Numerical Methods in Engineering*, *24*(2), (pp. 359-373). https://doi.org/10.1002/nme.1620240207

Sved, G., & Ginos, Z. (1968). Structural optimization under multiple loading. *International Journal of Mechanical Sciences*, *10*(10), (pp. 803-805). https://doi.org/10.1016/0020-7403(68)90021-0

Tamijani, A., Gharibi, K., Kobayashi, M., & Kolonay, R. (2018). Load paths visualization in plane elasticity using load function method. *International Journal*

of Solids and Structures, *135*, (pp. 99-109). https://doi.org/10.1016/j.ijsolstr.2017.11.013

Tamijani, A., Velasco, S., & Alacoque, L. (2020). Topological and morphological Design of Additively-Manufacturable Spatially-Varying Periodic Cellular Solids. *Materials & Design*, (pp. 109155). https://doi.org/10.1016/j.matdes.2020.109155

Tewari, A. (2015). *Aeroservoelasticity* (1st ed.). Springer.

Thompson, B., & Whitelaw, J. (1988). Flow-around airfoils with blunt, round, and sharp trailing edges. *Journal of Aircraft*, *25*(4), (pp. 334-342). https://doi.org/10.2514/3.45568

Tian, X., Liu, T., Yang, C., Wang, Q., & Li, D. (2016). Interface and performance of 3D printed continuous carbon fiber reinforced PLA composites. *Composites Part A: Applied Science and Manufacturing*, *88*, (pp. 198-205). https://doi.org/10.1016/j.compositesa.2016.05.032

van de Werken, N., Hurley, J., Khanbolouki, P., Sarvestani, A. N., Tamijani, A. Y., & Tehrani, M. (2019). Design considerations and modeling of fiber reinforced 3D printed parts. *Composites Part B: Engineering*, *160*, (pp. 684-692). https://doi.org/10.1016/j.compositesb.2018.12.094

van de Werken, N., Koirala, P., Ghorbani, J., Doyle, D., & Tehrani, M. (2021). Investigating the hot isostatic pressing of an additively manufactured continuous carbon fiber reinforced PEEK composite. *Additive Manufacturing*, *37*, (pp. 101634). https://doi.org/10.1016/j.addma.2020.101634

van de Werken, N., Tekinalp, H., Khanbolouki, P., Ozcan, S., Williams, A., & Tehrani, M. (2019). Additively Manufactured Carbon Fiber-Reinforced Composites: State of the Art and Perspective. *Additive Manufacturing*, *31*, (pp. 100962). https://doi.org/10.1016/j.addma.2019.100962

Van Der Klift, F., Koga, Y., Todoroki, A., Ueda, M., Hirano, Y., & Matsuzaki, R. (2016). 3D printing of continuous carbon fibre reinforced thermo-plastic (CFRTP) tensile test specimens. *Open J. Compos. Mater*, *6*(1), (pp. 18-27). https://doi.org/10.4236/ojcm.2016.61003

Wang, F., Lazarov, B. S., & Sigmund, O. (2011). On projection methods, convergence and robust formulations in topology optimization. *Structural and Multidisciplinary Optimization*, *43*(6), (pp. 767-784). https://doi.org/10.1007/s00158-010-0602-y

Wang, M. Y., Wang, X., & Guo, D. (2003). A level set method for structural topology optimization. *Computer methods in applied mechanics and engineering*, *192*(1-2), (pp. 227-246). https://doi.org/10.1016/S0045-7825(02)00559-5

Weng, Z., Wang, J., Senthil, T., & Wu, L. (2016). Mechanical and thermal properties of ABS/montmorillonite nanocomposites for fused deposition modeling 3D printing. *Materials & Design*, *102*, (pp. 276-283). https://doi.org/10.1016/j.matdes.2016.04.045

Wu, W., Geng, P., Li, G., Zhao, D., Zhang, H., & Zhao, J. (2015). Influence of layer thickness and raster angle on the mechanical properties of 3D-printed PEEK and a comparative mechanical study between PEEK and ABS. *Materials*, *8*(9), (pp. 5834-5846). https://doi.org/10.3390/ma8095271

Yang, R., & Chen, C. (1996). Stress-based topology optimization. *Structural optimization*, *12*(2), (pp. 98-105). https://doi.org/10.1007/BF01196941

Yu, H., Huang, J., Zou, B., Shao, W., & Liu, J. (2020). Stress-constrained shell-lattice infill structural optimisation for additive manufacturing. *Virtual and Physical Prototyping*, *15*(1), (pp. 35-48). https://doi.org/10.1080/17452759.2019.1647488

Zhang, S., Jaworski, A. J., McParlin, S., & Turner, J. T. (2019). Experimental investigation of the flow structures over a 40 swept wing. *The Aeronautical Journal*, *123*(1259), (pp. 39-55). https://doi.org/10.1017/aer.2018.118

Zhang, W., Cotton, C., Sun, J., Heider, D., Gu, B., Sun, B., & Chou, T.-W. (2018). Interfacial bonding strength of short carbon fiber/acrylonitrile-butadiene-styrene composites fabricated by fused deposition modeling. *Composites Part B: Engineering*, *137*, (pp. 51-59). https://doi.org/10.1016/j.compositesb.2017.11.018

Zhong, W., Li, F., Zhang, Z., Song, L., & Li, Z. (2001). Short fiber reinforced composites for fused deposition modeling. *Materials Science and Engineering: A*, *301*(2), (pp. 125-130). https://doi.org/10.1016/S0921-5093(00)01810-4

Zhu, W. (2019). Models for wind tunnel tests based on additive manufacturing technology. *Progress in Aerospace Sciences*, *110*, (pp. 100541). https://doi.org/10.1016/j.paerosci.2019.05.001

Zhu, W., Miao, K., & Li, D. (2019). Static aeroelastic models with integrated stiffness-contributing shell structures built by additive manufacturing. *Engineering Structures*, *187*, (pp. 352-361). https://doi.org/10.1016/j.engstruct.2019.02.066

Zhu, W., Zhang, X., & Li, D. (2019). Flexible all-plastic aircraft models built by additive manufacturing for transonic wind tunnel tests. *Aerospace Science and Technology*, *84*, (pp. 237-244). https://doi.org/10.1016/j.ast.2018.10.024

PUBLICATIONS

Fernandes, R., & Tamijani, A. (2016). Flutter Analysis of Laminated Curvilinear-Stiffened Plates. 57th AIAA/ASCE/AHS/ASC Structures, Structural Dynamics, and Materials Conference. https://doi.org/10.2514/6.2016-1720

Fernandes, R. R., & Tamijani, A. Y. (2017). Flutter analysis of laminated curvilinear-stiffened plates. *AIAA Journal*, *55*(3), (pp. 998-1011). https://doi.org/10.2514/1.J055021

Fernandes, R. R., Tamijani, A. Y., & Al-Haik, M. (2021). Mechanical characterization of additively manufactured fiber-reinforced composites. *Aerospace Science and Technology*, *113*, 106653. https://doi.org/https://doi.org/10.1016/j.ast.2021.106653

Fernandes, R. R., van de Werken, N., Koirala, P., Yap, T., Tamijani, A. Y., & Tehrani, M. (2021). Experimental investigation of additively manufactured continuous fiber reinforced composite parts with optimized topology and fiber paths. *Additive Manufacturing*, *44*, 102056. https://doi.org/https://doi.org/10.1016/j.addma.2021.102056